

AD-A136 086

ACOUSTO-OPTIC PROCESSING OF 2-D SIGNALS USING TEMPORAL  
AND SPATIAL INTEGRATION (U) CALIFORNIA INST OF TECH  
PASADENA D PSALTIS 31 MAY 83 AFOSR-TR-83-1100

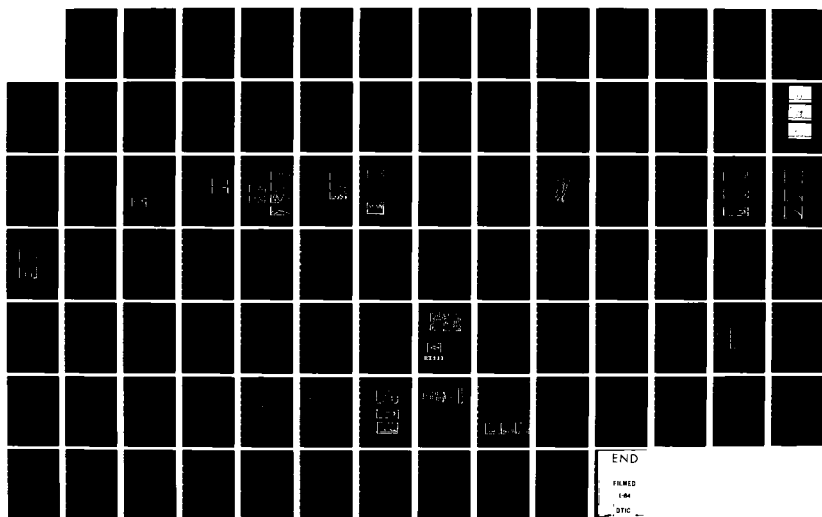
1/1

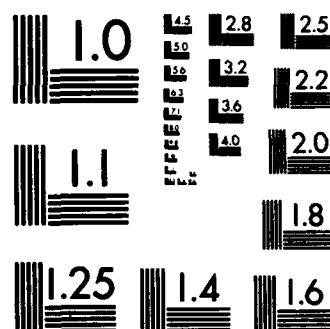
UNCLASSIFIED

AFOSR-82-0128

F/G 20/6

NL





AFOSR-TR- 83 - 1100

2

ANNUAL REPORT

Submitted to:

AIR FORCE OFFICE OF SCIENTIFIC  
RESEARCH

Grant Number: AFOSR-82-0128

ACOUSTO-OPTIC PROCESSING OF 2-D SIGNALS  
USING TEMPORAL AND SPATIAL INTEGRATION

Reporting Period: April 1, 1982 - May 31, 1983

Principal Investigator:

Professor Demetri Psaltis  
California Institute of Technology  
Pasadena, CA 91125

DTIC  
DEC 20 1983

Approved for public release;  
distribution unlimited.

83 12 20 038

AD-A236086

DTIC FILE COPY

**UNCLASSIFIED**

unclassified

SECURITY CLASSIFICATION OF THIS PAGE (When Data Entered)

REPORT DOCUMENTATION PAGE		READ INSTRUCTIONS BEFORE COMPLETING FORM
1. REPORT NUMBER <b>AFOSR-TR- 83 - 1100</b>	2. GOVT ACCESSION NO.	3. RECIPIENT'S CATALOG NUMBER
4. TITLE (and Subtitle) <b>ACOUSTO-OPTIC PROCESSING OF 2-D SIGNALS USING TEMPORAL AND SPATIAL INTEGRATION</b>		5. TYPE OF REPORT & PERIOD COVERED <b>ANNUAL 01 DEC 82- 31 MAY 83</b>
		6. PERFORMING ORG. REPORT NUMBER
7. AUTHOR(s) <b>D. Psaltis</b>		8. CONTRACT OR GRANT NUMBER(s) <b>AFOSR-82-0128</b>
9. PERFORMING ORGANIZATION NAME AND ADDRESS <b>California Institute of Technology Pasadena, CA 91125</b>		10. PROGRAM ELEMENT, PROJECT, TASK AREA & WORK UNIT NUMBERS <b>61102F 2305/B1</b>
11. CONTROLLING OFFICE NAME AND ADDRESS <b>Air Force Office of Scientific Research/NE Building 410 Bolling AFB, DC 20332</b>		12. REPORT DATE <b>31 May 1983</b>
14. MONITORING AGENCY NAME & ADDRESS (if different from Controlling Office)		13. NUMBER OF PAGES <b>91</b>
		15. SECURITY CLASS. (of this report) <b>Unclassified</b>
		15a. DECLASSIFICATION/DOWNGRADING SCHEDULE
16. DISTRIBUTION STATEMENT (of this Report) <div style="text-align: center;"><p>Approved for public release; distribution unlimited.</p><p>Approved for public release; distribution unlimited.</p></div>		
17. DISTRIBUTION STATEMENT (of the abstract entered in Block 20, if different from Report)		
18. SUPPLEMENTARY NOTES		
19. KEY WORDS (Continue on reverse side if necessary and identify by block number) <b>Acousto-Optic Processing, 2-D Correlator, SAR, Laser Diodes, two- dimensional signal processing synthetic aperture radar, acousto- optic devices, imaging, image processing</b>		
20. ABSTRACT (Continue on reverse side if necessary and identify by block number) <b>The research reported is the result of the collaboration of several members of the research group at Caltech. Eung E. Paek is responsible for the experimental 2-D correlator. Kelvin Wagner has contributed in the study and characterization of CCDs, in the SAR experiments and general architectural studies. Michael Haney has done the laser diode characterization and contributed in the SAR work. Santosh Venkatesh worked on the statistical characterization of time-and- space integrating architecture.</b>		

### ACKNOWLEDGMENTS

The research reported here is the result of the collaboration of several members of the principal investigator's research group at Caltech. Eung E. Paek is responsible for the experimental 2-D correlator. Kelvin Wagner has contributed in the study and characterization of CCDs, in the SAR experiments and general architectural studies. Michael Haney has done the laser diode characterization and contributed in the SAR work. Santosh Venkatesh worked on the statistical characterization of time-and-space integrating architectures.

We wish to thank Tom Bicknell from JPL for numerous discussions on SAR, Peter Kellman from ESL for acousto-optic device designs and members of Professor Yariv's group here at Caltech for their advice in the area of laser diodes. Finally we thank the AFOSR and Dr. John Neff for making this research possible.



AIR FORCE OFFICE OF SCIENTIFIC RESEARCH (AFOSR)  
NOTICE OF TRANSMITTAL TO DTIC

This technical report has been reviewed and is  
approved for public release IAW AFR 190-12.  
Distribution is unlimited.

MATTHEW J. KERPER  
Chief, Technical Information Division

*Documents include info on*

Table of Contents

	Page
I. Introduction - - - - -	1
II. Architectures - - - - -	4
III. Devices - - - - -	10
Appendix IIIa Coherence Properties of Pulsed Laser Diodes - -	24
Appendix IIIb Acousto-optic device data - - - - -	31
IV. Dynamic Range Issues - - - - -	40
V. Applications - - - - -	47
Appendix Va. Image correlation; theory - - - - -	49
Appendix Vb. Image correlation, experiments - - - - -	54
<i>Synthetic aperture radar;</i>	
Appendix Vc. SAR; theory - - - - -	59
Appendix Vd. SAR; experiments - - - - -	66
Appendix Ve 2-D Fourier transform; <i>and</i> - - - - -	75
Appendix Vf Moments - - - - -	81
VI. References - - - - -	88

## I. INTRODUCTION

The primary advantage of optical processing systems is their parallel processing capability. Typically  $10^3 \times 10^3$  analog data points can be processed simultaneously. Furthermore the optical system has maximum interconnection capability, allowing each data point from the input plane to be multiplied with all the  $10^3 \times 10^3$  data points stored in the frequency plane of a conventional Vander Lugt correlator [1]. This leads to the computation of  $10^{12}$  analog multiplications in the time it takes for light to propagate from the input to the output plane. The extremely high processing power of the optical system can only be realized in practice if suitable input/output devices exist. Two dimensional spatial light modulators [2,3] remain the major factor limiting the speed and the accuracy of the optical processors they are part of. Acousto-optic devices (AODs) have emerged in recent years as high quality, wideband ( $10^9$  Hz) light modulators and consequently they have been extensively used as the input transducer in 1-D optical signal processors [4]. A relative disadvantage of AOD's is that they are 1-D light modulators with a linear space bandwidth product of approximately  $10^3$ . The typical images that we like to be able to process optically have at least  $10^2 \times 10^2$  pixels (more typically  $10^3 \times 10^3$ ) and AODs cannot represent an entire image simultaneously. To overcome this difficulty, only a portion (a line) of an image is entered into the optical processor at one time and is processed separately. The intermediate results are temporarily stored on a 2-D optical detector (in the form of photogenerated charge) and allowed to accumulate on the detector until all the lines of the input image have been entered and processed. We will show in the next chapter that 2-D linear operations can be performed in this manner, if the kernel is shift invariant or separable in the two coordinates. This processing method

is called time and space integrating [5,6,7], since each line of data is processed by space integration and the final result is produced by integrating in time on the detector. The spatial integrating part of the processor operates at the very high bandwidth of the acousto-optic device (up to  $10^9$  Hz) while the time integrating processor serves as a convenient intermediate storage and data manager. Data is produced by the space integrating processor at extremely high rates (typically higher than  $10^{10}$  analog samples/second). The time integration compresses this rate to a manageable  $10^7$  samples/second and in the process a useful signal processing operation is performed.

There are two main factors that we feel make time-and space integrating attractive. Firstly, since the processing is performed in the time domain there is increased flexibility (perhaps we can call it programmability) in controlling the flow of data through the processor and the operations that are being performed. The second, and perhaps most important factor, is the implementation of these architectures with well developed devices (AODs, laser diodes, CCD arrays) which can lead to the development of practical (compact, inexpensive and power/efficient) powerful 2-D optical processors. The state of the art and the experimental characterization of the devices we use, are presented in Chapter III.

The price that we must pay for the convenience of using the optical detector as an accumulator is the bias built-up problem that is always associated with temporal integration. The problem arises because we wish to represent bipolar signals by photogenerated charges. Since the photogenerated charge is proportional to light intensity, (a positive quantity) a bias is introduced so that a positive signal on the detector smaller than the bias level can be interpreted as a negative signal. The bias always diminishes the dynamic range with which the output can be represented. It is therefore crucial to select the optimum



mode of operation and minimize the bias built up. This issue and the closely related subject of coherent vs. incoherent implementation are addressed in chapter IV.

We mentioned earlier that any 2-D linear operation with a separable or shift invariant kernel can be implemented with time and space integrating architectures. In principle then, these processors can be applied to any problem that requires the computation of such operations. Each problem however has its own peculiarities and a lot is gained by designing architectures specifically for a given application. During this reporting period we have considered 2-D correlation [8,9] the calculation of moments [10], synthetic aperture radar [11,12] and 2-D spectrum analysis [13]. Architectures for each of these problems and initial experiments are presented in chapter V.

## II. ARCHITECTURES

The TSI architectures we are investigating can be described in general by the block diagram of Figure 1.

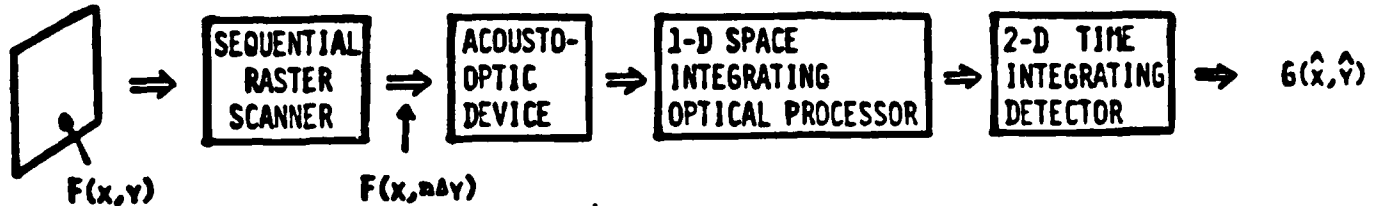


Figure 1. Time and space integrating processing of 2-D signals.

$f(x,y)$  is the 2-D data (usually an image) on which we will perform an arbitrary linear operation:

$$g(\hat{x}, \hat{y}) = \iint f(x, y) h(x, \hat{x}, y, \hat{y}) dx dy. \quad (1)$$

$h$  is the impulse response of the linear operator and  $g$  is the output we wish to produce. The function  $f(x,y)$  is sampled in the  $y$  direction and it is scanned along the  $x$  direction to produce a temporal electronic signal. If  $f(x,y)$  is an image, a TV camera performs this function by producing the video signal. The video signal is applied to an AOD where it generates a travelling acoustic wave proportional to the video within the acoustic delay of the AOD. The delay is made to be exactly equal to the duration of one video line. At periodic time instances the acoustic signal in the AOD corresponds to precisely one raster line of  $f(x,y)$ . At these instances the AOD is illuminated with a short light pulse. The light diffracted by the AOD each time the light source is pulsed, is spatially modulated by one of the lines of  $f(x,y)$ . At periodic time instances

the light is spatially modulated by consecutive lines of  $f(x,y)$ . This modulation scheme can be thought of as spatial modulation of the light with the  $x$  variation of the image  $f(x,y)$  and temporal light modulation by the  $y$  variation. Each line of  $f(x,y)$  denoted by  $f(x,n\Delta y)$  is processed by a 1-D multichannel space integrating optical processor whose operation is described by the following equation

$$g_n(\hat{x},\hat{y}) = \int f(x,n\Delta y) h(x,\hat{x},n\Delta y,\hat{y}) dx. \quad (2)$$

The output of this optical processor is detected by a 2-D integrating CCD array on which the results from consecutive lines are accumulated. After  $N$  video lines have been processed and detected, the signal that is accumulated is given by

$$g(\hat{x},\hat{y}) = \sum_n \int f(x,n\Delta y) h(x,\hat{x},n\Delta y,\hat{y}) dx. \quad (3)$$

This equation is a modified version of Eq. (1), with the integration over the continuous variable  $y$ , replaced by the summation over the discrete variable  $n\Delta y$ .

The development of Eq. (3) suggests the method through which it is in principle possible to implement 2-D signal processing operations with AOD's. It does not tell us what linear operations are feasible and the optical systems that will implement these operations. We spent considerable effort to determine whether it is possible to implement the most general 2-D shift variant kernel,  $h(x,\hat{x},y,\hat{y})$ . Our conclusion is that there is no efficient method for doing so and the reason is simply lack of enough independent dimensions. The implementation of a general kernel  $h(x,\hat{x},y,\hat{y})$  requires 4 independent variables and we have only 3 (2 spatial and time) to work with. Therefore, our conclusion is that unless we are willing to use wavelength

as a fourth variable, or temporal/spatial multiplexing (solutions we consider impractical at this point), it is not possible to implement the most general 2-D linear operation. The two most important 2-D linear operations can be implemented however: separable and shift-invariant operations.

If the kernel is separable ( $h(x, \hat{x}, y, \hat{y}) = h_1(x, \hat{x}) h_2(y, \hat{y})$ ), Eq. (3) takes the following form.

$$g(x, y) = \sum_n \left[ \int f(x, n\Delta y) h_1(x, \hat{x}) dx \right] h_2(n\Delta y, \hat{y}). \quad (4)$$

This type of operation can be implemented with a cascade of 1-D time and space integrating processors operating in orthogonal spatial dimensions. The orthogonality of the spatial domains of the two processors implies that they operate independently (they do not have to be coupled, simply interfaced) and therefore their implementation is relative straightforward. Arbitrary space-variant separable kernels can be implemented with the TSI method. One possible implementation of a general space-variant separable kernel processor is shown in Figure 2. The input image  $f(x, y)$  is applied to AOD1 as a TV video signal. Each line of the input image is processed in the x dimension by an astigmatic 1-D space variant processor (vector-matrix multiplier [14]). This portion of the processor implements the integration over x in equation (4) and produces the result in the form of a beam modulated spatially in the vertical direction. A second AOD is placed in the horizontal direction. This AOD modulates the light from the astigmatic processor by the nth line of the function  $h_2(x, y)$  ( $h_2(n\Delta y, \hat{y})$ ) at the instant the nth line of the input function  $f(x, y)$  is in the first AOD. The light diffracted by the second AOD is imaged onto a 2-D CCD which accumulates the light from all the lines of the input pattern (perform the summation over n in Eq. (4)). The significance of the architecture in Figure 2 is primarily at theoretical because it demonstrates that any linear operation with separable

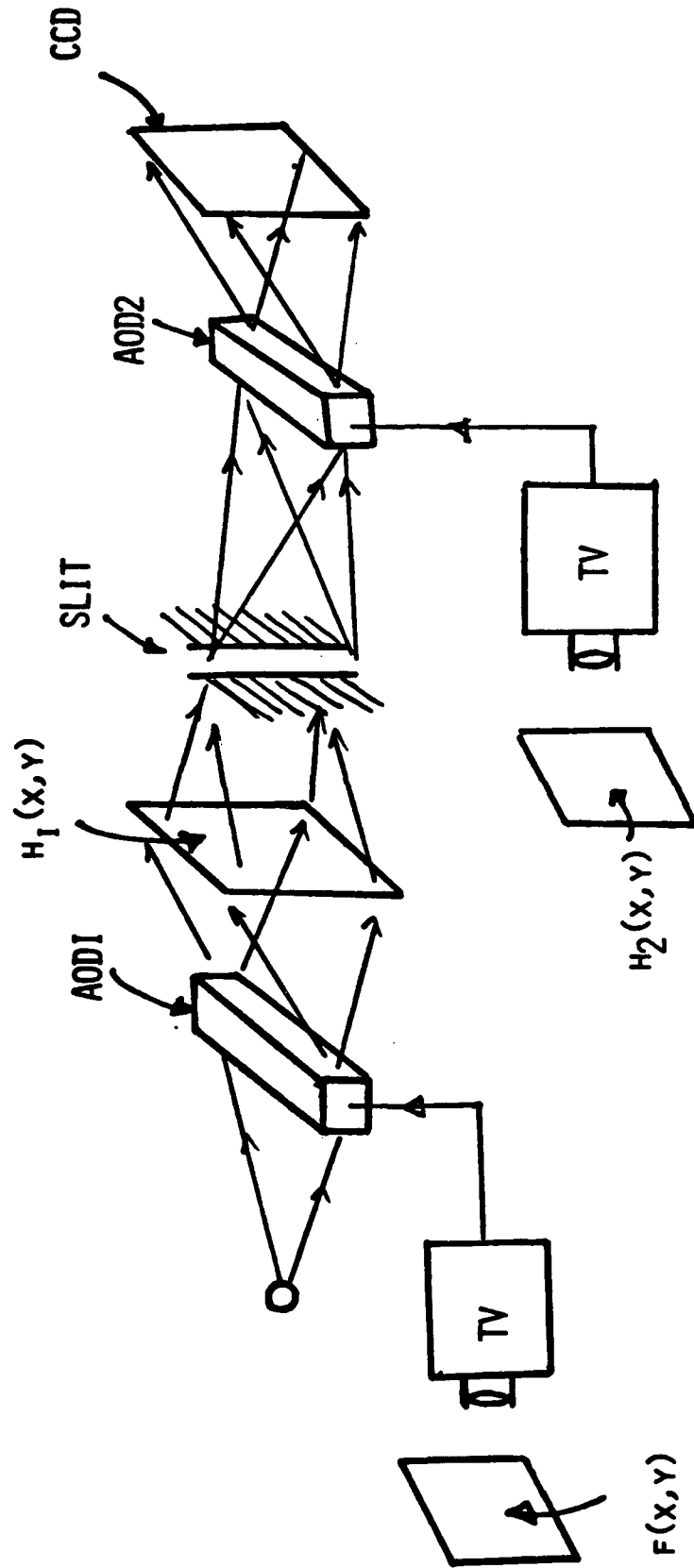


FIGURE 2. TIME-AND-SPACE INTEGRATING ARCHITECTURE FOR THE IMPLEMENTATION OF 2-D LINEAR OPERATIONS, WITH SHIFT VARIANT, SEPARABLE KERNEL

kernel can be implemented with the time-space integrating method. In practice, if a specific separable kernel is given a simpler and more elegant architecture can generally be found. Specific architectures for the computation of the 2-D Fourier transform, the moments of an image and synthetic aperture image formation have been designed and they are discussed in the applications section of this report.

The second class of 2-D linear operations that are implementable with the time-and-space integrating method are those with shift invariant kernels. In this case,

$$\begin{aligned} g(\hat{x}, \hat{y}) &= \sum_n \int f(x, n\Delta y) h(x + \hat{x}, n\Delta y + \hat{y}) dx \\ &= \sum_n \left\{ \left[ \int f(x, n\Delta y) h(x + \hat{x}, y) dx \right] * \delta(y + n\Delta y) \right\} \end{aligned} \quad (5)$$

Where \* denotes convolution and  $\delta$  is the Dirac delta function. The integral inside the brackets is the 1-D correlation of the nth line of  $f(x, y)$  with all the lines of the impulse response function  $h(x, y)$ .

These 1-D correlations must be shifted along the direction orthogonal to the direction in which the correlation is performed by a distance equal to  $n\Delta y$ . The 2-D correlation can then be obtained by summation over all the partial correlations. In a TSI architecture this last summation is performed by the time integrating detector array. The multichannel 1-D correlation can be performed by multiplying the 1-D Fourier transform of each line of the input function with the transforms of all the lines of the filter function  $h$ . Finally to complete the architecture a shifting mechanism must be incorporated that will transfer the data in the  $y$  direction on the detector before the summation over  $n$  is performed. A very convenient way to accomplish this is through the use of a CCD camera with which the transfer can be performed electronically [15]. Our work thus far on TSI architectures for shift invariant

operations has been concentrated on the frequency plane/CCD implementation. Detailed descriptions and experimental results are presented in chapter V of this report. Eq. (5) however suggests a general methodology through which alternate architectures can be designed. For instance, the 1-D multichannel correlation can be implemented by multiplication in the image plane and use of the travelling wave nature of the input AOD. Similarly, the shifting in the  $\hat{y}$  dimension can be performed by an auxiliary optical scanner instead of the electronic scanning that is performed by the CCD.

### III. DEVICES

We mentioned earlier that one of the advantages of the TSI architectures is their implementation with well developed devices. The key components common to almost all architectures are the pulsed light source, acousto-optic devices, and CCD detector arrays. A thorough assessment of the state-of-the-art and experimental characterization of selected devices was carried out during this reporting period. The devices we used in our experiments are operated in unconventional modes and therefore they had to be specifically designed for our application or characterized in the mode in which we operate them. The limitations that the devices impose on the performance of the systems were identified and optimum operating modes were selected.

1. Pulsed light source. A pulsed light source is required in the majority of the TSI architectures. The pulse width requirement is that it is shorter than the bandwidth of the input signal applied to the AOD. Since AODs have bandwidths from 20 to  $10^3$  MHz, pulse durations in the range 1-50 nseconds are required. The pulse repetition frequency must be locked to the rate at which new lines of data are entered into the system. This rate cannot exceed the inverse of the temporal window of the AOD ( 1-100  $\mu$ sec) and typically the PRF is  $10^4$ - $10^5$  Hz. The peak power must be sufficiently high to give an average power of  $10^{-5}$ - $10^{-3}$  W. In the majority of the applications the duty cycle of the pulsed laser is  $10^{-3}$  and therefore peak powers of 10- $10^3$  mW are required. Finally, coherence lengths of .5 to 2 cm are needed in some of the architectures. Gas lasers operated in the cavity dumped mode can easily satisfy all the stated requirements. Gas lasers however are very inefficient (.1% typically), large and expensive (particularly with a cavity dumper). Laser diodes on the other hand, have diametrically opposite characteristics: 10% power efficiency,



small size and cost. Pulses in the nanosecond range with peak powers of  $10\text{-}10^3$  mW can be readily produced by commercially available laser diodes. In addition laser diodes can be directly modulated which provides an added convenience in the design of the optical architecture. Laser diodes however, have some disadvantages. The lasing wavelength of the most common GaAs/AlGaAs lasers is around 800 nm. Both CCD detectors and acousto-optic devices work better at shorter wavelengths. The coherence and temperature stability of these lasers when operated in the pulsed mode were not known previously. The coherence and stability of several commercially available lasers was measured. The results were published in a paper attached as an appendix to this chapter. Our conclusions have been very positive. Laser diodes that are designed to lase in a single mode under cw operation, become coherent (single mode) within 1-2 nanoseconds after the onset of the pulse. This sets the lower limit on the available pulse width to approximately 10 nseconds. The maximum length of the light pulses is limited to 100 nanoseconds for coherence lengths in the order of 1cm, because the temperature of the laser junction increases exponentially after the onset of each pulse causing a corresponding shift in the lasing wavelength. The available range in pulse width (10-100 nanoseconds) for coherent operation is actually very convenient for our experiments because it allows processing of signals with bandwidths up to 50 MHz. At the beginning of this reporting period we felt that pulsed laser diodes would be inadequate as the source for most of the TSI architectures. Happily, our experience with laser diodes has shown the opposite to be true. We believe that the suitability of laser diodes is a crucial factor that can make TSI architectures practical in the immediate future, because of the low power requirements, size and cost of these devices.

2. Acousto-optic device. The AOD serves as the real time input transducer that brings the data to be processed into the TSI architectures. The primary motivation for investigating these architectures is the excellent light modulation properties of AOD's (bandwidth, linearity, optical quality, efficiency). A device was designed and manufactured specifically for the TSI architectures. The custom design was dictated by several considerations. The bandwidth of the signals we are processing in most of the applications is limited to 5-20 MHz. For instance the standard video signal from a TV camera has a bandwidth in this range. Consequently, in order to obtain a linear space bandwidth product in the order of  $10^3$ , a long acoustic delay is required. For instance, a standard video line is 63  $\mu$ seconds long. The maximum useable delay that an AOD can have is determined by the length of quality crystal that can be grown, the acoustic velocity and the acoustic attenuation. The best available material is  $\text{TeO}_2$  because of its slow (shear wave) acoustic velocity and availability of long crystals. The acoustic attenuation is relatively high in  $\text{TeO}_2$ , but it permits up to 100  $\mu$ sec devices for relatively low bandwidths. The device we are working with has 70  $\mu$ sec delay and 30 MHz 1dB bandwidth, at  $\lambda = 820$  nm. A second consideration that was crucial in designing this device was the quality of the Schlieren image, particularly since in all the TSI architectures the light diffracted by the AOD is expanded in the direction orthogonal to the acoustic wave. The Schlieren image can be severely distorted due to acoustic diffraction which places nulls in the diffracted image. A diamond transducer design advanced by Dr. Peter Kellman [16] was chosen that smoothes out the acoustic diffraction pattern. The specifications and the results of the characterization of the AOD are presented in appendix IIb of this chapter. Our conclusion from the investigation of AOD's is that, as

expected, they do not impose any major limitations on the performance of the TSI architectures. The accuracy, bandwidth and processing power of these processors are limited by other components in the system, primarily the detector. This is in contrast to conventional 2-D optical processors where the real time 2-D spatial light modulator is the major source of performance degradation.

3. CCD detector arrays. 2-D CCD arrays are used in the TSI architectures as the optical detector. In addition, the unique capability of CCDs to transfer photogenerated charge along one of the dimensions of the array proves to be very useful in the synthesis of the most powerful TSI architectures. Therefore investigation of the CCD's had a two-fold purpose; determination of the limitations imposed by the CCD on overall system performance and identification of the optimum CCD structures for the shift-and-add (or TDI) mode of operation. Our investigation and experiments were based exclusively on commercially available CCD's. Very substantial improvements in performance can be realized with devices specifically designed for this application, but the cost of a custom CCD array proved prohibitive.

Imaging CCD's have been studied and characterized extensively previously [17, 18]. In what follows we will stress the parameters of the CCD that directly affect the performance of the TSI architectures and report the results from our experiments with these devices. At present the CCD imposes the major limitation in the accuracy, bandwidth and processing power (space-bandwidth product) of TSI architectures. The accuracy is essentially determined by the linear dynamic range of the CCD. The dynamic range is determined by the following equation.

$$D.R. = \frac{N_s - N_d}{N_n}, \quad (6)$$

where  $N_s$  is the number of photogenerated electrons that will cause a pixel of the CCD to saturate,  $N_d$  is the average number of thermally generated (dark)

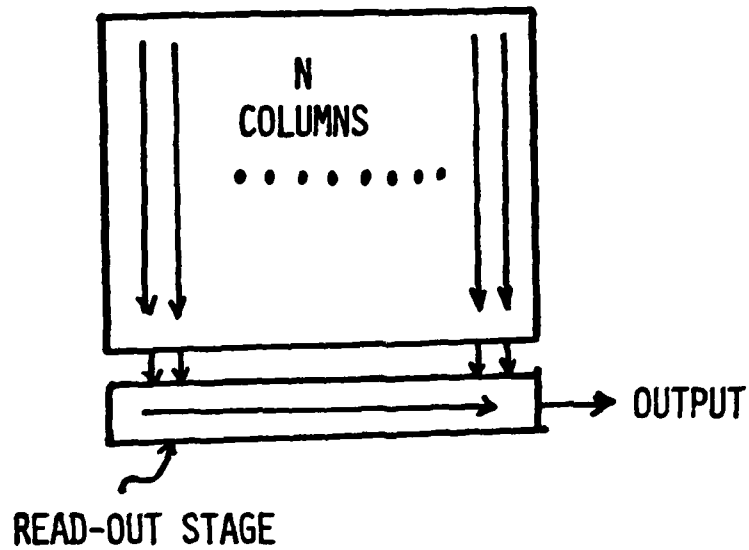
electrons that accumulate in one pixel during each integration period and  $N_n$  is the number of noise electrons (standard deviation).  $N_s$  is limited by geometric factors and the potentials at which the CCD is operated. It is crucial to keep  $N_s$  well below full saturation, to avoid non-linearities but more importantly to avoid blooming (charge spilling over to adjacent pixels) which degrades resolution. We have experimented with CCDs manufactured by RCA and Fairchild and in both instances we have found that we can comfortably work with  $N_s \approx 10^5$  electrons.  $N_s$  could be conceivably increased, by perhaps an order of magnitude, by incorporating anti-blooming mechanisms in the device and increasing the size of the potential well. The dark current,  $N_d$ , is of course a strong function of temperature. We have found that at room temperature  $N_d = N_s/2$  for an integration period equal to one second.  $N_d$  decreases linearly with decreasing integration time until the plateau of the dark current from the read-out electronics is reached. The dark current can be eliminated almost entirely by cooling the device. Several sources contribute to the total number of noise electrons; shot noise due to the signal and the dark current, read-out (thermal) noise, clock feedthrough, off-chip amplifier noise, fixed pattern noise (the variation of dark current, from pixel to pixel). We measure  $N_n$  to be equal to 150 electrons for 1 second integration time. In this case the dynamic range of the RCA device is measured to have 400:1 dynamic range. At shorter integration times the dynamic range is expected to increase because of the dark current decreases linearly with the read-out-rate, whereas the noise increases proportionally to the square root of the read out rate. At present, however, our noise floor is limited by clock feedthrough (the clock waveforms that are applied to the CCD to cause the charge transfer are picked up on the video line) and at shorter integration times the dynamic range does not improve. An improved design of the high frequency electronics that isolates the clock circuits from the video lines is expected to improve the dynamic range to more than  $10^3$ :1 at room temperatures. Furthermore, cooling the device will further

reduce the noise in addition to the dark current. Finally, the fixed pattern noise is eliminated along one of the dimensions of the CCD when it is operated in the shift-and-add mode. We expect that we will be able to observe a dynamic range well over  $10^3:1$  (compared to the present 400:1) and is feasible to obtain  $10^4:1$  with present CCD technology. For large 2-D CCD arrays, a substantial improvement beyond that will come only with advances in the state-of-the art of CCD technology. With the present dynamic range of the CCD, the effects of AOD nonlinearities and spatial non-uniformities are not detectable, in most instances and the system accuracy is essentially limited by the CCD.

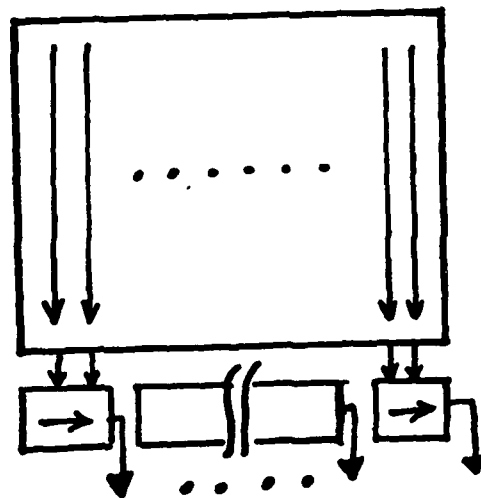
The speed at which charges can be transferred on the CCD and also read-out sets the limit on the through put of the optical processor. We should stress here the distinction between bandwidth and throughput. The bandwidth is limited by the AOD and it can be as high as several hundred MHz. If the results of the optical computations cannot be read-out at this rate then we must either reduce the input bandwidth or cease entering data periodically to allow the CCD to catch up. In this case the throughput is smaller than the bandwidth. This situation typically arises in radar processing (see chapter V) where signals with very large bandwidths can be processed, but since the pulse repetition frequency of radars is typically several KHz, the CCD is read out very slowly. In general however, the CCD imposes a speed limitation well below what state-of-the-art AOD's can provide. The CCD bandwidth is fundamentally limited by the time it takes for a charge packet to be transferred from one pixel to the next. This depends on factors such as the mobility of charge carriers, the voltage levels at which the CCD is operated and the center-to-center separation between pixels. In practice, when we work with commercially available CCD's, the speed can be limited by the bandwidth of the on-chip amplifier and the off-chip driving and read-out electronics.

Particularly for large 2-D arrays it becomes quite an engineering challenge to build fast driver circuits that can switch faster than 100 nsec (10MHz). We have driven CCD's in the shift-and-add mode with our circuits, at rates up to 10MHz. This rate is sufficient for the majority of our experiments (e.g. 512x512 images can be processed at 30 frames per second). For high speed applications it will not be possible to increase the 10MHz rate substantially without a custom CCD. The speed limitations arise because of the bottleneck formed by the read-out register, as shown in Figure 3a. All the columns of the device feed into a single horizontal CCD. If the horizontal register is clocked every 100 nsec, then the vertical registers cannot be clocked faster than every  $N \times 100$  nsec, where  $N$  is the number of columns in the CCD. CCD's however can be fabricated with multiple read-out stages as shown in Figure 3b. For instance a device with 10 parallel read-out channels can be read-out at 300 frames per second with present CCD technology. Furthermore, GaAs CCD technology allows bandwidths of  $10^8$ - $10^9$  Hz. This technology is still at the research and development stage, but it now appears that we are near the threshold of having system grade and probably commercially available devices. In conclusion, the CCD imposes at present the limitations in speed on the TSI architectures. The limitation however is not fundamental and we can safely expect to overcome it as CCD technology advances in the coming years. TSI architectures operating at  $10^8$ - $10^9$  Hz rates ( $10^2$ - $10^3$  frames/second for image processing) are feasible.

The size of commercially available CCD cameras is typically around  $10^5$  pixels, arranged in various formats. We have worked primarily with the RCA device which has 512 pixels in the shifting dimension and 320 pixels in the other dimension. Larger CCD's have been fabricated. For instance an 800x800 device has been built by Texas Instruments for use in the Space Telescope and the Galileo mission, for



(A)



$M$   
OUTPUT PORTS  
(B)

FIGURE 3. A) CCD ARRAY WITH A SINGLE  
READ-OUT REGISTER  
B) CCD ARRAY WITH MULTIPLE  
(PARALLEL) READ-OUT PORTS.

NASA. The same company plans to produce a commercial device with over  $10^3 \times 10^3$  pixels in the next few years. The space-bandwidth product of AOD's and the optical system is typically  $10^3 \times 10^3$ . Therefore current devices place the limit on the resolution of the overall system, but it is expected that this will be overcome in the near future as larger arrays become available.

Most commercially available CCDs are constructed in one of two architectures: frame transfer or line transfer. In the frame transfer devices, the CCD potential wells are themselves photosensitive. For instance, in a three stage CCD, the first stage of each pixel is held at a high potential during exposure and the photogenerated charge accumulates there. In the imaging mode, the entire charge, stored in the array is clocked out after each exposure. In the TDI mode the charge is transferred by only three stages, (one pixel) after each exposure. Therefore a relatively minor adjustment in the timing circuits is required to convert frame transfer devices to TDI operation. The RCA device with which we did the majority of our experiments is a frame transfer device and a variety of experimental results with this device are reported in Chapter V. The structure of line transfer devices, shown in Figure 4, is considerably more complex. Light is detected by an array of photodiodes and the photogenerated charge is transferred to an adjacent CCD through a single gate. Such devices can be operated in the TDI mode in one of two ways. The gate can be held open continuously allowing the photogenerated charge to flow from each photodetector to the corresponding pixel of the CCD during exposure. Alternatively, the gate can be opened periodically only after each exposure. We have experimented with both methods, with the second giving slightly better results in terms of dynamic range. Line transfer devices, in addition to being more complicated to operate in the TDI mode pose another, more fundamental problem. As the charge accumulates



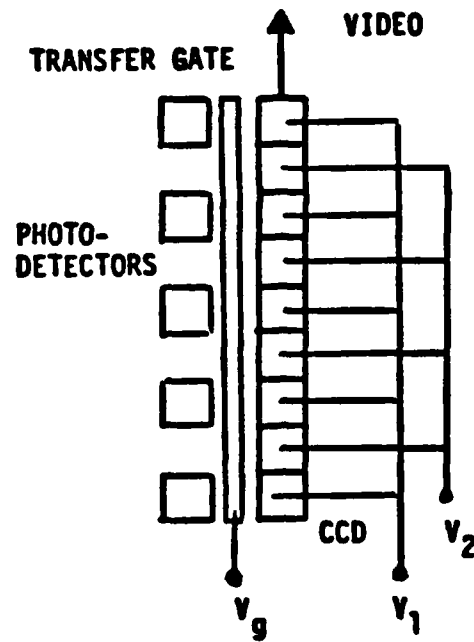


Figure 4. Line-transfer CCD array

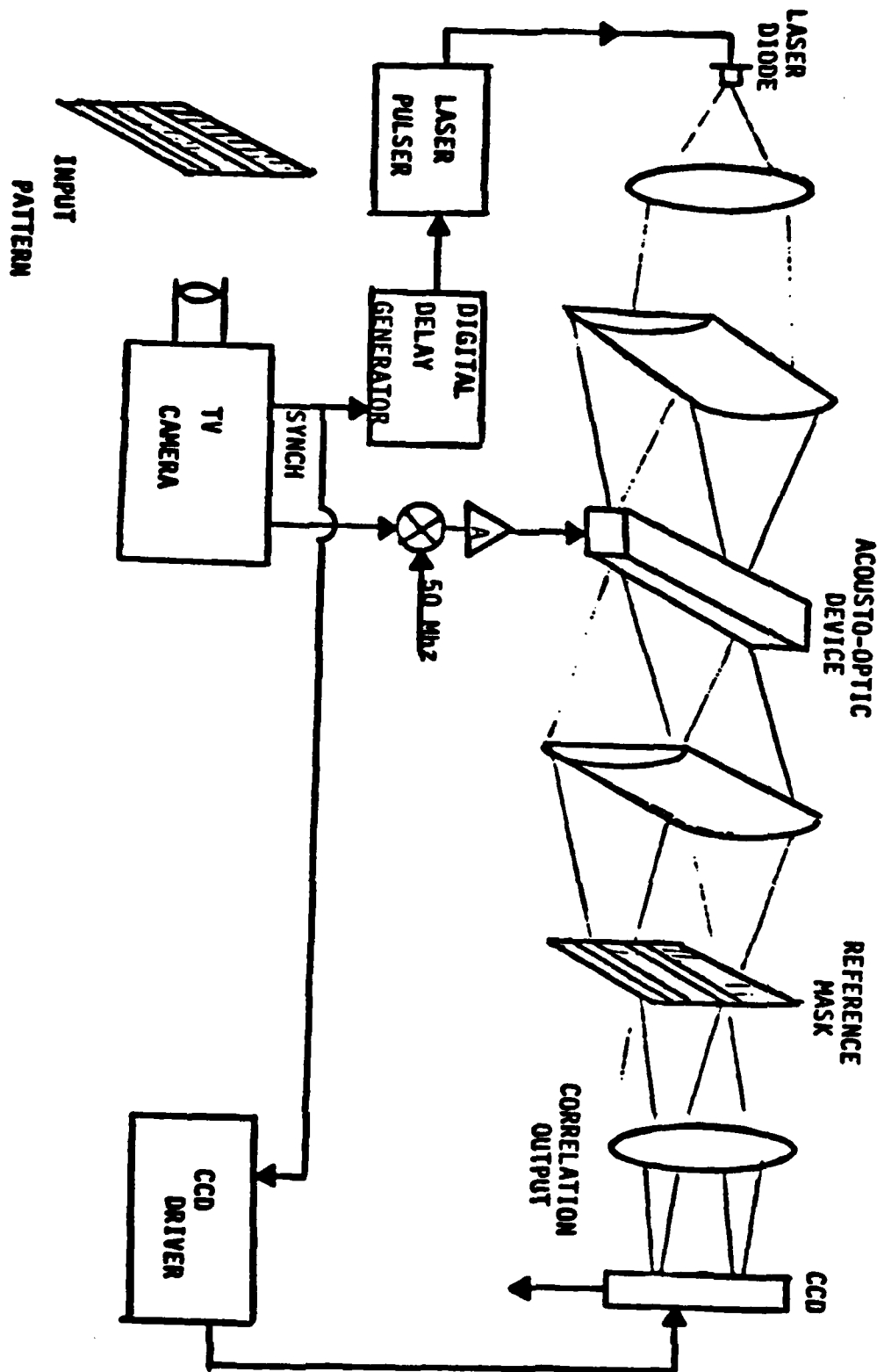


Figure 5. Experimental correlator used to test the line transfer CCD.

in each pixel of the CCD, we are trying to transfer new photogenerated charge from the detectors into the partially filled CCD well. The efficiency of charge transfer therefore decreases and the result is a reduction in dynamic range and resolution. The reasons we experimented with line transfer devices is because they are more readily available and in various array sizes (primarily through Fairchild). For instance, all the available 1-D CCDs are line transfer devices. Figure 5 is a schematic diagram of a simple experiment we performed with the 1-D Fairchild CCD operating in the TDI mode. An input pattern consisting of two horizontal slits was detected with a TV camera and the video signal from the camera was heterodyned to 50 MHz (the center frequency of the Acousto-optic device) and applied to the AOD. The Sync signal from the TV was used to trigger the pulsed laser diode to produce a light pulse every time a video line was present in the AOD. The light diffracted by the AOD illuminated a mask consisting of two slits also and the mask was imaged onto the CCD array. The CCD was operated in the shift-and-add mode in synchronism with the video signal from the TV camera. The output signal from the CCD is the correlation of the double slits in the input pattern and the mask placed in the optical system. The signal in Figure 6a was obtained by blocking one of the slits in the input pattern and obtaining the correlation between the single remaining slit and the double slit of the mask. This is in effect an image of the mask. Similarly in Figure 6b an image of the input pattern is shown by blocking one of the slits in the mask. In Figure 6c the signal obtained with all slits open is shown and the correlation between the signals in Figures 6a and 6b is obtained. Some of the experiments reported in Chapter V also use this type of CCD.

We conclude this chapter by noting that the performance of the TSI architectures is limited primarily by the CCD detector. The majority of these limitations



Figure 6. (a) Input pattern  
(b) Image of the mask  
(c) Correlation of input and mask

(speed, space bandwidth product) are not fundamental to the technology of CCD's, but rather a consequence of the fact that existing commercial devices are intended for TV camera applications and they can be overcome by a custom designed device using current technology. The dynamic range of the present devices ( $10^3:1$ ) is adequate for some applications (e.g. pattern recognition) but a dynamic range of  $10^4:1$  is required for others (e.g. SAR). It is also the one characteristic of CCDs that will require advances in the state of the art of the technology to provide an improvement of more than one order of magnitude ( $>10^4:1$ ). The dynamic range issue is particularly important in TSI architectures because a portion of the dynamic range is typically allocated to a bias term, so that bipolar signals can be represented. Issues relevant to dynamic range are addressed in the next chapter.

## Appendix IIIa

### COHERENCE PROPERTIES OF PULSED LASER DIODES

Michael Haney\* and Demetri Psaltis

California Institute of Technology  
Department of Electrical Engineering  
Pasadena, CA 91125

#### ABSTRACT

Laser Diodes are becoming increasingly attractive for application to time integrating and systolic optical computing architectures where large bandwidths and coherent processing are required. This paper reports the results of a study to determine the interferometric performance of laser diodes when used in a pulsed mode and where the interference effects of many sequential pulses are integrated temporally. The results indicate that fringe visibility is high for as many as  $10^4$  integrated pulses if the OPD in the processor is less than 5 mm and the laser pulse width is less than 50 nsec.

#### INTRODUCTION

The continual rise in the quality of performance and affordability of commercially available Laser Diodes (LD) has made them viable for use in many types of optical computers. The attractive features of LDs include: Their small size and relative ruggedness, their high efficiency and hence low electrical power requirements, their ability to be modulated directly with large bandwidths and, in the case of single longitudinal mode LDs, their large coherence lengths. These features make LDs applicable to many time integrating and systolic architectures, some of which employ coherent processing techniques that impose stringent requirements on the light source. In particular, the CCD/AO optical computers now being developed at Caltech for image processing and radar imaging applications [1,2] require a light source with a bandwidth of 1 GHz and peak output power of at least 10 milliwatts. The light source is to be pulsed in synchronism with a master clock with pulse widths of 10-100 nanoseconds. Furthermore the time-integrating and interferometric detection employed in the CCD/A-O processors impose the need for a high degree of uniformity from

\* Mr. Haney is with General Dynamics Corp., Pomona, CA and is currently attending Caltech on a corporate sponsored PhD fellowship

pulse to pulse in the coherence properties of the light source. The coherence requirement is based on the fact that the interferometric detection scheme used in the CCD/A-O optical computers will have OPDs of as much as 2 millimeters. The prime candidates for the light source of these processors are single longitudinal mode LDs which have cw coherence lengths of many centimeters and also have the required output power and bandwidth. While the cw coherence length of single mode LDs is known to be adequate, the pulsed coherence properties of these devices is not thoroughly understood. At issue is the "coherence time" of the LD, i.e. the time after the onset of laser oscillation in which the LD changes from its initial multi-mode oscillation to single mode. Also of interest is the stability of the mode in which the laser is emitting over the duration of the pulse. Lastly, since the light from many LD pulses is to be temporally integrated, the pulse-to-pulse coherence properties of the device must be understood.

An interferometric experiment was devised to characterize the pulsed coherence properties of single longitudinal mode LDs, the results of which are reported in this paper. Two commercially available LDs were evaluated, the Hitachi HLP-1600 and the Mitsubishi ML-3001. In the evaluation we concentrated on the HLP-1600 because, due to its higher peak power capability, it was more applicable to the CCD/A-O architecture. The HLP-1600 is capable of peak output power of 15 mW while the ML-3001 is limited to 3 mW.

A description of the pulsed coherence measurement experiment is contained in section 2 of this paper. The experimental results are presented in section 3 with the interferometric performance tradeoffs in pulse width, amplitude and LD biasing presented. Section 4 of this report is a discussion of the results in which a brief analysis is given.

#### EXPERIMENT

The LD pulsed coherence measurement set-up is shown schematically in Figure 1. The heart of the experiment is a Michelson Interferometer consisting of mirrors M1 and M2 and the beam splitter B1.

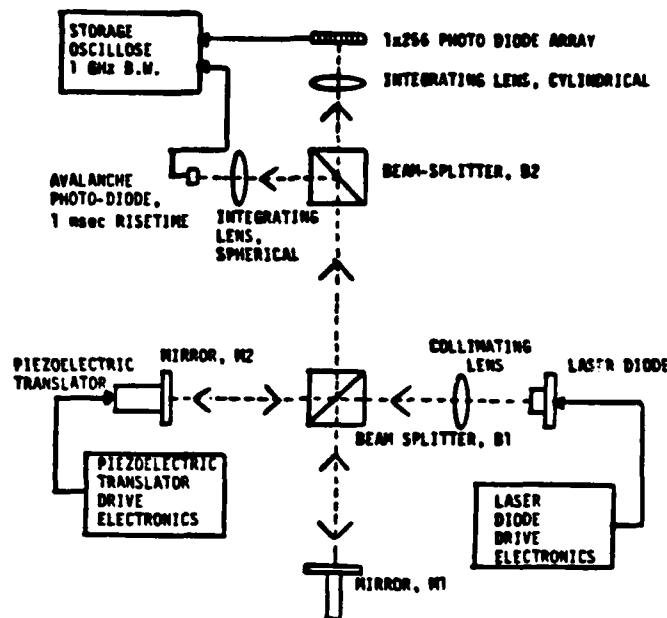


FIGURE 1

Mirror M1 is mounted on a micrometer stage to allow variations in OPD from 0 to 5 cm. Mirror M2 is mounted on a piezoelectrical translator. The translator is capable of being driven at frequencies of up to 5 KHz with the amplitude of translators varying by  $\pm \lambda/2$ . Modulation of the OPD in this manner is a convenient method for measuring fringe depth at the output of the interferometer. The Laser drive electronics consist of a current pulser with a dc biasing capability and a rise/fall time of 7 nanoseconds. Figure 2 is an oscilloscope trace of a typical LD drive pulse.

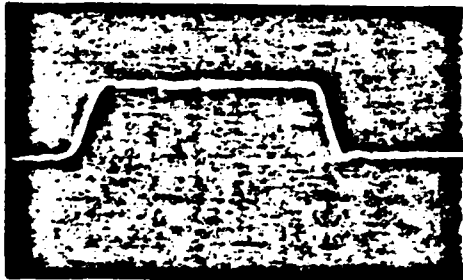


Figure 2.

The output of the interferometer is detected by both a high-speed avalanche photodiode (APD) and an integrating photodiode linear array (PDA). Beam splitter B2 permits simultaneous data collection with the two types of detectors. Both of the detectors employ integrating lenses to increase the level of the detected light. The APD that was used is capable of measuring rise times of individual light pulses that are less than 1 nanosecond with a sensitivity of 1 mV/ $\mu$ W. The PDA temporally integrates the light of many sequential

pulses in order to measure the pulse-to-pulse coherence of the LD. When data is being taken with the PDA the two output beams of the interferometer are made to be slightly misaligned along the dimension of the PDA by tilting mirror M1. This causes a linear fringe pattern on the array with a spatial frequency determined by the angle between the output beams. The fringe visibility of the light integrated on the array is thus a measure of the uniformity of the coherence over many pulses. The integration time of the PDA is variable to allow for the integration of 200 - 10,000 pulses. The interferometric detection on the PDA is analogous to that in the CCD/A-O processors in which the LD is used. In this application approximately 500 light pulses are integrated.

The output from the detectors is displayed on an oscilloscope for analysis. A 1 GHz bandwidth storage oscilloscope is used to accommodate the high speed of the APD.

The coherence time is estimated by measuring the time from the beginning of detectable light intensity to the time of maximum fringe visibility. This is accomplished by modulating the APO with Mirror M2 by  $\pm \lambda/2$  at a high rate ( $\sim 1$  KHz) with the piezoelectric translator so that the response to many individual pulses will appear simultaneously on the screen of the oscilloscope due to the persistence of the screen's phosphor. Therefore the trace is "smeared" because all possible relative phases of the interfering beams would be detected as different intensity amplitudes. However, during the start-up period of the pulse, when the light is incoherent, the smearing does not occur and thus the trace of many pulses appears as a single line. The coherence time is approxi-

mately the difference between the time light is first detected as a single trace and the time of maximum smearing of the light intensity due to interference.

The intra-pulse stability of the lasing mode is measured by studying the trace of the output of the APD for a single pulse of light from the interferometer. The amplitude of the light as a function of time is determined by the relative phase of the two interfering beams. If the beams are in phase maximum intensity will be detected; if the beams are 180 degrees out of phase, minimum intensity will be detected. At a given OPD this relative phase will change in a predictable manner with lasing wavelength. The ramifications of the intra-pulse stability of the lasing mode will also be measurable on the output of the PDA as a change in the fringe visibility of the interference pattern of the many integrated pulses.

The inter-pulse stability of the laser is determined by observing the time history (i.e. relative phase of the two beams) of many light pulses with the APD. The fringe pattern displayed on the PDA is also influenced profoundly by the inter-pulse stability of the lasing mode.

The primary variables in this experiment are the OPD of the interferometer, the pulse width of the light pulses, the peak output power of the laser diode, and the biasing conditions of the LD. All of these variables will have a strong influence on the fringe visibility that would be achievable in an optical computer employing a pulsed LD.

### RESULTS

The overall result of this study is that pulsed LD's become coherent (i.e. single mode) very rapidly after the onset of laser oscillation (within about 1 nanosecond), but that the interferometer performance of a processor employing laser diodes in this mode can be limited by three distinct effects. These effects occur when the OPD is nonzero

and are related to the electrical operating conditions and/or the rise in temperature of the junction area of the laser during the pulse. The first effect observed is the continuous and oscillatory variation in the intensity of the interfering beams during a single pulse due to a continuous shift in the lasing wavelength. This effect is caused by a shift in the index of refraction of the junction area in the laser with temperature. The second effect that was observed is that, although each laser pulse becomes single mode rapidly, the actual longitudinal mode selected by the laser in which to oscillate, may be different from pulse to pulse (i.e. the laser selects one of two adjacent Fabry-Perot cavity modes) leading to a possible reduction in fringe

depth when the integration of many such pulses occurs. The third effect encountered in this study is the occasional occurrence of a rapid (much less than 1 nanosecond) mode hop during the period of a single pulse leading to a possible step discontinuity (depending on the OPD) in the measured intensity of the interfering beams within the period of a single pulse. The magnitude of this step is directly related to the OPD of the system. The details of the measurements of these three effects are presented in the following paragraphs.

Figure 3 shows the leading edge interferometric activity of the laser diode. The data in figure 3 are oscilloscope traces of the output of the APD in which many interferometer output pulses are displayed simultaneously. The OPD for the multiple pulses in each trace are all different,



Figure 3a



Figure 3b

leading to the smeared appearance in the trace. This effect is caused by the modulation of the position of Mirror M2 by  $\pm \lambda/2$  and using the persistence of the oscilloscope screen as described in Section II. The top of the envelopes in the traces of Figures 3a and 3b correspond to the intensity measured for maximum constructive interference, while the bottom of the envelope corresponds to total destructive interference. In Figure 3a the first 11 nanoseconds of a 50 nanosecond pulse are shown for the case of zero OPD. The rippling in the maximum light level is due to slight impedance mismatches in the electronic drive circuitry and also possibly to relaxation oscillations in the laser diode. The time scale in Figure 3a is 2ns/div and thus it is obvious that the laser is fully coherent within about 1 nanosecond from the start of measurable light intensity. The first 8 nanoseconds of a 50 nanosecond pulse for the case of OPD = 1 cm is shown in Figure 3b, with a time scale of 1 ns/div. The coherence time of this pulse can be seen to be on the order of 1.5 nanoseconds. Both cases shown in Figure 3 correspond to approximately 15 mW peak output power with no dc bias current used. Pre-biasing the laser to a dc level at the threshold current of the laser reduced the coherence time slightly from the case of no bias but accurate



measurements of the effect are difficult because of the short (sub nanosecond) time scales involved. The final interesting feature of the data in Figure 3 is that the pulse rise times are on the order of 1 nanosecond despite the fact that the current drive pulse has a risetime of about 7 nanoseconds (see Figure 2.) This effect is probably due, at least in part, to the finite time delay before the start of laser oscillation while the injected carrier concentration builds up in the depletion region of the laser diode.

The effect on the interferometric performance of a continuous shift in the lasing wavelength is shown in Figure 4. Figure 4 consists of 2 oscilloscope traces of the output of the APD for a single laser pulse. The effect of the continuously shifting wavelength is a change in the relative phase of the interfering beams and thus a modulation of the intensity that is detected within the pulse. Shown in Figure 4 are two 800 nanosecond pulses, one at OPD=2 cm and the other at OPD = 4 cm. The number of cycles present in the intensity modulation during the pulse is proportional to the OPD and therefore Figure 4a shows twice as many cycles as Figure 4b.



Figure 4a.

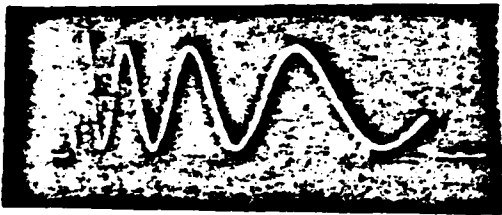


Figure 4b.

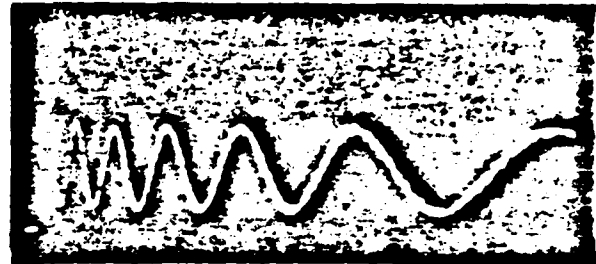
The phase of the intensity modulation is directly proportional to the change in junction temperature and thus each cycle of modulation corresponds to a fixed  $\Delta T$  in the junction for a given OPD. It is further noted that the frequency of the intensity modulation is highest in the early part of the pulse indicating that the temperature rise is most rapid at the beginning of the pulse.

The effects of pre-biasing and peak power are shown in Figure 5. All the pulses in Figure 5 have a pulse width of 2  $\mu$ sec. And were taken at an OPD of 4 cm. Figures 5a and 5b show the interferometer output for laser peak output power

of 15 and 8 milliwatts respectively, with no dc biasing. The fewer modulation cycles in Figure 5b indicate less change in temperature after 2  $\mu$ sec. Figure 5c and 5d show the effect of biasing the laser at its threshold current level before application of the current pulse for 15 and 8 milliwatts laser output power respectively. The dramatic reduction in the number of cycles indicates that pre-biasing raises the temperature



a



b



c



d

Figure 5

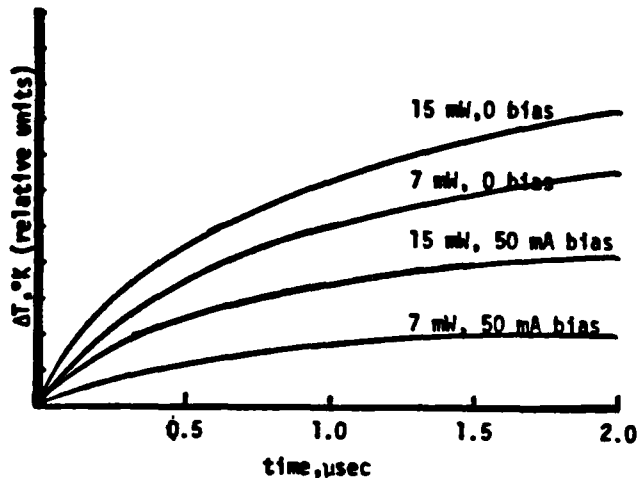
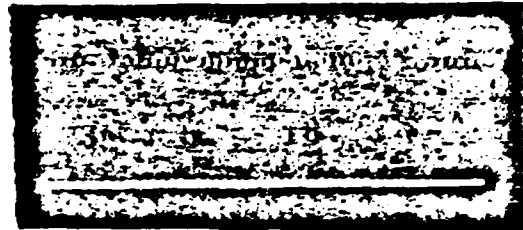


Figure 6.

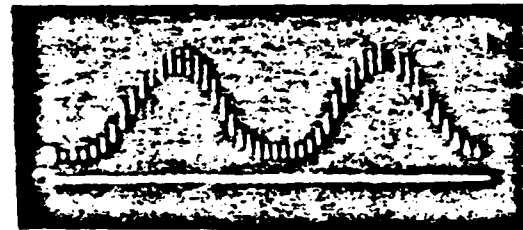
of the laser such that the change in temperature during the application of the pulse is less than with no biasing. The data of Figure 5 is plotted in Figure 6 where the phase of the amplitude modulation is used as a measure of junction temperature change with time. The data clearly show an exponential nature of the temperature rise with time constants that are on the order of several hundred nanoseconds. It should be noted that the data shown in Figures 4 and 5 indicate that these pulses would be useless for interferometric detection purposes due to the variation from constructive to destructive interference within a single pulse. For the much shorter pulse widths and OPDs to be used in the CCD/A-O processors, only fractions of a cycle of intensity modulation will occur during a pulse rendering it still useful for interferometric purposes. The effect of this phenomenon on the fringe depth for the integration of many pulses is discussed at the end of this section.

The effect of sequential laser pulses oscillating in different longitudinal modes is shown in the oscilloscope traces of Figure 7. All three traces in Figure 7 are of the APD output with a large time scale to show a series of pulses. In Figures 7b and 7c (which have different time scales) the OPD was modulated by  $\pm \lambda/2$  at a frequency of 1 KHz to show the achievable degree of interference. The rate of the laser pulses is 20 KHz and a short pulse width ( $\sim 50$  nsec) and OPD were used to minimize the effects of the inter-pulse wavelength changes. The OPD for this data is approximately 1 mm. The observed effect of this type of multimode behavior is different measured interferometric amplitudes of laser pulses that are oscillating in different modes. The amplitude difference is a manifestation of the different relative phases of the interfering beams. This phase difference is a function of the intermode spacing of the laser cavity and the OPD. At certain discrete OPD's (for this laser this spacing is integral multiples of 2.42 mm) the relative phases of the interfering beams are the

same in the interferometer for adjacent modes. The examples in Figure 7 illustrate a severe case in which the OPD was chosen to show large phase differences in the interference of adjacent longitudinal modes. This intermode instability was found to be a strong function of peak power and the choice of operating point for the laser. At output power levels of 1/2 maximum the intermode stability was found to be >95%



a



b



c

Figure 7.

The third phenomenon that was found to affect the interference properties of the laser diode is a sudden switch in mode within the period of the pulse. Figure 8 illustrates the effect of this on the detected intensity of the interfering beams. At the given OPD, the change in mode during the pulse resulted in a step change of approximately 180 degrees in the phase of the intensity modulation. The frequency of mode hopping was found to be a strong function of pulse width and electrical operating point and is reduced to an insignificant level by using shorter pulses, dc biasing, and output power of approximately 1/2 maximum.

Evaluation of the effects of the three types of mode instabilities described above on time integration interferometry was accomplished by studying the output of the PDA. The effects of

intra-pulse mode hopping and inter-pulse mode changes were reduced to an insignificant level as described above, leaving only the continuous shift in lasing wavelength with temperature as the dominant factor affecting the interferometric performance. Figure 9 is an oscilloscope trace of the PDA output. The fringe frequency shown represents a spatial frequency of about 2 lines/mm on the array. The trace shown represents the



Figure 8.

time integrated interferometric response of approximately 10,000 individual laser pulses over a period of 50 milliseconds. The data shown was taken at zero OPD and thus represents the largest attainable fringe depth. The actual fringe depth achieved is not 100% because of several non-idealities of the system. First, the PDA has dark noise which contributed to the bias. Second the very short multimode portion at the beginning of each pulse will add incoherently to result in a contribution to the bias. Lastly, nonidealities in the measurement set-up, such as misalignment of the integrating lens and signal spreading on the array could lead to bias contributions.

As OPD is increased the fringe visibility decreases due to increased variations in the amplitude of the interfering beams with increasing temperature during the pulse. In addition, longer pulses will have more variation intensity over the length of the pulse which tends to "wash out" the fringe pattern. The effect of OPD and pulse width on fringe visibility is plotted in Figure 10. This data can be used to define a maximum pulse width than can be used for a given OPD.

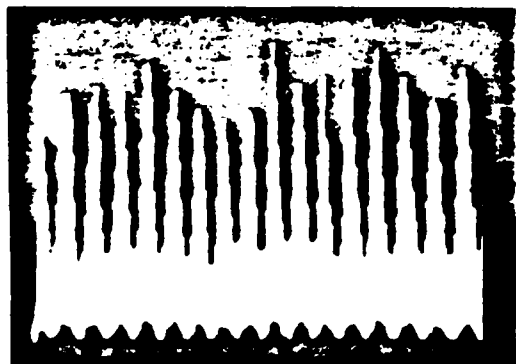


Figure 9.

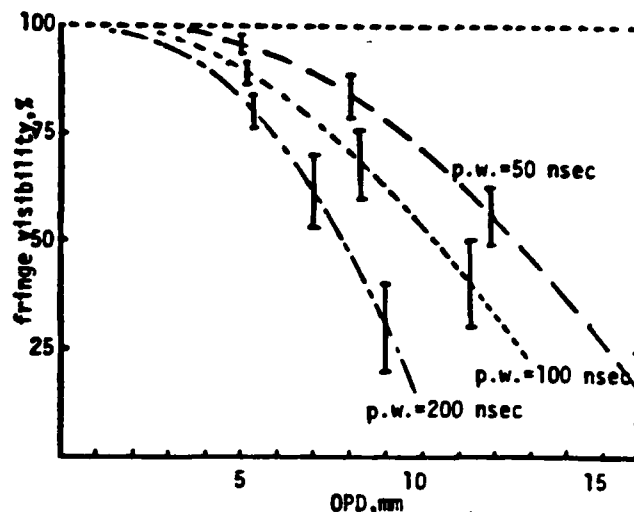


Figure 10.

### DISCUSSION

For a single longitudinal mode laser diode the lasing wavelength is determined by the length and index of refraction of the laser cavity. The laser will oscillate in one of the Fabry-Perot modes [3,4] of the cavity given by the following condition:

$$q \frac{\lambda}{2} = nL \quad (1)$$

where  $\lambda$  is the wavelength,  $L$  is the length of the cavity,  $n$  is the index of refraction and  $q$  is an integer. The change in wavelength with temperature is then given by

$$\lambda' = \frac{d\lambda}{dT} = \frac{2}{q} \left( n \frac{dL}{dT} + L \frac{dn}{dT} \right) \quad (2)$$

For the HLP-1600, which is double hetero-structure GaAlAs device,  $L = 300 \mu\text{m}$ ,  $n = 3.5$ , and the lasing wavelength is approximately  $.83 \mu\text{m}$ . The value of  $\lambda'$  for the HLP-1600 is approximately  $.06 \text{ nm}/^\circ\text{K}$  [5]. The change in index of refraction with temperature is the dominant factor in  $\lambda'$ .

The amplitude of the intensity of the interfering beams is proportional to the phase difference  $\Delta\phi$  of the waves:

$$\Delta\phi = \frac{2\pi}{\lambda} (\text{OPD}) \quad (3)$$

The change in phase difference with changing  $\lambda$  is then given by

$$\left| \frac{d(\Delta\phi)}{d\lambda} \right| = \frac{2\pi}{\lambda^2} (\text{OPD}) \quad (4)$$

Finally we can use equations (2) and (4) to determine how the temperature change will affect the measured phase difference in the interferometer:

$$\frac{d(\Delta\phi)}{dt} = \frac{2\pi (OPD) \lambda^{-1}}{\lambda^2}$$

The transient behavior for the rise in junction temperature during the beginning of laser oscillation has been modeled as follows [6]

$$\Delta T(t) = \Delta T_0 (1 - e^{-t/\tau})$$

where  $\Delta T_0$  is the asymptotic value of the junction temperature change,  $\tau$  is the thermal time constant which is determined by the thermal resistance and capacitance of the junction. The thermal time constant,  $\tau$  is typically several hundred nanoseconds. The model closely follows the measured data shown in Figure 6.

The overriding conclusion that are drawn from the results of this study is that the coherence properties of pulsed laser diodes are influenced predominantly by the transient rise in junction temperature during the time period of the pulse. These thermal effects limit the useful pulse width for coherent processing to a maximum of approximately 50 nsec for an OPD of 5 mm. The minimum pulse width is limited by the coherence time constant of the laser diode which is found to be 1-2 nsec. Inter-pulse and intra-pulse mode hopping will also affect the coherence properties but can be made negligible by a proper choice of electrical operating conditions. An important operating condition that should be employed is a dc bias at the threshold current level of the laser diode. The laser diode was shown to have very consistent coherence properties for thousands of sequential pulses and thus is suitable as the light source of the CCD/A-O processors.

#### ACKNOWLEDGMENT

The support by General Dynamics for Michael Haney's research at Caltech is gratefully acknowledged.

The work reported in this paper is sponsored by the Air Force Office of Scientific Research and in part by NASA/JPL

#### REFERENCES

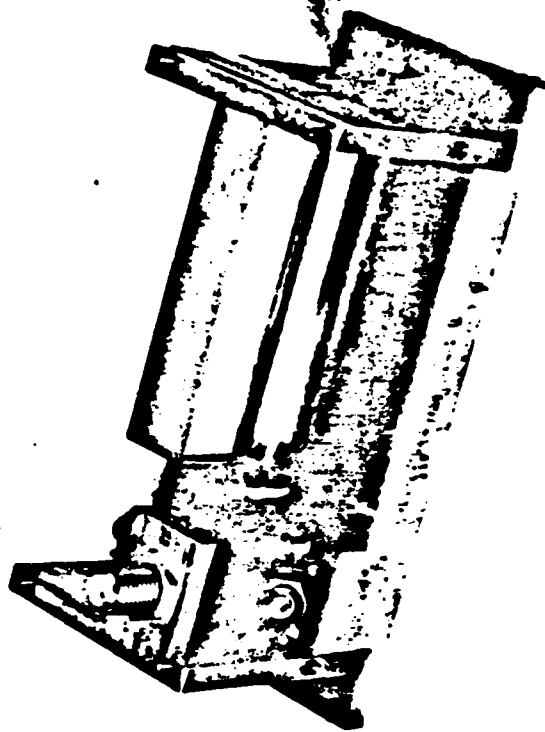
1. D. Psaltis, Appl. Opt., 21, 491 (1982)
2. D. Psaltis and K. Wagner, Optical Engineering, 21, 822 (1982).
3. Yariv, A., Quantum Electronics, 2d Ed. New York, Wiley, 1975
4. Sze, S., Physics of Semiconductor Devices, 2d Ed. New York: Wiley, 1981.
5. Hitachi Laser Diode Application Manual
6. Butler, J., The effect of junction heating on laser linearity and harmonic distortion, in Topics in Applied Physics, Vol. 39, Chap. 8 Springer-Verlag, Berlin, 1980.

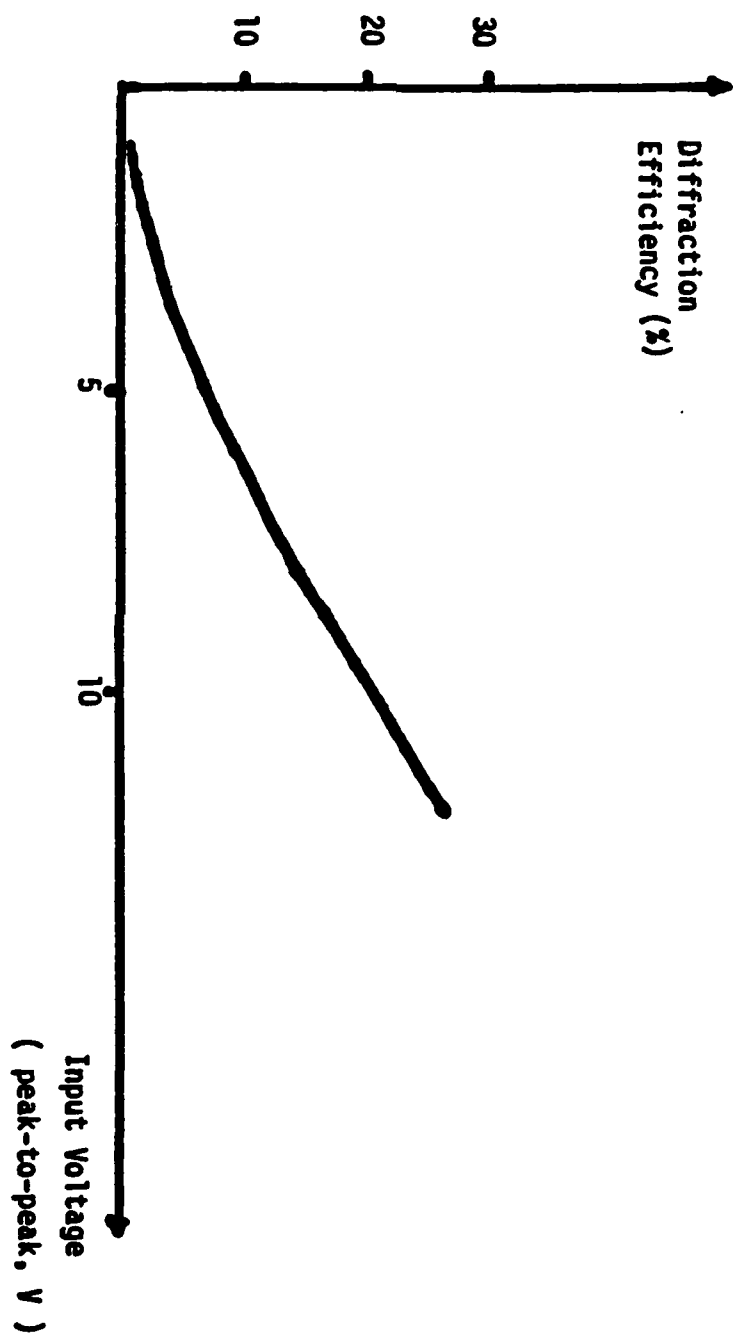
June 7, 1983

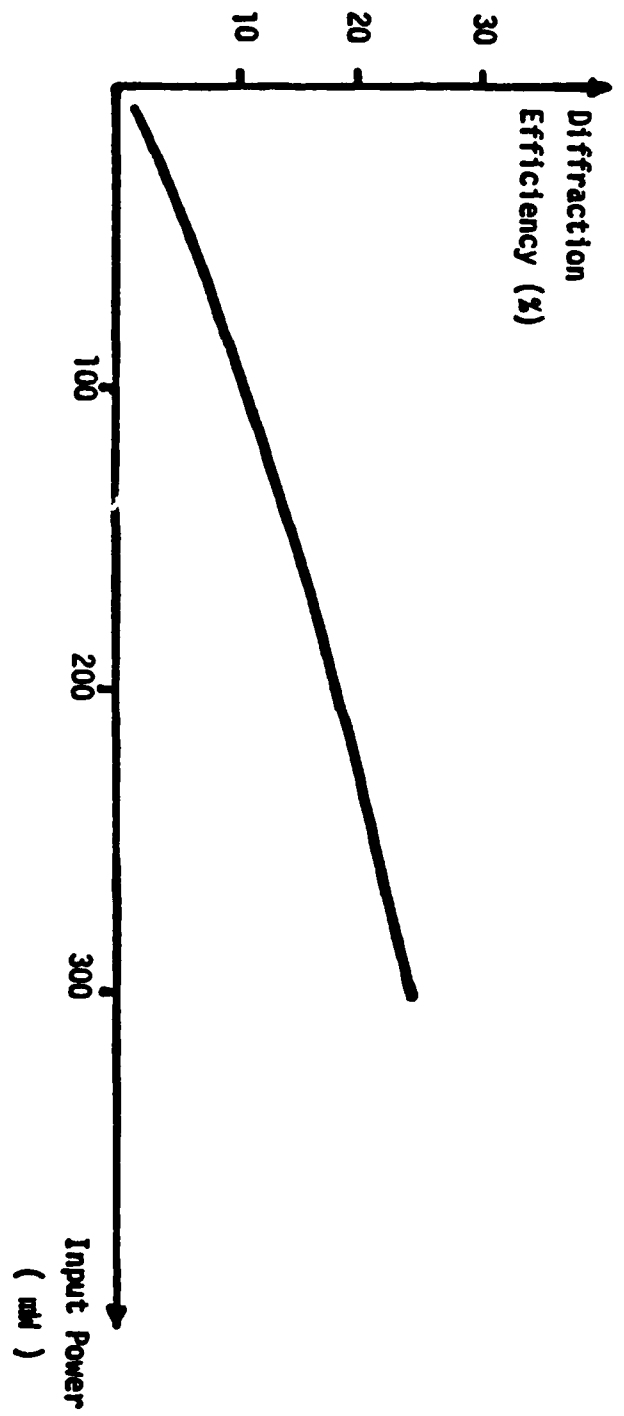
Appendix IIIb

DATA ON  $\text{TeO}_2$  ACOUSO-OPTIC DEVICE

Model No. 2050-3-003





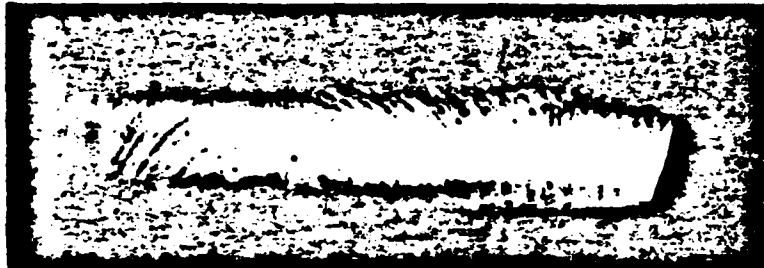




Schliferen Images



35 MHz

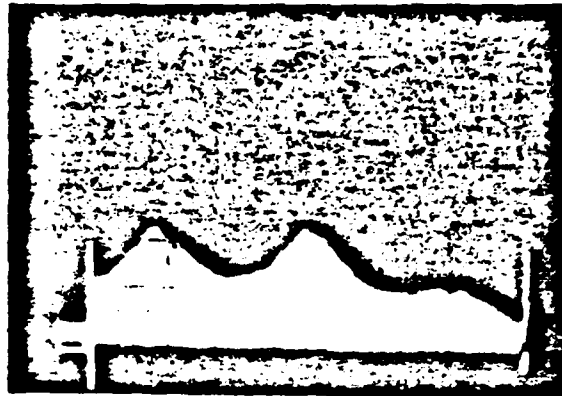


50 MHz

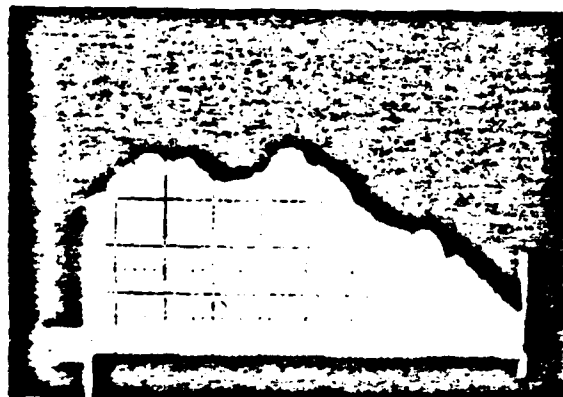


65 MHz

Bandshapes



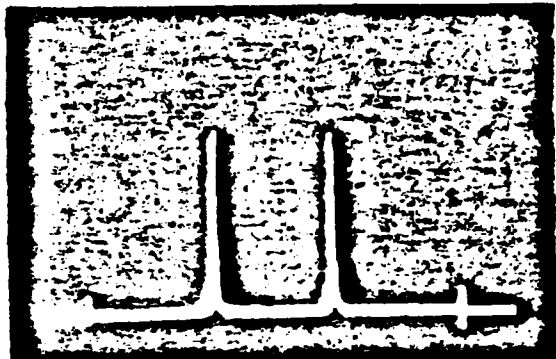
250 mW



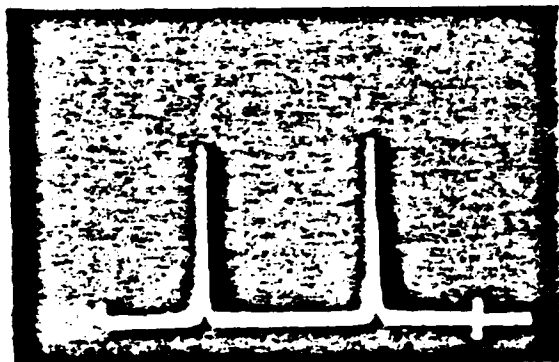
800 mW



1 W



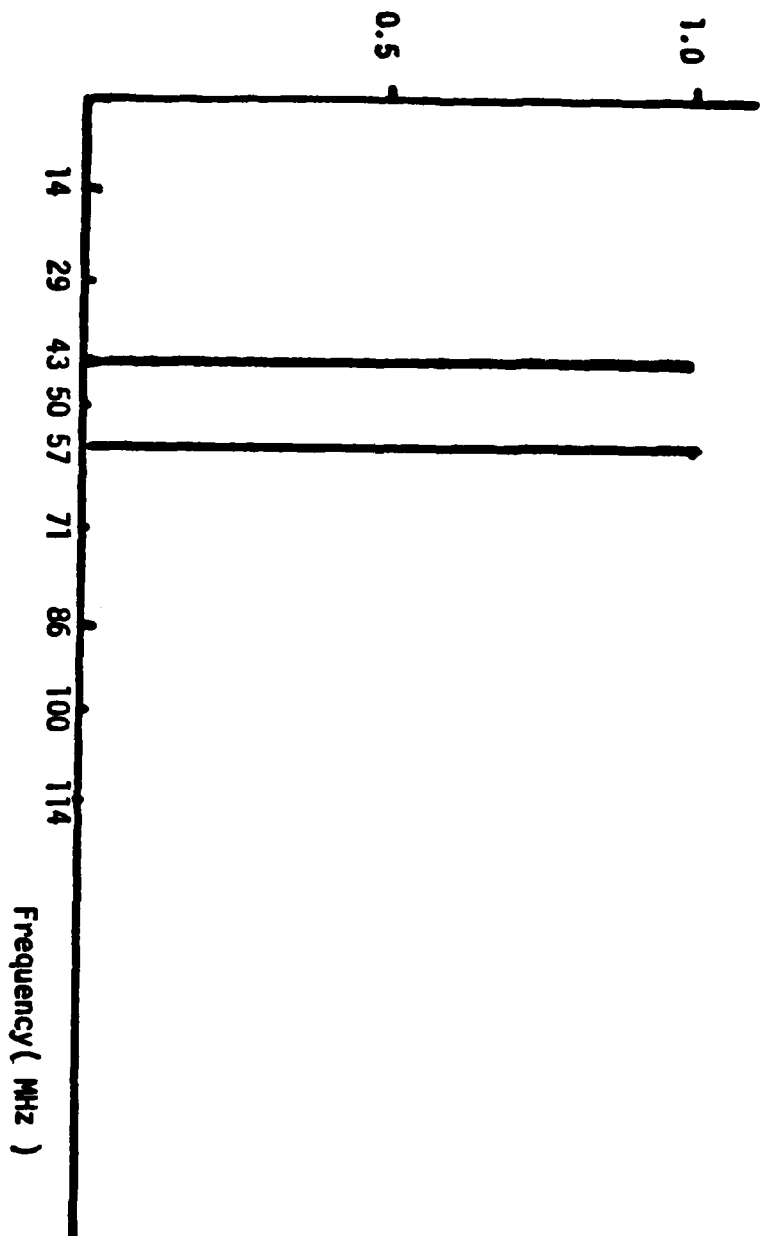
50 MHz and 7 MHz



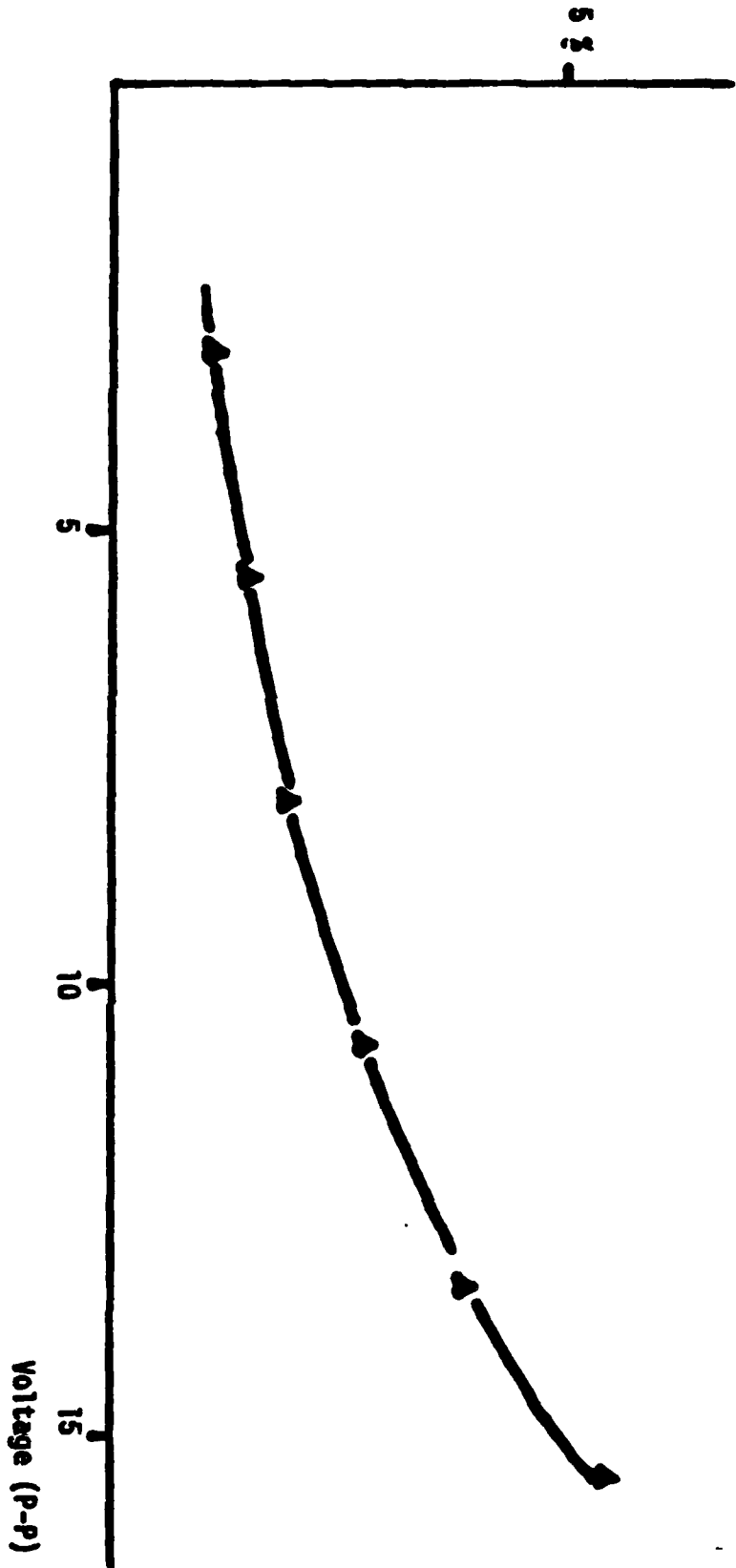
50 MHz and 10 MHz

Two-Tone Spectrum

-38-



Two-tone intermodulation (including  
power amplifier distortion)



#### IV. DYNAMIC RANGE ISSUES

In the previous chapter we concluded that the dominant factor limiting the performance of TSI architectures is the CCD detector. Essentially all 2-D optical processors require a 2-D detector at the output and CCD cameras have proven to be the best device for this purpose. The speed and space-bandwidth product of optical architectures that use 2-D spatial light modulations are typically limited by the input device. For instance, 2-D SLMS can be typically addressed at 30 frames/seconds. If a 2-D CCD is constructed with multiple read-out registers, allowing the data to be read-out at 300 frames/second, this speed can not be realized with a conventional architecture. A TSI architecture however can operate at this late rate because the AOD that is used as the input transducer can be fabricated with up to GHz bandwidth (corresponding to over a thousand frames per second). Therefore, the speed and the space-bandwidth of a TSI architecture are improved to the detector limit. The dynamic range of a 2-D space-integrating optical processor is determined by the dynamic range of the detector as well as the linearity of the input 2-D SLM. The relative importance between these two factors in determining the dynamic range of the overall processor depends on the application. In general, in applications where the signal-to-noise ratio at the input is small, the non-linearity of the input device becomes the dominant factor. The opposite is true for high SNR applications. In a TSI architecture the linear dynamic range of the AOD is so high ( $10^4$ - $10^5$ ), that the dynamic range of the processor is determined solely at the detector in almost all cases. The time integration that is performed on the detector in all TSI architectures, results in bias built-up which reduces the dynamic range available to the signal. The bias built-up arises in time integrating processors because of the need to represent bipolar functions by photogenerated charge, which is proportional to light intensity, a positive

quantity. We denote by DR and DR' the dynamic range of the CCD and the overall system, respectively. Then,

$$DR' = DR \left( \frac{SBR}{1+SBR} \right) .$$

where SBR is the ratio of the maximum value of the output signal to the bias. DR' is maximized as the CCD dynamic range DR, and SBR are made as large as possible. In the previous chapter we reported that in our present experiments  $DR \approx 10^3:1$  and we expect to be able to improve that by an order of magnitude by redesigning the CCD electronics. The maximum attainable value of the SBR is unity, in which case  $DR' = DR/2$ . If the SBR is very low however,  $DR' \approx (DR) (SBR)$ . For instance if  $SBR = 10^{-2}$ , then the dynamic range of the system will be a dismal 10:1, assuming  $DR = 10^3$ . It is therefore very crucial to design the system properly, so that SBR is maximized. The first consideration is whether to employ a coherent or an incoherent architecture. All the admissible 2-D processing operations can be implemented with both coherent or incoherent TSI architectures.

Incoherent systems are immune to coherent noise (speckle, undesirable interference effects) and therefore they can be constructed without the need of high quality optical components. The information however in an incoherent processor modulates the light intensity and bipolar numbers cannot be directly represented. A bias is added at the input stage of an incoherent system to allow bipolar signal representation throughout the processor. Let  $s(x,y)$  be a 2-D bipolar signal we wish to process and  $n(x,y)$  be an additive interference. The precise nature of  $n(x,y)$  depends on the application; it can be additive noise or a deterministic interference signal. Throughout the following analysis we will work with normalized (unitless) signals. This presents no problems since we are interested in the relative strengths between signals (SBR) and not their absolute values. For convenience we also take the maximum value of the signal to

always be unity and define the strength of all remaining terms relative to the signal. We define

$$K = \frac{\max \{s(x,y)\}}{\max \{n(x,y)\}} . \quad (7)$$

The input signal,  $f(x,y)$ , to the incoherent processor is given by

$$f(x,y) = \frac{1}{2} + \frac{k}{2(k+1)} \left[ s(x,y) + n(x,y) \right] , \quad (8)$$

and we have normalized both  $f(x,y)$  and  $s(x,y)$ . The TSI architecture performs a 2-D linear operation on  $f(x,y)$ , with a bipolar kernel  $h(x,\hat{x},y,\hat{y})$  (Eq. 1).

$$\begin{aligned} g(x,y) &= \iint f(x,y) \left[ \frac{1}{2} + \frac{1}{2} h(x,\hat{x},y,\hat{y}) \right] dx dy \\ &= \frac{1}{4} + \frac{k}{4(k+1)} \iint s(x,y) h(x,\hat{x},y,\hat{y}) dx dy \\ &\quad + \frac{k}{4(k+1)} \iint n(x,y) h(x,\hat{x},y,\hat{y}) dx dy. \end{aligned} \quad (9)$$

We have assumed in the above equation that the functions  $s$ ,  $n$  and  $h$  have zero mean and  $g$  is also normalized. The output  $g$ , consists of three additive terms. The first term is a constant bias. The second is the desired signal term which can attain a maximum value  $\frac{4}{4(k+1)}$ .

The third term is the interference filtering through to the output plane. In general, this term can vary with  $x$  and  $y$  and attain a maximum value  $\frac{k}{4(k+1)}$  ( $1/k$ ) =  $\frac{1}{4(k+1)}$ . In all the applications we are considering however, the interference is suppressed relative to the signal by the 2-D linear operation. We denote this processing gain by  $PG$ . The interference term then acts as additional bias with strength  $\frac{1}{4(k+1)PG}$ . The SBR in the incoherent case is equal to

$$SBR = \frac{k}{k+1 + \frac{1}{PG}} . \quad (10)$$



In most cases  $PG \gg 1$  and  $SBR = \frac{k}{k+1}$ . If  $k \gg 1$  (signal much stronger than the interference) then  $SBR = 1$ , which is the maximum value that can be attained. However if  $k \ll 1$ ,  $SBR = k$  and from Eq. 6,  $DR' = DR \cdot k$ . In many applications (e.g. SAR) this represents a disastrous loss in system dynamic range. Therefore incoherent TSI implementations are suitable only for cases where  $k \gg 1$ . In pattern recognition applications the input SNR is often sufficiently high to allow incoherent implementation. In most problems however the coherent implementation proves preferable. In coherent systems the amplitude of the light is modulated and that allows bipolar signals to be directly represented. The space integrating portion of the processing is performed without the need for a bias. The bias is introduced interferometrically at the detector stage, after the space integration has been performed. The processing gain that is realized in the space integrating portion of the system along with added flexibility in setting the bias level, result in a drastically reduced SBR as we will show presently. The input to the coherent processor is simply

$$f(x,y) = s(x,y) + n(x,y). \quad (11)$$

The output of the space integrating portion of the processor is

$$\begin{aligned} g'(\hat{x}, \hat{y}, y) &= \int s(x,y) h(x, \hat{x}, y, \hat{y}) dx \\ &+ \int n(x,y) h(x, \hat{x}, y, \hat{y}) dx \\ &= a(\hat{x}, \hat{y}, y) + b(\hat{x}, y, \hat{y}), \end{aligned} \quad (12)$$

where we denote by  $a$  and  $b$  the signal and interference terms at the output of the space integrating processor.  $g'$  is a function of three variables; in practice  $\hat{x}$  and  $\hat{y}$  are spatial variables and  $y$  is time. A bias,  $B$ , is inserted interferometrically at this stage so that bipolar signals can be represented by photogenerated charge

and the integration over  $y$  (time) is performed on the detector. The resulting signal on the detector, neglecting normalization constants, is given by

$$g(x,y) = \int |a(\hat{x},\hat{y},y) + b(\hat{x},\hat{y},y) + B|^2 dy$$

$$= 2B \int a dy + \int |a|^2 dy + \int |b|^2 dy + B^2 + 2B \int b dy + \int ab dy, \quad (13)$$

and we have performed the integration in  $y$  over a unit length. The first term in the above expansion is the desired signal form. The remaining terms are all bias terms. Their value depends on both the signal and the interference and it can be precisely determined only if these functions are known (i.e. for each application). However a simple, but general analysis can be carried out that is applicable in all the problems we have considered thus far. For instance it applies directly to SAR and 2-D Fourier transforms and with minor modifications it also applies to image correlation. For convenience, we normalize the peak value of the signal term to unity:  $\max \{ \int a dy \} = 1$ . The fourth term is a constant bias term. The fifth term is the interference filtered in both dimensions and therefore it is suppressed by the full processing gain of the systems. The value of this term is taken to be equal to  $1/(k \cdot PG)$ . The last term can be neglected when the input and interference are uncorrelated (true in all the problems we have examined). The second term is the integral  $\int |a|^2 dy$  and its value relative to the unit defined above ( $\max \{ \int a dy \} = 1$ ) will depend on the function  $f(x,y)$ . In all cases of interest (correlation, SAR, spectrum analysis) this term is restricted to less than unity. The third term is given by

$$\begin{aligned} \int |b|^2 dy &= \int |n(x,y) h(x,x,y,y) dx|^2 dy \\ &= \frac{1}{k^2 (PG_x)^2} \int |b^-(x,y,y)|^2 dy \end{aligned} \quad (14)$$

where  $PG_x$  is the processing gain resulting from the integration along  $x$  alone

( $PG = (PG_x) (PG_y)$ ) and  $B^2 \leq 1$ . The integral  $\int |b^-|^2 dy$  is never as small

as  $1/(PG_y)^2$  (i.e. the incoherent integration in  $y$  does not suppress the interference as effectively as coherent integration) but in general it is considerably less than unity. We denote

$$\frac{1}{PG_y} = \int |b^-(\hat{x}, \hat{y}, y)|^2 dy. \quad (15)$$

The approximate expression for the SBR of the coherent processor can now be written:

$$SBR = \frac{2B}{B^2 + 1 + 1/(k^2 \cdot PG_x^2 \cdot PG_y) + 2B/(K \cdot PG)} \quad (16)$$

We wish to maximize this ratio by setting appropriately the level of the reference  $B$ .

$$\frac{\partial (SBR)}{\partial B} = 0 \rightarrow B = \sqrt{1 + 1/(k^2 \cdot PG_x^2 \cdot PG_y)}. \quad (17)$$

Substituting this value in Eq. 16 we find the value for the optimum SBR:

$$SBR_{opt} = \frac{1}{\sqrt{1 + 1/(k^2 \cdot PG_x^2 \cdot PG_y)} + 1/(K \cdot PG)} \quad (18)$$

Typically,  $K \cdot PG$  is sufficiently larger than unity, and the second term in the denominator of the above equation can be neglected. When the coherent ( $PG_x^2$ ) and incoherent ( $PG_y$ ) processing gains are sufficient to suppress the interference below the signal level ( $k^2 PG_x^2 PG_y > 1$ ), then  $SBR_{opt} \approx 1$  and  $DR = DR/2$ . If  $k^2 PG_x^2 PG_y \ll 1$ , then

$$SBR_{opt} \approx k \cdot PG_x \cdot \sqrt{PG_y}.$$

By comparison, in the incoherent case  $SBR \approx k$  for small  $k$ . We see that if coherent light is used the signal-to-bias ratio can be increased by  $PG_x \cdot \sqrt{PG_y}$ . The

significance of this result cannot be overstated. We will consider SAR as an example to demonstrate this point. In SAR the interference consists of the radar returns from targets surrounding a point target that is being imaged. In this case  $k$  can be easily as small as  $10^{-4}$ . Therefore we would have practically no system dynamic range with an incoherent implementation.  $PG_x$  is typically  $10^2$ . In SAR  $PG_y \approx 10^2$ . Therefore,  $\sqrt{PG_y} = 10$  and  $SBR_{opt} = (10^{-4} (10^2) (10)) = 10^{-1}$ . The resultant system dynamic range is  $DR' = DR (SBR / (1+SBR)) \approx DR/10$ . If the CCD has a dynamic range equal to  $10^4:1$ , then SAR images can be formed with a comfortable  $10^3:1$  (60dB) dynamic range.

## V. APPLICATIONS

In Chapter II we established the methodology for constructing 2-D optical processors using the TSI method and determined the operations that are achievable. Within this general context there is very large number of different TSI architectures. We can arrive at specific designs only after a particular problem has been posed. We have thus far examined four applications: image correlation, synthetic aperture radar, the calculation of moments and 2-D spectrum analysis. Our work in these areas will not only provide what we feel are excellent solutions to important and computationally difficult problems, but also brings out the trade-offs and procedures that are involved in designing 2-D TSI architectures. This has proven to be an extremely important factor in determining the direction of the entire investigation.

Image correlation is the most powerful operation that can be implemented with a TSI architecture. It is also the operation with the widest applicability in image processing. Several image correlator architectures have been designed and the first real-time full 2-D correlation with a TSI architecture, was observed recently in our laboratory. The architecture and our experimental results are described in detail in the two published papers attached as appendices Va and Vb at the end of this chapter.

Synthetic Aperture Radar is the first problem to which optical computers were successfully applied and it appears to be ideally suited for TSI implementation. The theory of operation of this processor and initial experimental results are presented in appendices Vc and Vd.

2-D Fourier transforms are useful for the calculation of image spectra as well as the folded spectrum of long 1-D signals. TSI architectures can prove to be advantageous over the conventional 2-D Fourier transforming lens in certain

applications despite the simplicity and elegance of the conventional approach. The advantages of the TSI architecture in this application is the superior input device (AOD vs. 2-D SLM) resulting in higher bandwidth and potentially dynamic range, as well as flexibility in selecting the bandwidth and resolution with external electronic signals. TSI architectures for 2-D Fourier transforms are discussed in appendix Ve.

Moments have been shown to be useful quantities for image recognition, analysis and normalization. Several TSI architectures for the calculation of the moments of an image are presented in appendix Vf.

## Appendix Va

# Optical image correlation using acoustooptic and charge-coupled devices

Demetri Psaltis

An optical processing method is presented which allows the correlation of two images to be computed in real time with a 1-D acoustooptic spatial light modulator as the input device. Two-dimensional processing is accomplished by a combination of spatial and temporal integration. The time-integrating processing is performed by a CCD detector that is operated as an optically addressed correlator.

## I. Introduction

Optical image processors normally require at the input stage a real-time 2-D spatial light modulator (SLM)<sup>1</sup> which creates a suitable transparency corresponding to the input image. The relatively immature state of development of 2-D SLMs is a major factor that has prevented the realization of the huge potential of optical image processors. The limitations presently imposed by the SLMs can be overcome either by further developments in device technology or alternatively by modifying the optical system architecture. Several architectural designs have been proposed for this purpose.<sup>2-4</sup> For example, if the optical processor can be implemented with noncoherent illumination the requirements on the optical quality of the SLM can be relaxed, and a self-luminous display (such as a CRT) could be used as the input SLM. In a recent publication by the author<sup>3</sup> a 2-D signal processing technique has been presented that does not require the use of real-time 2-D SLMs. This is accomplished by entering the 2-D input data into the optical processor one line at a time using a 1-D acoustooptic SLM.<sup>5</sup> Each line is filtered spatially by the optical system. The data are processed in the second dimension by integrating the response due to consecutive lines on a time-integrating detector array. Acoustooptic technology is highly developed and consequently high quality acoustooptic SLMs can be fabricated. The use of acoustooptic devices (AOD) rather than 2-D SLMs in the optical processor can lead to improvements in accuracy, speed, and practicality (size, weight, power requirements, cost). In

this paper we describe the application of the time-and-space integrating processing technique to the implementation of an image correlator. Image correlation is a useful signal processing operation in pattern recognition, image restoration and enhancement, and video compression and is also the most powerful operation that can be implemented by an optical computer. Therefore, image correlation is probably the most significant 2-D signal processing operation that can be implemented with the time-and-space integrating method. In the following section we describe the operation of the optical image correlator, and in Sec. III we discuss the unique characteristics of this architecture.

## II. Description of the Processor

The time-and-space image correlating architecture is shown in Fig. 1. We will demonstrate that this system computes the cross-correlation  $g(\hat{x}, \hat{y})$  of two complex functions  $f(x, y)$  and  $h(x, y)$ :

$$g(\hat{x}, \hat{y}) = \iint f(x, y) h^*(x + \hat{x}, y + \hat{y}) dx dy. \quad (1)$$

The operation of the correlator in Fig. 1 can be summarized as follows: the optical system is a multichannel 1-D correlator which consecutively correlates each row of the function  $f(x, y)$  with all rows of the function  $h(x, y)$ . The AOD is used to enter the rows of  $f(x, y)$  sequentially into the optical system. The 1-D correlations are summed appropriately by operating the CCD detector in the shift-and-add mode.<sup>6</sup> The key components of the system are the AOD and the CCD detectors.

The AOD consists of a piezoelectric transducer bonded onto an acoustooptic crystal. We denote the voltage applied to the piezoelectric transducer by  $s(t)$ . The signal  $s(t)$  has the form  $s(t) = \alpha(t) \cos[\omega_0 t + \phi(t)]$ , where the complex envelope  $a(t) = \alpha(t) \exp[j\phi(t)]$  is the modulating signal and  $\omega_0/2\pi$  is the center frequency of the AOD. The device is illuminated by a collimated light beam incident at the Bragg angle  $\theta_B$ , where<sup>7</sup>

The author is with California Institute of Technology, Department of Electrical Engineering, Pasadena, California 91125.

Received 7 August 1981.

0003-6935/82/030491-06\$01.00/0.

© 1982 Optical Society of America.

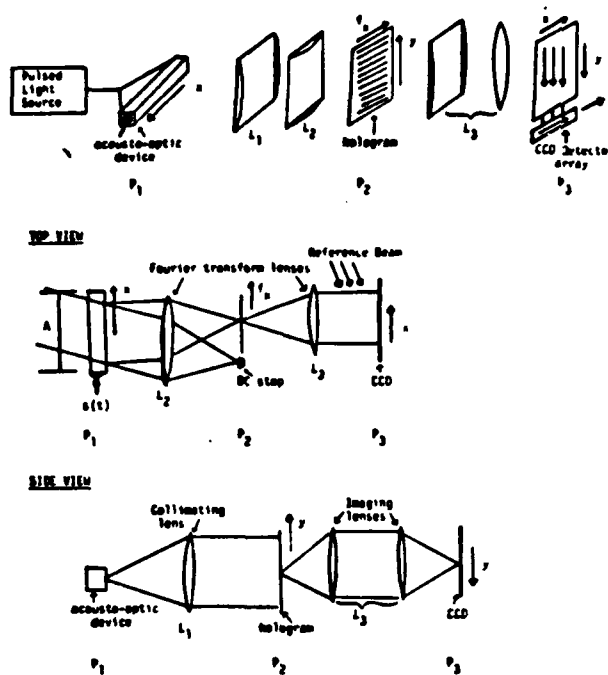


Fig. 1. Image correlator architecture.

$$\sin \theta_B = \frac{\lambda \omega_0}{4\pi v} \quad (2)$$

$\lambda$  is the wavelength of light in the acoustooptic crystal, and  $v$  is the speed of sound in the crystal. The acoustic wave that is induced by the voltage  $s(t)$  causes a portion of the incident light to be diffracted. In the Bragg regime essentially all the diffracted energy is concentrated in the first order. For relatively weak modulation levels the amplitude of the diffracted light  $E(x', t)$  is given by<sup>8</sup>

$$\begin{aligned} E(x', t) &\approx c_1 \text{rect} \left( \frac{x' - A/2}{A} \right) \alpha \left( t - \frac{x'}{v} \right) \\ &\times \exp \left[ j\phi \left( t - \frac{x'}{v} \right) \right] \exp \left[ j\omega_0 \left( t - \frac{x'}{v} \right) \right] \exp \left[ j \frac{2\pi \sin \theta_B x'}{\lambda} \right] \\ &= c_1 \text{rect} \left( \frac{x' - A/2}{A} \right) \alpha \left( t - \frac{x'}{v} \right) \\ &\times \exp(j\omega_0 t) \exp \left( -j \frac{2\pi \sin \theta_B x'}{\lambda} \right). \end{aligned} \quad (3)$$

In Eq. (3)  $c_1$  is a constant,  $x'$  is along the direction of the acoustic wave propagation, and  $A$  is the aperture of the AOD. Thus, the amplitude of the diffracted light is modulated by the complex signal  $\alpha(t - x'/v)$  over the spatial window  $A$ , Doppler shifted by the traveling acoustic wave by  $\omega_0/2\pi$ , and deflected around the Bragg angle  $\theta_B$ . For the rest of our discussion we will not carry the deflection term  $\exp[-j(2\pi \sin \theta_B x')/\lambda]$  in the equations since it does not affect the operation of the system we will describe. In Eq. (3) the origin of the  $x'$  coordinate is assumed to be at the piezoelectric transducer, and  $x'$  increases away from the transducer. In

our analysis it is more convenient to use the coordinate transformation  $x = -x' + A$ . In the  $x$ -coordinate system the origin is at the far end of the acoustooptic crystal, and  $x$  increases toward the transducer. Equation (3) can be rewritten as follows:

$$E(x, t) = c_1 \text{rect} \left( \frac{x - A/2}{A} \right) \alpha \left( t + \frac{x}{v} - \frac{A}{v} \right) \exp(j\omega_0 t). \quad (4)$$

We shall use Eq. (4) in the rest of our discussion.

The CCD image sensor consists of a matrix of photosensitive sites where incident photons are converted to electronic carriers which are trapped locally in the depletion region of a MOS junction.<sup>9</sup> The photogenerated charge packets can be transferred to adjacent pixels along one of the dimensions of the array by applying a clock waveform to the device. When the device is used as an image sensor, each charge packet is shifted continuously along the array after a single exposure to light until it reaches the edge of the device where an output CCD stage transfers the signal to the output pin. In our system the CCD array is exposed periodically. After each exposure the charge that is accumulated in each site is shifted by only 1 pixel. The photogenerated charge due to the most recent exposure is simply added to the charge that is already stored in each pixel. In Fig. 1 the spatial dimension along the shifting direction of the CCD is denoted by  $\hat{y}$ . Let the intensity of the illuminating light at the location  $\hat{y}$  during the  $n$ th exposure be denoted by  $I(n, \hat{y})$ . The charge generated at the pixel located at  $\hat{y}$  during the  $n$ th exposure is proportional to  $I(n, \hat{y})$ . After  $N$  exposures ( $N \geq n$ ), the charge  $I(n, \hat{y})$  shifts  $N - n$  pixels or by a distance  $(N - n)\Delta y$  in the  $\hat{y}$  direction.  $\Delta y$  is the pixel separation. The charge that is accumulated in the CCD as a function of pixel position  $\hat{y}$  after  $N$  exposures is given by

$$Q(\hat{y}) = \sum_{n=1}^N I(n, \hat{y} + (n - N)\Delta y), \quad (5)$$

for  $\hat{y} = 0$  to  $\hat{y} = M\Delta y$ , where  $M$  is the number of pixels in the CCD and  $I(n, \hat{y}) = 0$  for all  $\hat{y} \leq 0$ . The maximum number of exposures  $N$  for which the addition in Eq. (3) can be performed is equal to  $M$ . Bromley, and Monahan *et al.*<sup>6</sup> have used a CCD detector array in this mode of operation to perform a variety of 1-D linear operations. In our system we use the CCD detector to construct an array of parallel 1-D correlators.

In most image recognition applications the input scene and the filter functions are real. For this reason and to present the principles of operation of the system more clearly, we will restrict our analysis initially to real functions  $f$  and  $h$ . For completeness we will describe the operation of the system with complex signals  $f$  and  $h$  at the end of this section. The 1-D Fourier transform of a transparency with amplitude transmittance  $h(x, y)$  is formed with an astigmatic lens system which transforms in the  $x$  direction and images along  $y$ .<sup>10</sup> A hologram of the resulting light amplitude distribution is formed by recording its interference with a plane wave reference on photographic film or any other suitable device. The amplitude transmittance of the developed hologram is proportional to<sup>10</sup>



$$\begin{aligned}
 & |B \exp(-j2\pi \sin\theta_H F f_x) + H(f_x, y)|^2 \\
 &= B^2 + |H(f_x, y)|^2 \\
 &\quad + BH^*(f_x, y) \exp(-j2\pi \sin\theta_H F f_x) \\
 &\quad + BH(f_x, y) \exp(+j2\pi \sin\theta_H F f_x), \quad (6)
 \end{aligned}$$

where

$$H(f_x, y) = \int h(x, y) \exp(-j2\pi f_x x) dx.$$

$\theta_H$  is the angle of incidence on the hologram of the reference beam,  $B$  is its amplitude,  $F$  is the focal length of the lens in the  $x$  direction, and  $f_x$  is the spatial frequency variable which is linearly related to the spatial variable  $\xi$  in the plane of the hologram ( $f_x = \xi/(\lambda F)$ ). In Eq. (6) only the term containing  $H^*$  contributes to the correlation, and the remaining terms are blocked out in the optical system. Thus the effective complex transmittance of the hologram can be written

$$t_H(f_x, y) = BH^*(f_x, y) \exp(-j2\pi \sin\theta_H F f_x). \quad (7)$$

This hologram is placed in plane  $P_2$  of Fig. 1.

The image  $f(x, y)$  is scanned in a raster format to produce a temporal electronic signal  $r(t)$ . The raster signal  $r(t)$  is related to the 2-D function  $f(x, y)$  by the following equation:

$$r(t) = f[t - (n-1)T]v_s, n\Delta y \quad (8)$$

for  $n = 1$  to  $N$ , where  $v_s$  is the scanning velocity of the device (such as a TV camera) that produces the raster signal,  $T$  is the duration of each raster line [ $v_s T$  is the size of  $f(x, y)$  in the  $x$  direction], and  $\Delta y$  is the resolution of  $f(x, y)$  in the  $y$  direction [ $N\Delta y$  is the size of  $f(x, y)$  in the  $y$  direction]. In Eq. (8) we assume that  $f(x, y) = 0$  for  $x > v_s T$  and  $x < 0$ .  $r(t)$  is heterodyned to the center frequency  $\omega_0$  and applied to the AOD in plane  $P_1$  of Fig. 1. The modulation  $t_A(x, t)$  introduced by the AOD on the amplitude of the diffracted light can be found by substituting  $a(t)$  by  $r(t)$  in Eq. (4):

$$\begin{aligned}
 t_A(x, t) &= c_1 \text{rect}\left(\frac{x - A/2}{A}\right) r\left[t + \frac{x}{v} - \frac{A}{v}\right] \exp(j\omega_0 t) \\
 &= c_1 \text{rect}\left(\frac{x - A/2}{A}\right) f\left[\left(t + \frac{x}{v} - \frac{A}{v} - nT + T\right)v_s, n\Delta y\right] \\
 &\quad \times \exp(j\omega_0 t) \quad (9)
 \end{aligned}$$

We set  $A = v_s T$ , i.e., the aperture of the AOD can accommodate exactly one raster line of  $f(x, y)$ . For convenience we also set  $v_s = v$ . At time instances  $t = nT$  the modulation of the AOD is given by

$$\begin{aligned}
 t_A(x, nT) &= c_1 \text{rect}\left(\frac{x - A/2}{vT}\right) f\left[\left(nT + \frac{x}{v} - \frac{A}{v} - nT + T\right)v_s, n\Delta y\right] \\
 &\quad \times \exp(j\omega_0 nT) \\
 &= c_1 f(x, n\Delta y) \exp(j\omega_0 nT). \quad (10)
 \end{aligned}$$

The rect function can be dropped in Eq. (10) since  $f(x, y)$  was defined to be nonzero for  $0 < x < vT$ . Thus at times  $t = nT$ , a single line of the function  $f(x, y)$  modulates spatially the light diffracted by the AOD. A pulsed light source is used in the system to illuminate the AOD only at the instances  $t = nT$ . The temporal modulation of the source can be written as

$$t_S(t) = \text{rect}\left(\frac{t - nT}{\tau}\right) \quad (11)$$

for  $n = 1$  to  $N$ , where  $\tau$  is the duration of each light pulse, and the pulse shape has been approximated by a rectangular function. The light diffracted by the AOD is modulated by the product of Eq. (9) and (11). We denote this modulation function by  $t_{SA}(x, t)$ . For  $1/\tau$  larger than the bandwidth of  $r(t)$ ,  $t_{SA}$  can be approximated by

$$\begin{aligned}
 t_{SA}(x, t) &= t_S(t)t_A(x, t) \\
 &= \exp(j\omega_0 t) \text{rect}\left(\frac{t - nT}{\tau}\right) f\left[\left(t + \frac{x}{v} - nT\right)v_s, n\Delta y\right] \\
 &= f(x, n\Delta y) \exp(j\omega_0 t) \text{rect}\left(\frac{t - nT}{\tau}\right). \quad (12)
 \end{aligned}$$

Lens  $L_1$  in Fig. 1 is used to collimate this light distribution in the vertical direction so it illuminates the hologram in plane  $P_2$  uniformly in the  $y$  direction. Lens  $L_2$  takes the Fourier transform in the  $x$  direction. The amplitude of the light entering plane  $P_2$  is modulated by

$$\begin{aligned}
 t_{SA}(f_x, t, n) &= \int t_{SA}(x, t) \exp(-j2\pi f_x x) dx \\
 &= F(f_x, n\Delta y) \exp(j\omega_0 t) \text{rect}\left(\frac{t - nT}{\tau}\right), \quad (13)
 \end{aligned}$$

where

$$F(f_x, n\Delta y) = \int f(x, n\Delta y) \exp(-j2\pi f_x x) dx.$$

The light immediately after plane  $P_2$  is modulated by the product of Eqs. (7) and (13). The astigmatic lens system  $L_3$  images plane  $P_2$  onto the output plane  $P_3$  in the  $y$  direction, while it performs the Fourier transform in the horizontal ( $x$ ) direction. The amplitude of the light at plane  $P_3$  is given by

$$\begin{aligned}
 t_D(x, y, t, n) &= \int t_{SA}(f_x, t, n) t_H(f_x, y) \exp(-j2\pi f_x x' df_x) \\
 &= c_2 \exp(j\omega_0 t) \text{rect}(t - nT) \int F(f_x, n\Delta y) H^*(f_x, y) \\
 &\quad \times \exp[-j2\pi(\sin\theta_H F + x')f_x df_x] \\
 &= c_2 \exp(j\omega_0 t) \text{rect}\left(\frac{t - nT}{\tau}\right) \\
 &\quad \times \int f(x, n\Delta y) h(x + x', y) dx, \quad (14)
 \end{aligned}$$

where  $x' = x + \sin\theta_H F$  and  $y$  are the horizontal and vertical spatial coordinates, respectively, in  $P_3$ , and  $c_2$  is a constant. The convolution theorem was used to obtain the last form of Eq. (14). The output light distribution is detected interferometrically by the CCD detector array at the output plane to obtain a detected signal proportional to Eq. (14). A reference beam derived from the same source is heterodyned to the center frequency  $\omega_0$  of the AOD and made incident on the detector at an angle  $\theta_D$ . The amplitude of the reference beam is described by

$$t_R(x, t) = A \exp(j2\pi \sin\theta_D x/\lambda) \exp(j\omega_0 t) \text{rect}\left(\frac{t - nT}{\tau}\right). \quad (15)$$

The signal  $I(x, y, n)$  that is detected by the CCD is proportional to the time integrated intensity of the sum of Eqs. (14) and (15)

$$\begin{aligned}
I(x, y, n) &= c_3 |f(t_D + t_R)|^2 dt \\
&= \int_{nT - \tau/2}^{nT + \tau/2} |A \exp(j2\pi/\phi x) \\
&\quad + f(x, n\Delta y)h(x + x, y)dx|^2 dt \\
&= \tau c_3 A^2 + |f(x, n\Delta y)h(x + x, y)dx|^2 \\
&\quad + 2A |f(x, n\Delta y)h(x + x, y)dx| \cos(2\pi/\phi x), \quad (16)
\end{aligned}$$

where  $f_0 = \sin\theta_D/\lambda$ . The third term in this equation is the 1-D correlation of the  $n$ th row of  $f(x, y)$  with all the rows of  $h(x, y)$ . The correlation forms on the spatial carrier  $f_0$ . Since both  $f$  and  $h$  are real functions only the amplitude of the fringe pattern is modulated. In the  $y$  direction the CCD is operated in the shift-and-add mode described earlier. The charge that is accumulated in the CCD after  $N$  light pulses can be found by substituting Eq. (16) into Eq. (5):

$$\begin{aligned}
Q(x, y) &= \sum_{n=1}^N I(x, y, n) \\
&= c_4 \left\{ NA^2 + \sum_{n=1}^N |f(x, n\Delta y)h(x + x, y + (n - N)\Delta y)dx|^2 \right. \\
&\quad \left. + 2A \left[ \sum_{n=1}^N f(x, n\Delta y)h(x + x, y + n\Delta y - N\Delta y)dx \right] \cos(2\pi/\phi x) \right\}. \quad (17)
\end{aligned}$$

The third term in Eq. (17) forms on a spatial carrier of frequency  $f_0$ . By setting  $f_0$  equal to or larger than the bandwidth of  $f(x, y)$ , this term can be separated from the other two baseband terms by electronic filtering after the signal from the CCD is converted to a video signal. The envelope of the carrier in Eq. (17) is recognized to be the 2-D correlation described by Eq. (1) with the integration over the continuous variable  $y$  replaced by the summation over the discrete variable  $n\Delta y$ . The correlation pattern is shifted by the constant  $N\Delta y$  in the  $y$  direction. For a CCD detector with  $N$  horizontal rows, this means that each slice of the correlation pattern is formed sequentially at the last row of the device. The fast horizontal CCD shift register transfers each line of the 2-D correlation to the output stage of the device where it can be displayed or processed further electronically.

We shall close this section by discussing how the system of Fig. 1 can be used to correlate complex 2-D functions. We assume that we have the complex function  $h(x, y)$  recorded either holographically or in a digital memory. The 1-D Fourier transform of this complex function can then be produced and placed in plane  $P_2$  of Fig. 1 either optically or by computer generation. The function  $f(x, y)$  is represented by two real functions that correspond to its real and imaginary parts. The two corresponding electronic raster signals are used to modulate in quadrature the carrier that is applied to the AOD. From Eq. (4) we conclude that the modulation introduced by the AOD is proportional to the complex signal that is used to modulate in quadrature the carrier. The optical system performs the complex correlation in the  $x$  direction. The phase of the 1-D complex correlation is preserved in the phase of the fringe pattern in Eq. (16). Thus the full 2-D

-52- complex correlation is formed by performing the addition over  $n$  in Eq. (17).

### III. Discussion

We devote this section to the discussion of the characteristics of the AOD/CCD image correlator. The majority of the potential advantages of this system are consequences of the use of an AOD as the real-time SLM. AODs have been investigated and manufactured for many years. Consequently reliable and relatively inexpensive high quality devices are now commercially available. The simple structure of an AOD relative to most 2-D SLMs allows compact systems to be built with relatively low power requirements and without the need for high voltages. Thus the use of AODs can lead to practically feasible optical image processors in the immediate future. The excellent modulation characteristics of AODs<sup>11</sup> (high linear dynamic range, spatial uniformity, and low scatter level) allow the input image to be represented in the optical computer with high fidelity, with a corresponding improvement in overall accuracy. AODs can accept data at rates up to several gigahertz. We do not anticipate however, that this capability can be approached by the AOD/CCD image processor in the near future because of limitations in the speed with which the CCD can be read out. The system also requires a device which produces an electronic raster signal corresponding to the input image. In most applications this device can be a TV camera. The current limitations of CCD and image sensor technologies impose a limit of  $\approx 50$ -MHz input rate which corresponds to the processing of 200 images, each consisting of  $500^2$  pixels in 1 sec. The need for an auxiliary image sensor may be construed as a disadvantage of this technique. Ideally it is preferable to have a device which serves simultaneously as the image sensor and the SLM for the optical computer. In many applications, however, 2-D SLMs are not suitable for direct detection of the live scene, and an auxiliary sensor must be used. The output of the auxiliary sensor is then scanned onto the 2-D SLM either electronically or optically. In such cases, the ability of the AOD/CCD system to accept directly the electronic raster signals is an advantage.

The limitations on the performance of the AOD/CCD processor are imposed primarily by the CCD detector. These limitations are not significantly different from the limitations imposed by the detector on any optical image processor. For continuous processing of frames the input data rate cannot exceed the readout rate in the AOD/CCD processor. The speed at which commercially available CCD detector arrays are normally read out is 5-10 MHz (standard video frame rates). Therefore, the processing speed is limited by the detector if one is restricted to using commercially available devices. CCD detectors which are fabricated specifically for optical signal processing applications can be made with several parallel output stages,<sup>12</sup> which increases the readout speed. For example, a device with 10 parallel readout stages could be read out at 50-100-MHz rates. In addition, current research in GaAs<sup>13</sup> CCDs shows promise of extending the inherent speed

of these devices to hundreds of megacycles per second. CCD detectors have  $\sim 500 \times 500$  pixels,<sup>14</sup> and devices with over one thousand pixels in each dimension are presently under development. The number of pixels of the CCD in the nonshifting dimension determines in this dimension the space-bandwidth product of the images that can be processed. The number of pixels in the shifting direction determines the space-bandwidth product of the filter in the shifting dimension but does not limit the size of the input scene. In other words, this processor is a sliding window correlator in one dimension. This feature can be useful in applications where the input image is sensed by a linear detector array, and the imaging in the second dimension is accomplished by the relative motion between the detector and the object. The dynamic range, noise, linearity, and spatial nonuniformity of the CCD detector are factors that affect the accuracy with which the processed image can be detected. Commercial CCD cameras have dynamic range in excess of 1000:1 with excellent linearity in this range.<sup>14</sup> This range can be extended by designing CCDs with large detector elements that can store a larger photogenerated charge and also by cooling the device and using postdetection electronic processing to minimize detector noise. The detector noise is caused by shot noise of the signal and leakage current, feed-through of clock transients, and thermal noise in the amplifiers.<sup>14</sup> The trade-off between output noise and bandwidth is the major engineering challenge in the design of the AOD/CCD image processor. The portion of the detector dynamic range that is utilized to represent the output signal is proportional to the ratio of the signal to the bias terms in Eq. (17):

$$SBR = \frac{2A \sum_{n=1}^N \int f(x, n\Delta y) h(x + x_0 + n\Delta y + y) dx}{NA^2 + \sum_{n=1}^N |\int f(x, n\Delta y) h[x + x_0 + (n - N)\Delta y] dx|^2} \quad (18)$$

For  $SBR = 1$ , half of the dynamic range is utilized. The  $SBR$  however can be significantly lower depending on the functions  $f$  and  $h$ . It is thus crucial to maximize the dynamic range of the CCD.

We are considering two types of pulsed source for this system: mode-locked gas lasers<sup>7</sup> and semiconductor lasers.<sup>7</sup> Gas lasers can satisfy all the requirements of the system (pulse width, peak power, coherence, sta-

bility), but semiconductor lasers are attractive because they are compact, efficient, and relatively inexpensive. The modes in a semiconductor laser, however, are so widely spaced because of the short cavity length that interferometric detection is feasible only with a single-mode laser. Single-mode laser diodes can be fabricated and are even available commercially. However when these diodes are pulsed several modes exhibit gain during the transients. For a well-fabricated diode the transients decay within 1 nsec.<sup>15</sup> Thus, if a pulse with duration of 5 nsec is used, single-mode operation can be obtained 80% of the time.

The operation of the CCD detector in the shift-and-add mode has an important advantageous consequence. Since the signal that eventually reaches the output stage of the detector is a weighted sum of the signal detected by all the detector elements in a single column of the CCD array, the variations in the responsivity among the individual pixels and dark current will average out.<sup>14</sup> In addition, speckle noise which is uncorrelated from pixel to pixel will also average out. Thus the system utilizes coherent light which provides the flexibility of easily synthesizing a filter in the spatial frequency domain but is immune to coherent noise.

## References

1. D. Casasent, *Proc. IEEE* **65**, 143 (1977).
2. W. T. Rhodes, *Proc. Soc. Photo-Opt. Instrum. Eng.* **180**, 143 (1979).
3. D. Psaltis, *J. Opt. Soc. Am.* **71**, 198 (1981).
4. M. O. Hagler, R. J. Marks II, E. L. Kral, J. F. Walkup, and T. F. Krile, *Appl. Opt.* **19**, 4253 (1980).
5. J. C. Chang, *IEEE Trans. Sonics Ultrason.* **SU-23**, 2 (1976).
6. K. Bromley, M. Monahan *et al.*, *Proc. Soc. Photo-Opt. Instrum. Eng.* **118**, 118 (1977).
7. A. Yariv, *Quantum Electronics* (Wiley, New York, 1967).
8. W. T. Rhodes, *Proc. IEEE* **69**, 65 (1981).
9. D. F. Barbe, *Proc. IEEE* **63**, 38 (1975).
10. J. W. Goodman, *Introduction to Fourier Optics* (McGraw-Hill, New York, 1968).
11. K. Preston, *Coherent Optical Computers* (McGraw-Hill, New York, 1972), p. 163.
12. G. M. Barsbuk, *Proc. IEEE* **69**, 100 (1981).
13. R. C. Eden and I. Deyhimy, *Proc. Soc. Photo-Opt. Instrum. Eng.* **214**, 39 (1979).
14. J. A. Hall, in *Applied Optics and Optical Engineering*, Vol. 8, R. R. Shannon and J. C. Wyant, Eds. (Academic, New York, 1980).
15. K. Lau, "Ultra-high Frequency Dynamics of Semiconductor Injection Lasers," Ph.D. Thesis, California Institute of Technology, Pasadena, 1981.

## Appendix Vb

### ACOUSTO-OPTIC/CCD IMAGE PROCESSOR

Demetri Psaltis, Eung Gi Paek and Santosh Venkatesh

California Institute of Technology  
Department of Electrical Engineering  
Pasadena, CA, 91125

#### ABSTRACT

Optical image correlators are presented that use acousto-optic and charge-coupled devices as the input and output transducers respectively. Experimental results are presented and the applicability to pattern recognition of a non-linear pseudo-correlation that can also be conveniently computed with these processors, is discussed.

#### INTRODUCTION

Image processing is perhaps the most natural application of optical information processing because the two dimensions of the optical system and its parallel processing capability are very effectively utilized in this application. The potential of optical image processors however, can only be realized in practice if suitable transducers are available to bring the images into the optical processor with sufficient speed and accuracy and also transducers (detectors) to read-out the processed images. In recent years the development of Acousto-Optic Devices (AOD) and semiconductor detector arrays and light sources, has led to the development of high performance optical processors [1,2]. In this paper we discuss how acousto-optic devices and CCD detectors can be used for optical image correlation. The acousto-optic device is used as the input transducer in the optical processor and it receives the image to be processed in the form of a video electronic signal. The CCD is used as the optical detector in the system and simultaneously as an array of electro-optic correlators. The advantages that can be derived from the use of these relatively mature technologies in the implementation of an optical 2-D correlator are high speed, flexibility, accuracy, small physical size and power efficiency.

In the following section we discuss the general method for performing image correlation with an acousto-optic processor. In section III

we review the holographic implementation of such a processor and the experimental results of this implementations are included in section IV.

#### GENERAL CONCEPT

The correlation  $g(\xi, \eta)$  of an input image  $f(x, y)$  and a reference image  $h(x, y)$  is given by:

$$g(\xi, \eta) = \iint f(x, y) h(x+\xi, y+\eta) dx dy. \quad (1)$$

We are concerned here with the implementation of this operation with an optical system in which the input image  $f(x, y)$  is introduced through an AOD. AOD's are 1-D spatial light modulators with a linear space bandwidth product typically equal to  $10^3$  pixels. The size of the images that we like to be able to process optically is at least  $10^3 \times 10^3$  pixels. Therefore, it is clear that an AOD cannot be used to simultaneously modulate a light beam with an entire image. Typically, a single line of the image can be accommodated by the AOD at one time. This fact dictates our processing strategy: the input image is entered into the optical processor and processed one line at a time. The processed image lines are detected and accumulated on a 2-D CCD camera [2]. The image  $f(x, y)$  must be sampled in one of its dimensions (in our notation the y-dimension) so that its lines can be applied sequentially to the AOD. In practice this is accomplished by detecting  $f(x, y)$  with a raster scanning TV camera. Since the correlation  $g(\xi, \eta)$  will be computed from the samples of  $f(x, y)$  we replace the integration over the continuous variable  $y$  in Eq. (1) by a summation:

$$g(\xi, \eta) = \sum_n \int f(x, n\Delta y) h(x+\xi, n\Delta y + \eta) dx. \quad (2)$$

$\Delta y$  is the sampling interval in the  $y$  direction and if it is chosen to be at the Nyquist rate (assuming  $f$  is bandlimited) the correlation  $g$  computed via Eq. (2) does not differ from the continuous correlation.  $N$  is the number of lines in  $f(x, y)$ . We can write the shift in the  $n$  direction by  $n\Delta y$  in the above equation as a

convolution with a delta function  $\delta(n+n\Delta y)$  and derive the following form for the correlation  $g(\xi, n)$ :

$$g(\xi, n) = \sum_n \int \int f(x, n\Delta y) h(x+\xi, n') dx \delta(n'-n-n\Delta y) dn' \quad (3)$$

This form of the correlation function determines directly the implementation algorithm of the acousto-optic image correlator. The term in the brackets in Eq. (3) is the 1-D correlation in the  $x$  direction of the  $n$ th line of the input image with all the lines of the reference. Several optical implementations of such a multi-channel 1-D correlator are possible. The term in the brackets in Eq. (3) is a function of two variables  $\xi$  and  $n'$ , and it must be shifted in the  $n'$  direction by the distance  $n\Delta y$ . In other words the 1-D correlations of the first line of the input are shifted by 1 pixel in the  $n'$  direction, while the correlations of the  $N$ th line are shifted by  $N$  pixels. This can be accomplished in an optical system in one of two ways. An optical scanner can be used after the multi-channel correlator to deflect the light by the appropriate distance for each input line. Alternatively (and in most cases preferably) a CCD camera can be used to detect the 1-D correlations and then shift the detected signal by transferring the charge on the CCD. The full 2-D correlation  $g(\xi, n)$  is formed by accumulating (summing over  $n$ ) the shifted 1-D correlation on the time integrating detector array. The operations that must be performed to implement this algorithm optically are summarized in the block diagram of Figure 1.

### HOLOGRAPHIC IMPLEMENTATION

We will describe this implementation [3] with the aid of Figure 2. The input pattern is detected by the TV camera. The horizontal sync of the camera is locked to a stable oscillator which acts as the master clock for the entire processor. Each pulse from this oscillator triggers the TV camera to produce an electronic signal corresponding to one of the lines in the input pattern. The video signal is heterodyned to the center frequency of the AOD and after amplification it is applied to the piezoelectric transducer of the AOD. At the end of each horizontal scan by the TV camera, the acoustic wave in the AOD is spatially modulated by the corresponding line of the input pattern. The clock from the master oscillator is delayed by the duration of one raster line and it triggers the pulsed laser that is used as the source in this processor. The duration of the light pulses is made shorter than the inverse of the bandwidth of the video signal. As a result the light diffracted by the AOD each time the laser is pulsed is spatially modulated by one of the lines of the input pattern. The diffracted light enters an astigmatic lens system which expands and collimates the light in the vertical direction. In the horizontal direction the light is Fourier transformed. A 1-D Fourier transform hologram of the reference image  $h(x, y)$  in our notation is placed in the Fourier plane of this astigmatic lens system. The hologram contains the reference image transformed in the  $x$  direction only. Since the light illuminating the hologram is collimated vertically, the light diffracted by the hologram is modulated by the product of the transform of the current line from the input pattern and all the lines of the reference image. A second

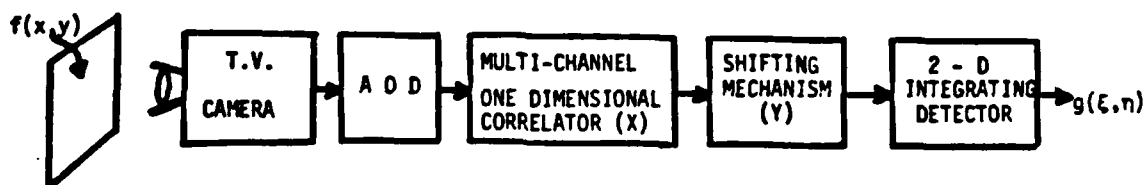


Figure 1. Block diagram of the acousto-optic implementation of the image correlator

A variety of specific optical implementations are possible using this algorithm and the trade-offs involved do not make one of the implementations clearly superior to the rest for all applications. In this paper we discuss a holographic implementation that shares all the characteristics of the algorithm

depicted in Figure 1: the input image is entered in the optical system via the TV camera and the acousto-optic device; a multi-channel 1-D correlator processes each line of the input image and a 2-D time integrating detector is used to accumulate the 1-D correlations and form the full 2-D correlation.

astigmatic lens system is placed after the hologram. The light is now imaged in the vertical direction and transformed again in the horizontal direction. The transform of the product of the transforms produces the correlation (or convolution if desired) between one of the input lines and all the lines of the reference image. The imaging that is performed in the vertical direction causes these 1-D correlations to appear stacked in the vertical direction at the output plane of the optical system. Returning momentarily to Eq. (3), the operation that has been performed up to this point in the processor is the 1-D integral of Eq. (3). A 2-D CCD detector is placed at the output plane of the processor. The photogenerated

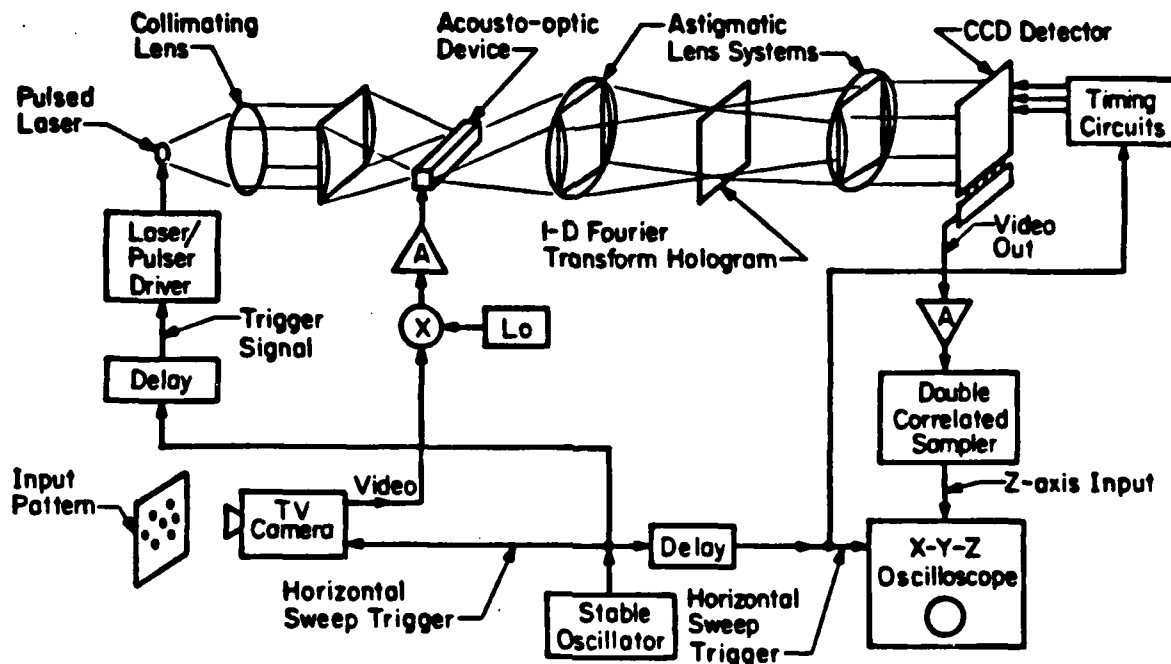


Figure 2. Acousto-optic/CCD image correlator.

2-D charge pattern that is stored in the CCD after it is exposed to the light from each laser pulse, is shifted vertically by one pixel. If we trace the location on the CCD of the charge generated during the  $n$ th light pulse we find that after the  $N$ th pulse occurs, it has travelled  $N-n$  pixels in the vertical direction. To obtain the 2-D correlation we must (according to Eq. (3)) shift the  $n$ th line by  $n$  pixels. Since  $N$  is fixed (it is the total number of lines in the input pattern) the CCD does perform the appropriate shifting and the entire 2-D correlation forms (shifted by  $N$  pixels) after integration on the CCD (the summation over  $n$  in Eq. 3) of the light incident on it from  $N$  light pulses. The correlation output is read-out continuously by the CCD in the form of a video signal which can be displayed or processed further electronically.

In this processor the 1-D correlations that are formed at the output of the optical system modulate the amplitude of the light. This optical wave must be interferometrically detected in order to obtain a detected signal proportional to the field amplitude rather than its intensity. The interferometric detection method [4] and experimental demonstration of it [5] have been discussed elsewhere. In this paper we wish to concentrate

on the 2-D operation that is being performed by the processor of Figure 2, when interferometric detection is not used. In this instance the pattern  $g^*(\xi, n)$  formed on the CCD is given by the following expression [4]:

$$g^*(\xi, n) = \sum_{n=1}^N \left| \int f(x, n\Delta y) h(x + \xi, n\Delta y + n) dx \right|^2 \quad (4)$$

The function  $g^*(\xi, n)$  is similar to the correlation in form, with the important exception that the 1-D correlations in the  $x$ -direction are squared before the summation in the second dimension is performed. This operation is clearly non-linear but it is shift invariant. Since  $g^*(\xi, n)$  can be very conveniently calculated with the acousto-optic image processor, we investigated its properties to determine its possible utility for pattern recognition. Using the Schwarz inequality it can be shown that

$$g^*(\xi, n) \leq \sum_n \left| \int |f(x, n\Delta y)|^2 dx \right|^2 = G^* \quad (5)$$

and the equality holds only for  $g^*(\xi, n) = G^*$ . This result is significant because it indicates that  $g^*(\xi, n)$  is maximized when the input and the reference images are matched and

aligned spatially. Therefore it could be used to recognized patterns. We must however consider the performance of a pattern recognition system based on this operation, when noise is present. A full analysis of this case is beyond the scope of this paper, but we will point out several important facts. First, the signal-to-noise ratio analysis that is typically performed to determine the performance of pattern recognition algorithms that are based on correlation is not appropriate in the nonlinear case. The non-linearity in  $g'$  results in noise components at the output that are not normally distributed and therefore the underlying distribution becomes important in the determination of the probabilities of detection and misclassification. Furthermore, patterns that belong to different classes but correlate well (and therefore are likely to be misclassified by a linear correlation algorithm) can be well separated by the non-linear correlation, and vice-versa. For instance, if

$$G = \sum_n \int |f(x, n\Delta y)|^2 dx, \quad (6)$$

is the value of the autocorrelation peak of the image  $f$ , we denote by  $\alpha G$  the peak value of the crosscorrelation between  $f$  and a second image  $h(x, y)$  not belonging to the same class as  $f$ .  $\alpha$  is a constant satisfying  $-1 < \alpha < 1$ . The non-linear crosscorrelation of the same two functions is denoted by  $\beta G'$ , where  $G'$  is defined in Eq. (5) and  $\beta$  is a constant satisfying  $0 < \beta < 1$ . It can be shown [6] that given  $\alpha$ ,  $\beta$  is in the range  $\alpha^2 < \beta < \alpha$  if the images involved are real and positive. Clearly  $\beta$  can be smaller than  $\alpha$ , which intuitively indicates that if this is the case two patterns can be separated more effectively with the non-linear correlation  $g'$ . More formally, we calculate the probability of false alarm (the probability of classifying  $h(x, y)$  as belonging to the class represented by  $f(x, y)$ ) as a function of the parameter  $\beta$  for the non-linear correlation case. This function is plotted in Figure 3 for an input SNR=1, assuming a linear processing gain of  $10^4$ , a value of  $\alpha = .7$  and for a fixed probability of detection  $P_D = .96$ . On the same diagram the probability of false alarm that we obtain under the same conditions using linear correlator is indicated. We note that in

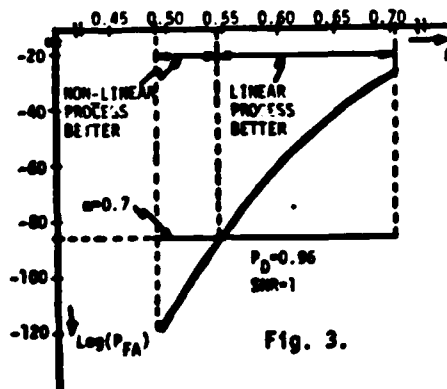


Fig. 3.

Figure 3 there is a very low probability of false alarms for both cases (this is a somewhat superfluous case since  $\alpha$  is relatively low and the SNR is high) but we can also see that the probability of false alarm can be smaller for the non-linear correlator. Of course it can also be higher depending on the value of  $\beta$ .  $\beta$  is determined by the images  $f$  and  $h$  and therefore we conclude from this exercise that a recognition algorithm based on non-linear correlation can out-perform the linear correlator for a certain class of images. In general, the non-linear correlation can provide adequate performance for a large class of pattern recognition applications. A complete statistical characterization of the non-linear correlation will be presented in a future publication.

### EXPERIMENTAL PROCESSOR

A photograph of the experimental acousto-optic/CCD image correlator is shown in Figure 4. The apparatus is a hardware implementation of the system shown in Figure 3. The light source used in this experiment is a pulsed laser diode with 50 nsec pulse width. The inverse of the pulse width ( $1/50 \text{ nsec} = 20 \text{ MHz}$ ) must be at least twice the video bandwidth, therefore video signals with up to 10 MHz bandwidth can be processed with the system. The peak power of this laser can be as high as  $9 \text{ W}$ , resulting in an average light power of approximately 10 mW which is adequate for detection by the CCD. A custom fabricated acousto-optic device was the input electronic-to-optical transducer. This device is a shear acoustic wave  $\text{TeO}_2$  Bragg cell, with 30 MHz 1dB bandwidth at 820 nm (the laser wavelength), in excess of 400% watt diffraction efficiency and most significantly, the acoustic delay of the device is 70  $\mu\text{sec}$ . The long acoustic delay is required in this processor so that we can accommodate an entire standard video line (63  $\mu\text{sec}$ ). The light diffracted by the AOD is demagnified by a factor of approximately 4 with two spherical lenses, in order to match the size of the video lines from the AOD (4 cm) with the size of the transparencies used to fabricate the hologram (1 cm). The demagnified Schlieren image of the AOD is reflected towards the hologram and Fourier transformed. The hologram was formed from a transparency recorded on a high speed holographic plate (to avoid the phase distortion introduced by the plastic substrate of film) with a HeNe laser. The components that are used for recording the hologram are visible in the far end of the optical bench in Figure 4. The holograms are recorded on dichromated gelatin to obtain high diffraction efficiency. We obtain in excess of 20% efficiency with the dichromated gelatin holograms at 820 nm. The light diffracted by the hologram is reflected towards the CCD, imaged vertically and transformed horizontally. The CCD used in the experiment is a commercially available (Fairchild) 1-D device oriented vertically. Special timing and driving electronic circuits were built to operate the device in the time-delay-and-integrate (TDI) mode necessary for this processor. The 1-D array produces slices of the 2-D correlation surface in the  $\eta$  direction, for a fixed  $\xi$  value. The slices

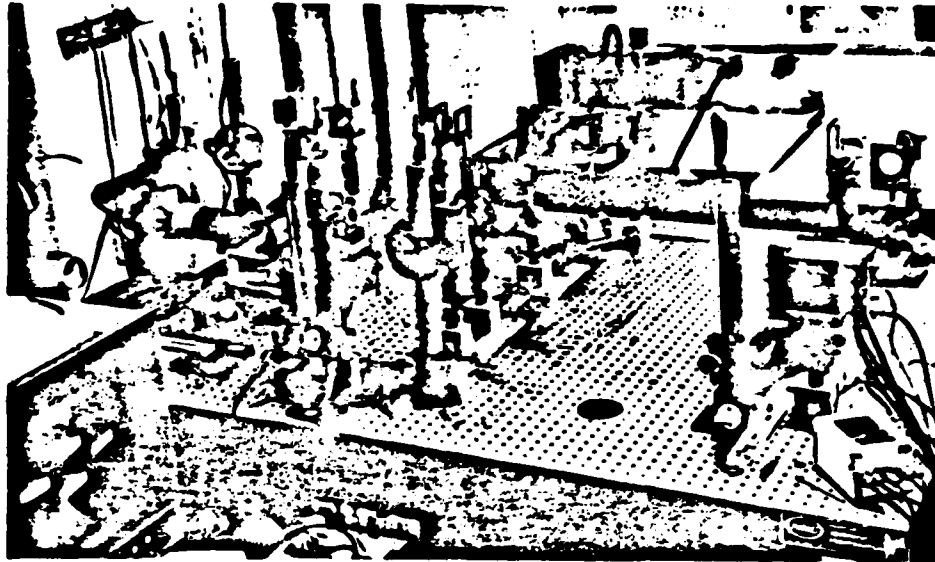


Figure 4. Experimental Acousto-optic/CCD image correlator.

for different  $\xi$  values can be observed by translating the CCD horizontally. A 1-D CCD was chosen for this initial experiment, rather than a 2-D CCD which can produce the entire 2-D correlation simultaneously, because its output can be easily monitored on an oscilloscope which has allowed us to easily align and calibrate the system. The input pattern (shown in Figure 5a) was detected by a high resolution TV camera (not shown in

Figure 4). The output signal from the CCD for 5 horizontal positions is shown in Figure 5b. This composite photograph is the 2-D autocorrelation of the pattern in Figure 5a computed by the system in Figure 4. Interferometric detection was not used in these experiments, therefore the non-linear correlation described by Eq. 4 is obtained. The pattern in Figure 5a is in good agreement with the autocorrelation expected from the simple pattern in Figure 5a. We attribute the asymmetries noticeable in Figure 5b to non-linearities and phase distortion in the hologram.

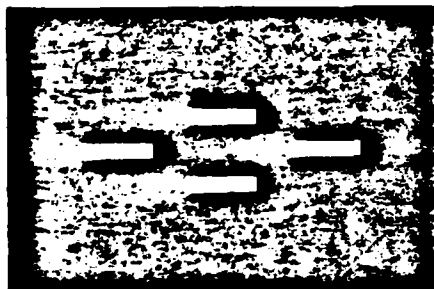
#### ACKNOWLEDGMENTS

The research reported in this paper is supported by the Army Research Office and the Air Force Office of Scientific Research.

We thank Dr. Peter Kellman for his assistance in the design of the acousto-optic device used in the experiments and Mr. Ed Roos from Crystal Technology for the fabrication of the device.

#### REFERENCES

- [1] Special issue on Acousto-optic Signal Processing, Proc. IEEE, Vol. 69, 1, Jan. 1981.
- [2] K. Bromley, et. al., Proc. SPIE, Vol. 118, p. 118, 1977
- [3] D. Psaltis, J. Opt. Soc. Am., 71, p. 198, 1981
- [4] D. Psaltis, Appl. Opt., 21, p. 491, 1982
- [5] M. Haney and D. Psaltis, this volume.
- [6] S. Venkatesh and D. Psaltis, to be published.



(a)



(b)

Fig. 5(a). Input Pattern (b) Optically Computed Auto-Correlation



# Real-time optical synthetic aperture radar (SAR) processor

Demetri Psaltis  
Kelvin Wagner

California Institute of Technology  
Department of Electrical Engineering  
Pasadena, California 91125

**Abstract.** A real-time optical synthetic aperture radar (SAR) processor is described. The processor utilizes an acousto-optic device as the input electronic-to-optical transducer and a CCD camera that serves as the optical detector and simultaneously performs the focusing of the SAR image in the azimuth direction.

**Keywords:** two-dimensional signal processing; synthetic aperture radar; acousto-optic devices; imaging; image processing.

*Optical Engineering* 21(5), 822-828 (September/October 1982).

## CONTENTS

1. Introduction
2. Synthetic aperture radar (SAR) signals
3. Acousto-optic/CCD SAR processor
4. Discussion
  - 4.1. Azimuth resolution
  - 4.2. Image size in azimuth
  - 4.3. Range resolution
  - 4.4. Image size in range
  - 4.5. Flexibility
  - 4.6. Dynamic range
5. Experiment
6. Acknowledgments
7. Appendix A: derivation of Eq. (14)
8. Appendix B: derivation of Eq. (15)
9. References

## 1. INTRODUCTION

Synthetic aperture radar (SAR) still represents the most successful application of optical computing, even though more than 30 years have elapsed since the initial demonstration of the optical SAR processor. Optical computers are used routinely today to form SAR images from radar signals that are collected by aircraft or spacecraft and recorded on photographic film. The requirements of modern radars, however, are often not met by the present film-based optical processors. These requirements include higher image quality (resolution, dynamic range, artifacts, etc.), real-time image formation, flexibility, and on-board processing capability. In order to meet such requirements, digital computers are increasingly being used to form SAR images. The dramatic advances in microelectronics in recent years have made it feasible to construct digital SAR processors that can provide better image quality (due to the highest accuracy and the flexibility in programming a digital computer) than film-based SAR processors. In addition, digital processors can be built (as they have in some cases) that have real-time and on-board processing capabilities. It is not the purpose of this paper to present a comparison of optical versus digital techniques in SAR (the interested reader is referred to Ausherman's paper<sup>1</sup>), but it is necessary to point out that a number of problems remain with digital SAR processors. The complexity of these systems results in a very costly, power consuming, relatively large

and heavy processor. Thus, even though it is conceivable to build a low resolution real-time digital processor, for many of the applications this is an impractical solution.

Very significant advances have also been achieved in the area of electro-optics which have resulted in corresponding improvements in the state of the art of optical computers. Specifically, acousto-optic technology has matured, and consequently high quality devices are now available to be used as the input spatial light modulator; semiconductor detector arrays (CCD's and photodiode arrays) have proven to be excellent as detectors in the optical computer, and the semiconductor light sources (LED's and laser diodes) which have been developed primarily for optical communications, are a very efficient light source in many optical processors. These and other developments have made it possible to construct real-time, high performance, power efficient, compact and relatively inexpensive optical computers such as the acousto-optic spectrum analyzer<sup>2</sup> and the ambiguity function radar processors.<sup>3</sup> In this paper we describe an optical SAR processor in which the modern components available for optical computing are fully utilized, and, therefore, we believe that the resulting processor has great potential for applications where on-board, real-time SAR image formation is required.

In Sec. 2 the fundamentals of SAR are reviewed, in order to establish the notation we will be using in the paper. A comprehensive treatment of SAR can be found in Refs. 4 and 5. In Sec. 3 the operation of the optical processor is described in detail, and in Sec. 4 we discuss its performance characteristics. Our experimental results to date are reported in Sec. 5.

## 2. SAR SIGNALS

The side-looking SAR geometry is depicted in Fig. 1. The vehicle (aircraft or spacecraft) is traveling with a constant velocity  $v$  along the  $\eta$  direction and at height  $h$ . Coded pulses are emitted periodically through an antenna mounted on the side of the vehicle. In this paper we assume that the pulses are chirp coded. The transmitted waveform  $S(t)$  in complex notation is given by

$$S(t) = \sum_n \text{rect} \left[ \frac{t - nT}{\tau} \right] \exp[jb(t - nT)^2] \exp(j2\pi v_0 t) \quad (1)$$

where  $\tau$  is the pulse duration,  $1/T$  is the pulse repetition frequency (PRF),  $b$  is the chirp rate, and  $v_0$  is the microwave frequency of the radar. The transmitted waveform illuminates a patch of the surface to be imaged (the ground), and part of it is reflected back towards the

Invited Paper TD-103 received Apr. 12, 1982; accepted for publication Apr. 19, 1982; received by Managing Editor May 10, 1982.  
© 1982 Society of Photo-Optical Instrumentation Engineers.

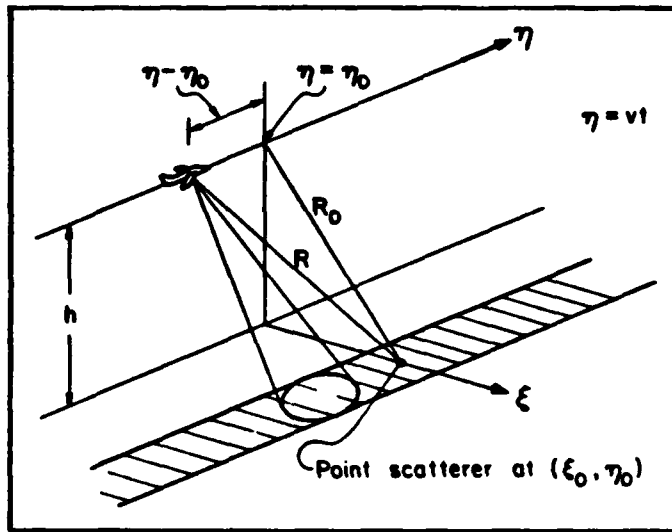


Fig. 1. Synthetic aperture radar geometry.

vehicle and detected by the antenna. The objective of SAR is to form an image of the ground from these reflections. We will discuss how an image of a single point scatterer (impulse) located at coordinates  $\xi = \xi_0$  and  $\eta = \eta_0$  on the ground can be formed. Since the SAR image formation is a linear operation, knowledge of the impulse response completely describes the system. The signal received by the antenna due to a single point scatterer is

$$r(t) = A(t) S(t - 2R/c), \quad (2)$$

where  $R$  is the instantaneous range from the antenna to the point scatterer at  $(\xi_0, \eta_0)$ .  $A(t)$  is the far-field pattern of the antenna. From the geometry of Fig. 1,  $R$  can be written as

$$R(t) = \sqrt{(\eta_0 - \eta)^2 + R_0^2} = \sqrt{(\eta_0 - vt)^2 + R_0^2}, \quad (3)$$

where  $R_0 = \sqrt{h^2 + \xi_0^2}$  is the range when the vehicle crosses  $\eta = \eta_0$ . In most cases, the variation of the range  $R(t)$  with time can be neglected within the duration  $\tau$  of a single radar pulse, and therefore  $R(t) \approx R(nT)$ . In addition, the range  $R_0$  is typically much greater than the distance  $|\eta - \eta_0|$ . This allows us to expand the square root in Eq. (3) as follows:

$$R(t) \approx R(nT) \approx R_0 + \frac{(vnT - \eta_0)^2}{2R_0}. \quad (4)$$

Using the above equation and Eq. (1), we can rewrite Eq. (2) as

$$r(t) = \sum_n A(nT) \text{rect} \left[ \frac{t - 2R_0/c - \Delta\tau - nT}{\tau} \right] \times \exp[jb(t - 2R_0/c - \Delta\tau - nT)^2] \times \exp(j2\pi\nu_0 t) \exp(-j2\pi\nu_0 2R_0/c) \exp(-j2\pi\nu_0 \Delta\tau). \quad (5)$$

The variation of the antenna pattern  $A(t)$  during a single pulse can be neglected, and hence  $A(t) \approx A(nT)$ . The quantity  $\Delta\tau = (vnT - \eta_0)^2 / R_0 c$  has units of time and is very small compared to  $2R_0/c$  if  $R_0 \gg |\eta - \eta_0|$ . Therefore,  $\Delta\tau$  can be neglected in Eq. (5) except in the term  $\exp(-j2\pi\nu_0 \Delta\tau)$  because in this term  $\Delta\tau$  is multiplied by  $\nu_0$  which is the very large radio frequency. The term  $\exp(-j4\pi\nu_0 R_0/c)$  is an inconsequential constant phase term and can be omitted. With these modifications, we can write the final form for  $r(t)$  as

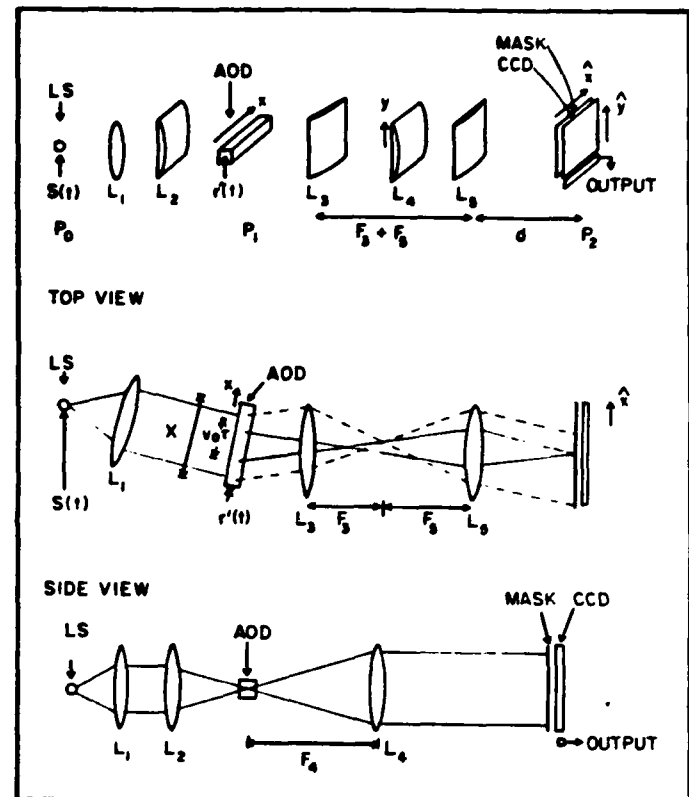


Fig. 2. Acousto-optic/CCD synthetic aperture radar processor. (LS—light source, AOD—acousto-optic device,  $F_1$  is the focal length of the lens  $L_1$ , and the broken lines indicate the path of the rays of the reference wave.)

$$r(t) = \sum_n A(nT) \text{rect} \left[ \frac{t - 2R_0/c - nT}{\tau} \right] \times \exp[jb(t - 2R_0/c - nT)^2] \exp[-j(2\pi\nu_0/cR_0)(vnT - \eta_0)^2] \times \exp(j2\pi\nu_0 t). \quad (6)$$

The received signal  $r(t)$  must be processed to produce an image of the point scatterer on the ground. In the next section we will describe in detail how the real-time optical processor that is presented in this paper forms the SAR image from the signal  $r(t)$ . In deriving Eq. (6), a number of simplifying assumptions and approximations were made, which may or may not be justifiable in practice depending on the particular application. We will proceed with the description of the system based on this relatively simple form of the SAR equation [Eq. (6)], and in Sec. 4 we will discuss the necessary modifications to the system for cases in which the conditions set in this section are not met.

### 3. ACOUSTO-OPTIC/CCD SAR PROCESSOR

A schematic diagram of the processor is shown in Fig. 2. The system is illuminated by a pulsed laser. The light amplitude of the source is modulated by

$$P(t) = \sum_n \text{rect} \left[ \frac{t - nT}{\tau_0} \right], \quad (7)$$

where  $\tau_0$  is the duration of each light pulse. The spherical lens  $L_1$  collimates the light from the source, and the cylindrical lens  $L_2$  focuses the light in the vertical ( $y$ ) direction so that it can pass through the aperture of the acousto-optic device (AOD) placed in plane  $P_1$ . The received radar signal  $r(t)$  is heterodyned to the center frequency  $\nu_1$  of the AOD, and a reference signal  $B \exp(j2\pi\nu_2 t)$  is

added to it. The frequency  $v_2$  is chosen such that the difference  $v_2 - v_1$  is equal to the bandwidth of each radar pulse:

$$v_2 - v_1 = b\tau/\pi. \quad (8)$$

The need for the reference signal will become apparent shortly. The resulting signal  $r'(t)$  is related to  $r(t)$  by the following equation:

$$r'(t) = r(t) \exp[-j2\pi(v_0 - v_1)t] + B \exp(j2\pi v_2 t). \quad (9)$$

$r'(t)$  is applied to the piezoelectric transducer of the AOD of Fig. 2. The light diffracted by the AOD is modulated by<sup>4</sup>

$$S_1(t, x) = \text{rect} \left( \frac{x}{X} \right) P(t) r' \left( t + \frac{x}{v_a} \right), \quad (10)$$

where  $x$  is along the direction of propagation of the acoustic wave,  $X$  is the aperture of the AOD, and  $v_a$  is the speed of sound in the AOD. The undiffracted light is blocked in the focal plane of the cylindrical lens  $L_3$ . The combination of lenses  $L_2$  and  $L_3$  accomplishes two tasks. First, since the two lenses are separated by the sum of their focal lengths, a single plane wave incident on  $L_3$  will be recollimated when it exits the lens  $L_3$ . In addition, the impulse response of the system in the  $x$  direction from plane  $P_1$  to plane  $P_2$  is made to be equal to

$$h(x, \hat{x}) = \exp[jb_1(x - \hat{x})^2] \exp(-j2\pi v_1 x/v_a). \quad (11)$$

where  $\hat{x}$  is the horizontal coordinate in plane  $P_2$ . The constant  $b_1$  can be set by appropriately choosing the focal lengths of  $L_2$  and  $L_3$  and the distance  $d$ . The term  $\exp(-j2\pi v_1 x/v_a)$  reflects the fact that the optical system following the Bragg cell is tilted so that its optical axis coincides with a wave diffracted at the Bragg angle. In Eq. (11) we assume that the effects of the lens apertures are negligible. In the vertical direction  $y$ , the light is recollimated by the lens  $L_4$ , and therefore the amplitude of light entering plane  $P_2$  does not vary along  $y$ . At  $P_2$  a transparency is placed immediately in front of the CCD camera. The intensity transmittance  $T(\hat{x}, \hat{y})$  of this mask is

$$T(\hat{x}, \hat{y}) = \frac{1}{2} + \frac{1}{2} \cos \left[ 2\pi u_0 \hat{x} + \frac{b_2 \hat{y}^2}{\hat{x}} \right], \quad (12)$$

where  $u_0$  and  $b_2$  are constants that will be specified later. The instantaneous intensity incident on the CCD is given by

$$I(\hat{x}, \hat{y}, t) = T(\hat{x}, \hat{y}) \left| \int S_1(t, x) h(x, \hat{x}) dx \right|^2. \quad (13)$$

The CCD is operated in the shift-and-add mode.<sup>7</sup> In this mode of operation the device is exposed to light periodically. The photogenerated charge is accumulated on the detector for a short time interval, and after each exposure the entire photogenerated charge pattern is electronically shifted by one pixel along one of the dimensions of the CCD. The photogenerated charge due to the next exposure is simply added to the charge that is already stored in each pixel, and then the process is repeated. In our system the charge transferring is done in synchronism with the PRF of the radar, and the integration period is set equal to the period  $T$  of the radar. The charge generated on the CCD during the  $n$ th radar pulse is given by

$$\begin{aligned} Q(\hat{x}, \hat{y}, n) &= \int_{t=nT/2}^{t=(n+1)T/2} I(\hat{x}, \hat{y}, t) dt \\ &= 2Bv_a \tau \tau_0 T(\hat{x}, \hat{y}) A(nT) \text{sinc} \left[ \frac{b\tau}{\pi v_a} \left( \hat{x} - \frac{2R_0 v_a}{c} \right) \right] \end{aligned}$$

$$\begin{aligned} &\times \cos \left[ \frac{2\pi(v_2 - v_1)\hat{x}}{v_a} + \frac{2\pi v_0}{cR_0} (v_n T - \eta_0)^2 + \phi \right] \\ &+ \text{bias terms}. \end{aligned} \quad (14)$$

The derivation of Eq. (14) is straightforward but tedious, and it is presented in Appendix A. This charge pattern gets shifted along the  $\hat{y}$  direction by  $(N - n)$  pixels on the CCD, after  $N$  exposures have taken place. The total charge that accumulates at each pixel located at coordinates  $(\hat{x}, \hat{y})$  after  $N$  exposures is

$$\begin{aligned} Q(\hat{x}, \hat{y}) &= \sum_n^N Q[\hat{x}, \hat{y} + (N - n)\Delta y, n] \\ &= \frac{Bv_a \tau \tau_0}{2} \text{sinc} \left[ \frac{b\tau}{\pi v_a} \left( \hat{x} - \frac{2R_0 v_a}{c} \right) \right] \text{sinc} \left[ \frac{2Nv_0 v^2 T^2}{c\Delta y R_0} \right] \\ &\times \left( \hat{y} - \eta_0 \frac{\Delta y}{vT} + N\Delta y \right) \cos [4\pi u_0 \hat{x} + \phi] \\ &+ \text{bias terms}. \end{aligned} \quad (15)$$

In the above equation  $\Delta y$  is the pixel separation in the CCD,  $u_0 = (v_2 - v_1)/v_a$ , and  $\phi$  is a constant phase term.  $Q(\hat{x}, \hat{y})$  is the final output of the processor, and its form demonstrates the imaging capability of the system. In the  $\hat{x}$  direction,  $Q(\hat{x}, \hat{y})$  is a sinc function with width  $\pi v_a/b\tau$  and centered at  $\hat{x} = 2R_0 v_a/c$ . In other words, we obtain the image of the point scatterer located at  $\xi = \xi_0$  on the ground, focused in the  $\xi$  direction. The resolution in the  $\xi$  direction is equal to  $\delta_\xi = \pi c/2b\tau$ . This is a well-known result for range resolution in radar systems.<sup>8</sup> The carrier at spatial frequency  $2u_0$  arises from the inclusion of the reference signal in the acousto-optic device which allowed us to record on the CCD the phase of the detected signals. This is necessary in this system because the Doppler information that is essential for the focusing in the azimuth ( $\eta$ ) direction is encoded in the phase of the range compressed signal  $Q(\hat{x}, \hat{y}, n)$ . In addition, since the output forms on a carrier, it can be easily separated from the bias term in Eq. (15).

In the  $\hat{y}$  direction,  $Q(\hat{x}, \hat{y})$  is also a sinc function whose position is proportional to  $\eta_0$ , the location of the point scatterer on the ground in the azimuth direction. The width of this sinc function is equal to  $c\Delta y R_0/Nv_0 v^2 T^2$ , and it determines the resolution in azimuth. In ground coordinates  $\eta$ , the width of the sinc function corresponds to an azimuth resolution

$$\delta_\eta = \frac{cR_0}{2Nv_0 vT} = \lambda_0 R_0/2D_s.$$

$D_s = NvT$  is the distance that the vehicle collecting the SAR data travels during the time interval  $NT$ , and it is equal to the synthetic aperture of the system. Therefore, the azimuth resolution obtained with this processor conforms with previously derived results<sup>9</sup> for SAR systems. The entire pattern is shifted in the  $\hat{y}$  dimension by the distance  $N\Delta y$ . For a CCD with  $N$  pixels in the horizontal direction, this implies that after the signal is integrated on the CCD for  $N$  pulses to produce a focused image, it arrives at the edge of the device (at  $\hat{y} = N\Delta y$ ) where a separate CCD stage transfers an entire line of the data (a slice of the image for each azimuth position) to the output pin of the CCD device. The azimuth slices are continuously produced as long as the flight continues, producing in real time an image of a long strip on the ground parallel to the direction of the flight.

#### 4. DISCUSSION

In this section we discuss some of the issues relative to the performance of the optical processor we have described. We will address

several performance criteria separately and comment on the effects of the processor architecture and the devices used in the system. A complete in-depth analysis of the performance is beyond the scope of this paper.

#### 4.1. Azimuth resolution

In the previous section we derived the formula for the resolution that can be obtained in the along track (azimuth) direction:

$$\delta_y = \frac{cR_0}{2Nv_0T} \quad (16)$$

$N$  is the only parameter in the above equation that is related to the processor.  $N$  is the number of radar pulses that are used to form the SAR image of each point scatterer on the ground. In the AO/CCD processor,  $N$  is also equal to the number of pixels of the CCD in the shifting direction ( $\hat{y}$ ). Commercially available CCD cameras have approximately 500 pixels. Several devices with approximately twice this number have recently been developed<sup>9</sup> or are currently under development. If a CCD with  $10^3$  pixels is used, the azimuth resolution obtainable with this processor is 22.5 meters on the ground. This figure was obtained by using the parameters of the SEASAT radar<sup>9</sup> that was flown by NASA. The azimuth resolution will, of course, be different for different radars. To obtain lower resolution, larger CCD's would have to be used. It is unlikely that a significant increase in the size of monolithic CCD cameras will take place in the near future. It is possible, however, to construct larger arrays by interfacing a number of separate chips. As  $N$  is increased and finer resolution is achieved, other factors in the processor become limiting, such as optical aberrations, mechanical/electronic stability, and light source coherence over the time period  $NT$ . Finally, for low resolution imaging, some of the approximations that were made in Sec. 2 may not be valid. For instance, if the approximation that the range of each point target remains constant as the plane flies past it is not valid, an effect known as range curvature<sup>4</sup> results. Range curvature can be corrected in our processor simply by tilting one of the cylindrical lenses in the system which introduces barrel distortion that can exactly cancel out the range curvature.

#### 4.2. Image size in azimuth

The AO/CCD processor continuously produces slices of the SAR images in the azimuth direction, and therefore the size of the SAR image is not limited by the processor in this direction.

#### 4.3. Range resolution

The resolution in the range direction ( $\hat{z}$ ) on the ground is given by

$$\delta_z = \frac{\pi c}{2b\tau} \quad (17)$$

The bandwidth of the chirped radar pulses is equal to  $b\tau/\pi$ , and therefore the resolution in range is limited by the temporal bandwidth of the processor. The bandwidth of the AOD used in the system is not the primarily limiting factor since devices with several gigahertz bandwidth are available. More importantly, the duration of the light pulse  $\tau_0$  must be shorter than the inverse of the bandwidth of the signal to avoid smearing of the range compressed signal [Eq. (14)]. For typical radar bandwidths,  $\tau_0$  should be several nanoseconds. Several laser sources are capable of producing nanosecond pulses with adequate peak power. We are primarily considering laser diodes because they are compact and power efficient. Laser diodes can lase in a single mode under cw operation (and therefore be coherent), but when they are pulsed, several modes exhibit gain during the transients. The need for coherence in the system imposes with present state-of-the-art devices a minimum pulse width of ~20 ns. Therefore, if a laser diode is used in the system, the bandwidth of the radar must be equal to 50 MHz, which corresponds to range resolution equal to 3 m. This can be lowered by an order of magni-

tude if a pulsed gas laser is used. The additional factors mentioned in our discussion on azimuth resolution also become increasingly important for finer range resolution.

#### 4.4. Image size in range

The number of pixels in the range direction is limited by the space-bandwidth product of the AOD or the CCD in the nonshifting direction, whichever is smaller. At the present time, the CCD imposes this limit at approximately  $10^3$  pixels. The range coverage can be extended by using several processors operating in parallel.

#### 4.5. Flexibility

A potential application for the AO/CCD processor is on-board real-time image formation. In such applications the radar geometry can be expected to change from time to time or even continuously. Enough flexibility must be built into the system so that it can be adaptable to the changing conditions. One method for achieving this is by the use of a real-time 2-D spatial light modulator<sup>6</sup> in place of the fixed mask in Fig. 2. The impulse response of the processor can then be altered to track changes in the radar geometry.

#### 4.6. Dynamic range

The dynamic range is defined as the maximum unsaturated brightness in the SAR image divided by the minimum detectable level above the noise. In general, a large dynamic range can be observed in a SAR image because the noise detected at radio frequencies is very effectively suppressed through the pulse compression in both range and azimuth that is performed to bring the SAR image into focus. The potential for high dynamic range, however, can only be realized if the processor that forms the SAR image can provide it. In an optical processor, essentially every component of the system contributes to diminish the dynamic range available at the output by adding noise or by introducing nonlinearities and aberrations in the system. In the AO/CCD processor, the CCD detector is the dominant factor that limits the dynamic range. The maximum brightness of the SAR image is equal to the maximum charge that can be stored in each pixel of the CCD, minus the charge that corresponds to the bias terms in Eq. (15) and the dark current that accumulates during the integration time. The bias is signal dependent and is largest at portions of the SAR image that have maximum *average* intensity. Therefore, relatively sparse objects can be imaged with a larger dynamic range. For a single point scatterer on the ground, the bias can be only 1/2 of the full dynamic range of the CCD, but for a distributed target the bias increases as  $\sqrt{M}$ , where  $M$  is the average number of point scatterers on the ground that are located at the same range in a distance  $NvT$  along the azimuth direction. The minimum detectable level at the output of the processor is determined by the fixed pattern noise of the CCD (the variation of the dark current from pixel to pixel), optical scattering, quantum noise primarily due to the bias, and thermal and amplifier noise from the electronics.<sup>10</sup> Our calculations<sup>11</sup> show that the dynamic range of the images that will be produced by the experimental processor we are presently constructing is ~200:1. A commercially available CCD camera is used in the experimental processor, and post-detection signal processing is applied in order to minimize noise. The dynamic range can be increased to over  $10^3$ :1 by cooling the CCD to eliminate the dark current and by using a CCD specifically designed for this application.

### 5. EXPERIMENT

The CCD camera is utilized in this system not only as the optical detector but also as a multichannel correlator by operating it in the shift-and-add mode described earlier. The signal that comes out at each column (at position  $\hat{x}$ ) of the device is the correlation between the transmittance of the mask as a function of  $\hat{y}$  at the same position  $\hat{x}$  and the signal corresponding to the temporal variation of the incident light intensity. We have performed an experiment to demonstrate the operation of the CCD as an optical multichannel correlator. The experimental setup is shown in Fig. 3. A light emitting diode (LED) is used as the light source. The intensity of the LED is

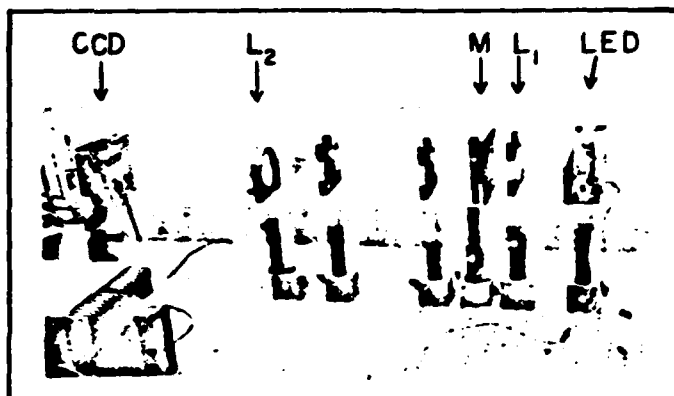


Fig. 3. Experimental electro-optic ambiguity function processor. (LED—light emitting diode,  $L_1$ —collimating lens,  $M$ —mask,  $L_2$ —imaging lens, CCD—camera.)

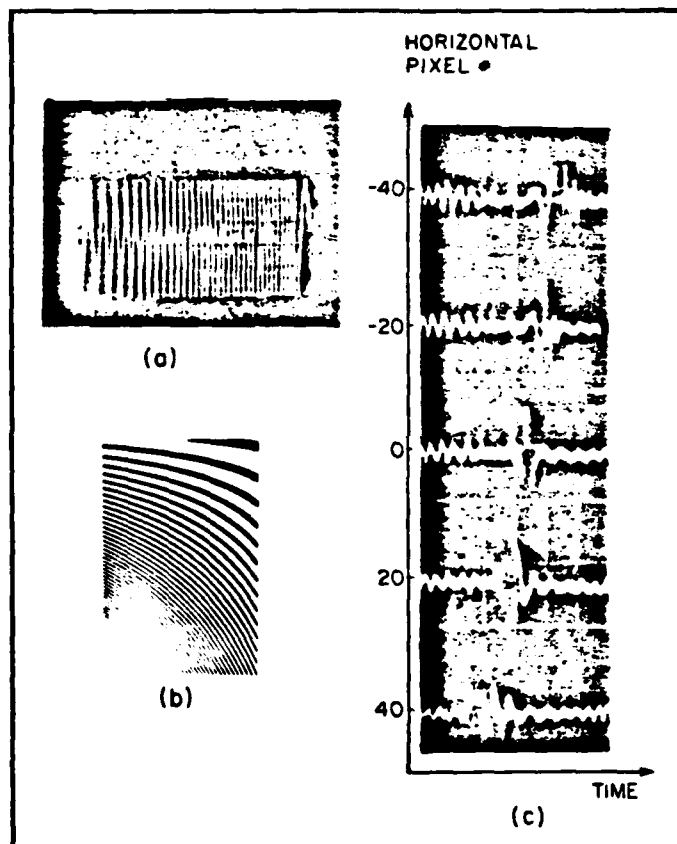


Fig. 4. Ambiguity processor signals: (a) input (LED) waveform; (b) mask; (c) ambiguity function.

temporally modulated by the chirp signal shown in Fig. 4(a). The chirp signal that modulates the LED represents the variation of the intensity detected by the CCD [the function  $Q(\hat{x}, \hat{y}, n)$  in Eq. (14)] as a function of pulse number  $n$ . The duration of this waveform is equal to  $NT$ , and its bandwidth is equal to  $v_0^2 NT / cR_0$ .<sup>5</sup> The bandwidth of the waveform in Fig. 4(a) is 30 Hz, and its duration is 1 s. The CCD we used in this experiment has  $N = 512$  pixels in the vertical dimension, and therefore the duration of one second corresponds to a radar pulse repetition frequency equal to  $1/T = 0.5$  kHz. These parameters were chosen to be approximately equal to the parameters of an experimental aircraft radar which is flown periodically by the Jet Propulsion Laboratory. We intend to use data collected by this radar to test the processor when it is completed.

The light from the LED is collimated by lens  $L_1$  in Fig. 3, and it

illuminates the mask denoted by  $M$  in Fig. 3. A photograph of this mask is shown in Fig. 4(b). The intensity transmittance in the vertical direction is a chirp signal whose chirp rate is proportional to the horizontal position. The signal at the center of the mask matches the waveform that is used to modulate the LED. The mask is imaged by lens  $L_2$  onto the CCD, which is operated in the shift-and-add mode. The output signal from the CCD at each horizontal position is the correlation of the waveform modulating the LED and the transmittance of the mask at that horizontal position. The output waveforms from the CCD from selected vertical locations are shown in Fig. 4(c). This 2-D waveform is known as the ambiguity function<sup>12</sup> of the chirp signal, and Fig. 4(c) displays the familiar tilted-ridge structure of the ambiguity function for this particular waveform.

## 6. ACKNOWLEDGMENTS

We thank Tom Bicknell from the Jet Propulsion Laboratory (JPL) for the technical information he has provided to us on SAR systems and for loaning to us some of the equipment used in the experiments. The research reported in this paper is supported by NASA and JPL and in part by the Air Force Office of Scientific Research.

## 7. APPENDIX A: DERIVATION OF EQUATION (14)

$$Q(\hat{x}, \hat{y}, n) = \int_{t-nT/2}^{t+nT/2} I(\hat{x}, \hat{y}, t) dt. \quad (14)$$

Substituting Eq. (13) in Eq. (14):

$$Q(\hat{x}, \hat{y}, n) = T(\hat{x}, \hat{y}) \int_{t-nT/2}^{t+nT/2} \left| \int S_1(t, x) h(x, \hat{x}) dx \right|^2 dt. \quad (A1)$$

We will first evaluate the integral over  $x$  in the above expression. Using Eqs. (10) and (11):

$$\begin{aligned} g(t, \hat{x}) &= \int S_1(t, x) h(x, \hat{x}) dx \\ &= \int \text{rect} \left( \frac{x}{X} \right) P(t) r' \left( t + \frac{x}{v_a} \right) \exp[jb_1(x - \hat{x})^2] \\ &\quad \times \exp \left( -j \frac{2\pi v_1 x}{v_a} \right) dx. \end{aligned} \quad (A2)$$

Substituting the expressions for  $P(t)$  and  $r'(t)$  from Eqs. (7) and (9):

$$\begin{aligned} g(t, \hat{x}) &= \sum_n \text{rect} \left( \frac{t-nT}{\tau_0} \right) \int \text{rect} \left( \frac{x}{X} \right) \\ &\quad \times \left\{ r \left( t + \frac{x}{v_a} \right) \exp \left[ -j2\pi(v_0 - v_1) \left( t + \frac{x}{v_a} \right) \right] \right. \\ &\quad \left. + B \exp \left[ j2\pi v_2 \left( t + \frac{x}{v_a} \right) \right] \right\} \\ &\quad \times \exp[jb_1(x - \hat{x})^2] \exp \left( \frac{-j2\pi v_1 x}{v_a} \right) dx. \end{aligned} \quad (A3)$$

and the expression for the received signal  $r(t)$  from Eq (6) is

$$\begin{aligned}
 g(t, \hat{x}) = & \sum_n \text{rect} \left( \frac{t-nT}{\tau_0} \right) \int \text{rect} \left( \frac{x}{X} \right) \left\{ \sum_n A(nT) \text{rect} \left[ \frac{t-2R_0/c-nT+x/v_a}{\tau} \right] \exp [jb(t-2R_0/c-nT+x/v_a)^2] \right. \\
 & \times \exp \left[ -j \frac{2\pi v_0}{cR_0} (vnT-\eta_0)^2 \right] \exp [j2\pi v_0(t+x/v_a)] \exp [-j2\pi(v_0-v_1)(t+x/v_a)] + B \exp [j2\pi v_2(t+x/v_a)] \Big\} \\
 & \times \exp [jb_1(x-\hat{x})^2] \exp (-j2\pi v_1 x/v_a) dx .
 \end{aligned} \quad (A4)$$

The laser pulse width  $\tau_0$  is chosen sufficiently smaller than the bandwidth of the radar pulses ( $\tau_0 < b\tau/\pi$ ) so that the temporal variation of the signal in the above equation can be neglected over the duration of each light pulse. With this approximation Eq. (A4) can be rewritten as follows:

$$\begin{aligned}
 g(t, \hat{x}) = & \sum_n \text{rect} \left( \frac{t-nT}{\tau_0} \right) \exp(j2\pi v_1 t) \int \text{rect} \left( \frac{x}{X} \right) \left\{ \sum_n A(nT) \text{rect} \left[ \frac{x/v_a-2R_0/c}{\tau} \right] \exp [jb(x/v_a-2R_0/c)^2] \right. \\
 & \times \exp \left[ \frac{-j2\pi v_0}{cR_0} (vnT-\eta_0)^2 \right] + B \exp [j2\pi(v_2-v_1)x/v_a] \exp [j2\pi(v_2-v_1)nT] \Big\} \exp [jb_1(x-\hat{x})^2] dx .
 \end{aligned} \quad (A5)$$

We can assume that  $|X| > v_a \tau + 2R_0 v_a/c$ , i.e., the range delay is such that the reflected radar pulse is entirely in the aperture of the AOD at the instant the laser is pulsed. This can be ensured by appropriately setting the relative phase of the radar and laser pulse repetition frequencies. The parameter  $b_1$  (the focusing power of the optical system in the  $x$  direction) is set equal to  $b/v_a^2$ . Finally, the offset frequency  $v_2 - v_1$  is made to be equal to  $m/T$ , where  $m$  is an integer. This can be accomplished by deriving  $v_1 - v_2$  from the pulse repetition frequency  $1/T$ . The function  $g(\hat{x}, t)$  can then be written as follows:

$$\begin{aligned}
 g(\hat{x}, t) = & \sum_n \text{rect} \left( \frac{t-nT}{\tau_0} \right) \left\{ A(nT) \exp \left[ -j \frac{2\pi v_0}{cR_0} (vnT-\eta_0)^2 \right] \exp \left( -j \frac{b}{v_a^2} \hat{x}^2 \right) \exp \left( j \frac{4bR_0^2}{c^2} \right) \int \text{rect} \left( \frac{x/v_a-2R_0/c}{\tau} \right) \right. \\
 & \times \exp \left[ -j \frac{2b}{v_a^2} (\hat{x}-2R_0 v_a/c) x \right] dx + B \exp [j2\pi(v_2-v_1)\hat{x}/v_a] \exp [j\pi^2(v_2-v_1)^2/b] \Big\} = \sum_n \text{rect} \left( \frac{t-nT}{\tau_0} \right) \\
 & \times \left\{ A(nT) v_a \tau \text{sinc} \left[ \frac{b\tau}{\pi v_a} (\hat{x}-2R_0 v_a/c) \right] \exp \left[ -j \frac{2\pi v_0}{cR_0} (vnT-\eta_0)^2 \right] \exp \left[ -j \frac{2b}{v_a^2} (\hat{x}-2R_0 v_a/c) (2R_0 v_a/c) \right] \right. \\
 & \times \exp \left[ -j \frac{b}{v_a^2} (\hat{x}^2-4R_0^2 v_a^2/c^2) \right] + B \exp [j2\pi(v_1-v_2)\hat{x}/v_a] \exp [j\pi^2(v_2-v_1)^2/b] \Big\} .
 \end{aligned} \quad (A6)$$

We substitute the above expression in Eq. (14):

$$\begin{aligned}
 I(\hat{x}, \hat{y}, nT) = & T(\hat{x}, \hat{y}) \int_{t=nT/2}^{t+nT/2} \sum_n \text{rect} \left( \frac{t-nT}{\tau_0} \right) \left\{ |A(nT)|^2 v_a^2 \tau^2 \text{sinc}^2 \left[ \frac{2b\tau}{v_a} (\hat{x}-2R_0 v_a/c) \right] + |B|^2 + 2B A(nT) v_a \right. \\
 & \times \text{sinc} \left[ \frac{b\tau}{\pi v_a} (\hat{x}-2R_0 v_a/c) \right] \cos \left[ \frac{2\pi(v_2-v_1)\hat{x}}{v_a} + \frac{2\pi v_0}{cR_0} (vnT-\eta_0)^2 + \phi \right] \Big\} dt = 2T(\hat{x}, \hat{y}) B v_a \tau \tau_0 A(nT) \\
 & \times \text{sinc} \left[ \frac{b\tau}{\pi v_a} (\hat{x}-2R_0 v_a/c) \right] \cos [2\pi(v_2-v_1)\hat{x}/v_a + 2\pi v_0(vnT-\eta_0)^2/cR_0 + \phi] + \text{bias terms} .
 \end{aligned} \quad (14)$$

In the above equation, the phase terms from Eq. (A6) that do not depend on the index  $n$  have been lumped in the parameter  $\phi$ .

## 8. APPENDIX B: DERIVATION OF EQUATION (15)

$$Q(\hat{x}, \hat{y}) = \sum_n Q(\hat{x}, \hat{y} - n\Delta y + N\Delta y, nT) \quad (15)$$

Substitute Eq. (14) in the above equation and the expression for the transmittance of the mask from Eq. (12):

$$\begin{aligned} Q(x, y) &= \sum_n 2Bv_a \tau \tau_o \left\{ \frac{1}{2} + \frac{1}{2} \right. \\ &\times \cos \left[ 2\pi u_o \hat{x} - \pi b_2 (\hat{y} - (n-N)\Delta y)^2 / \hat{x} \right] \Big\} \\ &\times A(nT) \operatorname{sinc} \left[ \frac{b\tau}{\pi v_a} (\hat{x} - 2R_o v_a / c) \right] \\ &\times \cos \left[ 2\pi (v_2 - v_1) \hat{x} / v_a + 2\pi v_o (vnT - \eta_o)^2 / cR_o + \phi \right]. \quad (B1) \end{aligned}$$

The spatial frequency  $u_o$  on the mask must be selected so that the sum frequency  $u_o + (v_2 - v_1)/v_a$  of the two cosine functions in the above equation is sufficiently large so that the signal term that is riding on the sum frequency can be separated from the bias terms in the spatial frequency domain. To accomplish this, we set  $u_o = (v_2 - v_1)/v_a$ . We write the product of the cosines as a sum, and the term of interest in Eq. (B1) takes the following form:

$$\begin{aligned} Q(\hat{x}, \hat{y}) &= (Bv_a \tau \tau_o / 2) \operatorname{sinc} \left[ (b\tau / \pi v_a) (\hat{x} - 2R_o v_a / c) \right] \\ &\times \sum_n A(nT) \cos \left[ 4\pi v_o \hat{x} - \pi b_2 \hat{y}^2 / \hat{x} \right. \\ &+ 2\pi b_2 (n-N)\Delta y \hat{y} / \hat{x} - \pi b_2 \Delta y^2 (n-N)^2 / \hat{x} + 2\pi v_o v^2 T^2 n^2 / cR_o \\ &\left. - 4\pi v_o nT \eta_o cR_o + 2\pi v_o \eta_o^2 / cR_o + \phi \right]. \quad (B2) \end{aligned}$$

The focusing of the SAR image in the azimuth direction ( $\eta$ ) is accomplished by the summation over  $n$  in the above equation. The summation will result in a well-focused image in the  $\hat{y}$  direction if the terms containing  $n^2$  in the argument of the cosine are canceled. To accomplish this, the constant  $b_2$  of the mask is set appropriately.

$$\begin{aligned} (2v_o v^2 T^2 / cR_o) n^2 &= (b_2 \Delta y^2 / \hat{x}) n^2 \rightarrow \\ \rightarrow b_2 &= \frac{2v_o v^2 T^2 \hat{x}}{cR_o} = \frac{2v_o v^2 T^2}{cR_o} (2R_o v_a / c) \\ &= \frac{4v_o v^2 T^2 v_a}{c^2 \Delta y^2}. \quad (B3) \end{aligned}$$

Equation (B3) and the value we previously chose for  $u_o$  provide all the information necessary to construct the mask that is used in the system. Equation (B3) is substituted in Eq. (B2), and all inconsequential phase terms are included in the parameter  $\phi$ . Equation (B2) then reduces to the following equation:

$$\begin{aligned} Q(\hat{x}, \hat{y}) &= (Bv_a \tau \tau_o / 2) \operatorname{sinc} \left[ (b\tau / \pi v_a) (\hat{x} - 2R_o v_a / c) \right] \\ &\times \sum_n A(nT) \cos \left[ 4\pi v_o \hat{x} + (4\pi v_o v^2 T^2 / c\Delta y R_o) \right. \\ &\times (\hat{y} - (\eta_o \Delta y / vT) + N\Delta y) n + \phi \Big]. \quad (B4) \end{aligned}$$

The summation over  $n$  in Eq. (B4) is recognized as the discrete cosine transform<sup>12</sup> of the antenna pattern  $A(nT)$ . In order to get an approximate result, we can assume that the antenna pattern is so broad in the azimuth direction that its main lobe uniformly illuminates a distance  $vNT$  on the ground. Therefore,  $A(nT)$  is approximately a constant for  $0 > n > N$ , and Eq. (B4) can be evaluated as follows<sup>13</sup>:

$$\begin{aligned} Q(\hat{x}, \hat{y}) &= (Bv_a \tau \tau_o / 2) \operatorname{sinc} \left[ (b\tau / \pi v_a) (\hat{x} - 2R_o v_a / c) \right] \\ &\times \frac{\sin \left[ (2N\pi v_o v^2 T^2 / c\Delta y R_o) (\hat{y} - (\eta_o \Delta y / vT) + N\Delta y) \right]}{\sin \left[ (2\pi v_o v^2 T^2 / c\Delta y R_o) (\hat{y} - (\eta_o \Delta y / vT) + N\Delta y) \right]} \\ &\times \cos (4\pi v_o \hat{x} + \phi). \quad (B5) \end{aligned}$$

The ratio of the sines in Eq. (B5) can be approximated by a sinc function for large  $N$ , and this leads us to the final form of Eq. (15):

$$\begin{aligned} Q(\hat{x}, \hat{y}) &= (NBv_a \tau \tau_o / 2) \operatorname{sinc} \left[ (b\tau / \pi v_a) (\hat{x} - 2R_o v_a / c) \right] \\ &\times \operatorname{sinc} \left[ (2N\pi v_o v^2 T^2 / c\Delta y R_o) (\hat{y} - (\eta_o \Delta y / vT) + N\Delta y) \right] \\ &\times \cos (4\pi v_o \hat{x} + \phi). \quad (15) \end{aligned}$$

## 9. REFERENCES

1. D. A. Ausherman, *Opt. Eng.* 19(2), 157(1980).
2. T. M. Turpin, *Proc. IEEE* 69(1), 79(1981).
3. W. T. Rhodes, *Proc. IEEE* 69(1), 65(1981).
4. E. N. Leith, *Proc. IEEE* 59(9), 1305(1971).
5. I. Cindrich, J. Marks, and A. Klooster, *Proc. SPIE* 128, 128(1977).
6. A. Korpel, *Proc. IEEE* 69(1), 48(1981).
7. K. Bromley, M. Monahan et al., *Proc. SPIE* 118, 118(1977).
8. M. Blouke et al., *Proc. SPIE* 290, 6(1981).
9. D. Casasent, *Proc. IEEE* 65, 143 (Jan. 1977).
10. J. Hall, in *Applied Optics and Optical Engineering*, Vol. VIII, Chap. 8, Academic Press, New York (1980).
11. D. Psaltis and K. Wagner, *Proc. SPIE* 271, 51(1981).
12. A. W. Rihaczek, *Principles of High Resolution Radar*, McGraw Hill, New York (1969).
13. A. Oppenheim and R. Schaffer, *Digital Signal Processing*, Prentice Hall, Englewood Cliffs, New Jersey (1975).

Synthetic Aperture Radar Imaging Using  
Acousto-Optics And Charge-Coupled Devices

Demetri Psaltis, Kelvin Wagner and Michael Haney  
California Institute of Technology  
Department of Electrical Engineering  
Pasadena, California 91125

**ABSTRACT**

The principles of operation of the Acousto-optic/CCD real-time SAR processor are reviewed and experimental results are presented. The interferometric detection method used in this system is also discussed.

**I. INTRODUCTION**

Synthetic Aperture Radar (SAR) imaging (1,2) is the first problem to which optical computers were successfully applied, initially in the late 50's. The requirements of modern radars such as real-time image formation, better image quality and on-board processing capability, cannot be met by the film based optical SAR processors. We have recently introduced (3,4) a technique for real-time optical SAR processing that utilizes an acousto-optic device (AOD) as the input electronic-to-optical transducer and a CCD image sensor on which the SAR image is formed. The advanced (and continuously improving) state-of-the-art of AOD's and CCD's results in a system that is relatively compact, power efficient, inexpensive and flexible. Therefore, we expect that this processor can be advantageous over digital systems in many of the applications of SAR. In this paper, we present recent experimental results and we discuss the interferometric detection scheme used in the system.

**II. TIME-AND-SPACE INTEGRATING PROCESSING**

SAR is a 2-D signal processing problem because the data collected by the radar is essentially an unfocused image and the processing required in a 2-D linear operation that brings this data into focus. AOD's are used in the processor described in this paper to convert the RF signals to modulated light waves. Since AOD's are 1-D spatial light modulators we will first discuss how 2-D processing can be accomplished with 1-D devices. The approach we have selected is to process the data by spatial integration in one of its dimensions and by temporal integration along the second (5). This is shown in block diagram form in Figure 1.

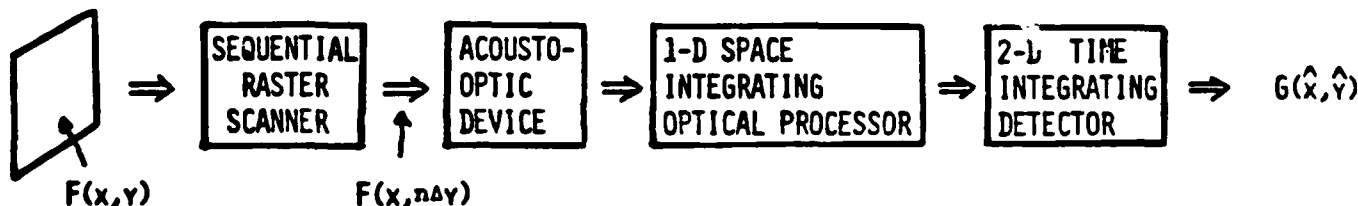


Figure 1. Time-and-Space Integrating Processor of 2-D Signals  
Let:  $f(x, y)$  be an arbitrary 2-D function to which we wish to apply a linear operator characterized by the impulse response  $h$ . The processed data  $g(\hat{x}, \hat{y})$  is in the form

$$g(\hat{x}, \hat{y}) = \iint f(x, y) h(x, \hat{x}, y, \hat{y}) dx dy. \quad (1)$$

To compute  $g$ , the function  $f(x, y)$  is first sampled in the  $y$  dimension. If  $f(x, y)$  is an image, a raster scanning TV camera can be used to perform the sampling. In SAR, the data is already sampled by the pulsed radar waveform. The sampled data can be thought of as an ensemble of  $N$  one dimensional signals,  $f(x, n\Delta y)$ , where  $N$  is the number of samples in the  $y$  direction and  $\Delta y$  is the sampling period. Each of the 1-D signals is sequentially entered into the optical system through the AOD and processed by spatial integration. At the time the  $n$ th line is at the input plane of the optical system, the light at the output is modulated by

$$g_n(\hat{x}, \hat{y}) = \int f(x, n\Delta y) h(x, \hat{x}, n\Delta y, \hat{y}) dx, \quad (2)$$



where  $h$  is the spatial impulse response of the optical system and  $(x, y)$  are the output co-ordinates.  $g(x, y)$  is detected and stored on a 2-D CCD array. The different lines of data are sequentially entered in the system and the corresponding responses accumulated on the time integrating CCD. The charge accumulated on the CCD after all  $N$  lines of data have been processed is proportional to

$$g(x, y) = \sum_{n=1}^N \int f(x, n\Delta y) h(x, x, n\Delta y, y) dx. \quad (3)$$

Eq. (3) is essentially identical to Eq. (1) with the continuous variable  $y$  replaced by  $n\Delta y$  and the integration over  $y$  replaced by the summation over  $n$ . The final issue that has to be addressed is whether an optical system can be implemented with an impulse response  $h(x, x, n\Delta y, y)$ . This impulse response corresponds to the most general 2-D linear operation (Eq. 1). It is a function of three spatial variables and it must be updated for each  $n$  (each line of input-data). It is not in general feasible to implement an optical system with a controllable impulse response in this form. It is however, possible to do so, for two very important special forms of the function  $h$ : a) if  $h$  is shift invariant ( $h(x, x, n\Delta y, y) = h(x+x, y+n\Delta y)$ ), 2-D convolution/correlation can be implemented. (6) b) if  $h$  is separable in  $x$  and  $y$  ( $h(x, x, n\Delta y, y) = h_1(x, x) h_2(n\Delta y, y)$ ), operations such as the 2-D Fourier Transform can be performed<sup>(5)</sup>. The signal processing required for SAR image formation is also a 2-D linear operation with a separable kernel and therefore the time-and-space integrating processing method is applicable to this problem.

### III. SAR

The geometry of the side-looking radar is shown in Figure 2. The vehicle that collects the SAR data is flying with constant velocity in the direction  $x$  parallel to the ground. Coded pulses are transmitted by the antenna mounted on the vehicle and a portion of the ground is illuminated. The reflections from the ground are detected at the vehicle. The position of each point reflector on the ground in the  $y$ -direction (range) in Figure 2 is estimated by measuring the round-trip delay of the radar pulses. The position of each target in the  $x$ -direction

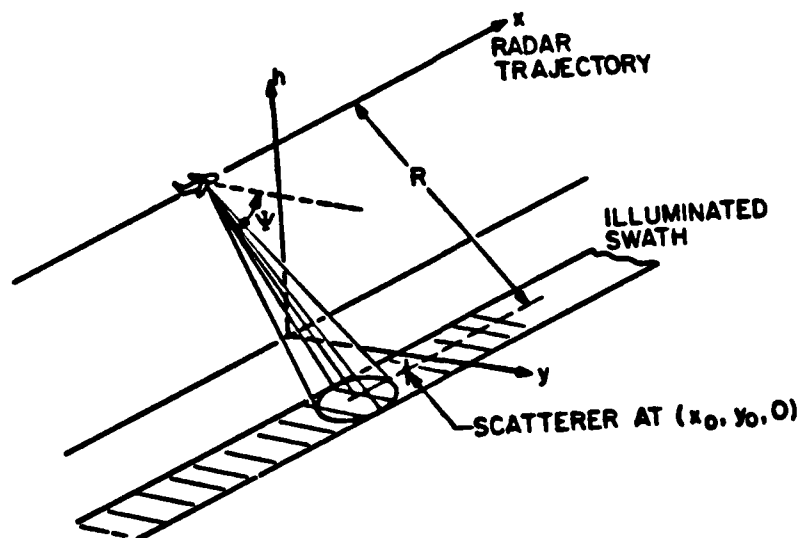


Figure 2. SAR Geometry

(azimuth) is determined by measuring the Doppler frequency shift of consecutive radar pulses. As the vehicle approaches a stationary point reflector the relative velocity component results in a blue Doppler shift on the reflected pulses. When the vehicle crosses over the reflector there is no relative velocity component and no frequency shift and when the vehicle flies away from a red Doppler shift results. The signal processor estimates the range and Doppler parameters of the reflected signals for all points on the ground simultaneously, to form a complete SAR image. The reflected radar signals in SAR are normally thought of as a 2-D data set. The first dimension,  $\eta$ , is formed by the time history of each reflected pulse and the second dimension,  $\xi$ , is formed by the consecutive

radar pulses. It can be shown (2) that the signal reflected from a single point reflector located at co-ordinates  $(x=x_0, y=y_0)$  on the ground, arranged in the 2-D format is given by:

$$f(\xi, \eta) = e^{jk_1 (\xi-x_0)^2/y_0 + jk_2 (\eta-y_0)^2} \quad (4)$$

where  $k_1$  and  $k_2$  are constants determined by the parameters of the radar and we have assumed that the transmitted pulses are linear frequency modulated (LFM). If the function in Eq. (4) is recorded as a 2-D optical transparency, an asymmetric zone plate is formed. The image of the point reflector on the ground is formed by focusing this zone plate. The focusing operation is described mathematically by the following 2-D integral:

$$\begin{aligned} g(x, y) &= \int_{\Lambda_1} \int_{\Lambda_2} f(\xi, \eta) e^{-jk_1 (\xi+x)^2/y} e^{-jk_2 (\eta+y)^2} d\xi d\eta \\ &= e^{jk_1 (x_0^2 - x^2)/y_0} e^{jk_2 (y_0^2 - y^2)} \\ &\quad \int_{\Lambda_1} \int_{\Lambda_2} e^{-j2k_1 \xi(x-x_0)/y_0} e^{-j2k_2 \eta(y-y_0)} d\xi d\eta \\ &= e^{jk_1 (x_0^2 - x^2) + jk_2 (y_0^2 - y^2)} \operatorname{sinc} \left[ \frac{k_1 (x-x_0)}{\pi y_0 \Lambda_1} \right] \operatorname{sinc} \left[ \frac{k_2 (y-y_0)}{\pi \Lambda_2} \right]. \end{aligned} \quad (5)$$

$\Lambda_1$  is the interval of integration in the azimuth ( $\xi$ ) dimension and it is proportional to the number of radar pulses that are integrated to form the SAR image.  $\Lambda_2$  is the interval of integration in the range ( $\eta$ ) dimension and it is determined by the duration of the transmitted coded pulses. Eq. (5) demonstrates that the image  $g(x, y)$  for a single point target is a focused spot centered at the co-ordinates  $(x_0, y_0)$ . Since the operations involved are linear, the entire image is formed for an arbitrary ground reflectivity. The signal processing required is described by Eq. (5), and it is important to notice that the kernel of this operation is separable in  $\eta$  and  $\xi$ . We rewrite Eq. (5) in order to emphasize this point.

$$\begin{aligned} g(x, y) &= \int_{\Lambda_1} \left[ \int_{\Lambda_2} f(\xi, \eta) e^{-jk_2 (\eta+y)^2} d\eta \right] e^{-jk_1 (\xi+x)^2/y} d\xi \\ &= \int_{\Lambda_1} h(\xi, y) e^{-jk_1 (\xi+x)^2/y} d\xi. \end{aligned} \quad (6)$$

This separability allows us to process the radar data  $f(\xi, \eta)$  first along the range ( $\eta$ ) dimension for each value of the parameter  $\xi$ . Since  $\xi$  corresponds to different radar pulses, the reflection received for each transmitted pulse is processed in  $\eta$  (the time history of each return) to focus the SAR image in range. The range focused image is then processed across the consecutive pulse returns ( $\xi$ ) to produce the final image. The required processing operation in  $\xi$ , depends on  $y$  and therefore a different processing operation must be performed for each position in range. For real-time image formation, an array of parallel processors is needed in the azimuth direction, one for each range resolution cell.

We present the range processor in the following section and the azimuth processor in section V. The interferometric detection that is necessary to integrate the two processors into a complete SAR imager is discussed in section VI.

#### IV. RANGE PROCESSOR

A schematic diagram of the range processor is shown in Figure 3. Recognizing the fact that the  $\xi$  dimension is sampled by the pulsed radar waveform, we replace  $\xi$  with the discrete variable  $n\Delta\xi$ , where  $n$  is an integer and  $\Delta\xi$  is proportional to the pulse repetition period of the radar. The received signal  $f(n\Delta\xi, \eta)$  is applied to the AOD and the system is illuminated with a pulsed light source. The PRF of the light source is equal to the PRF of the radar. The timing of the light pulses is set such that they occur at the instant the acoustic signal in the AOD

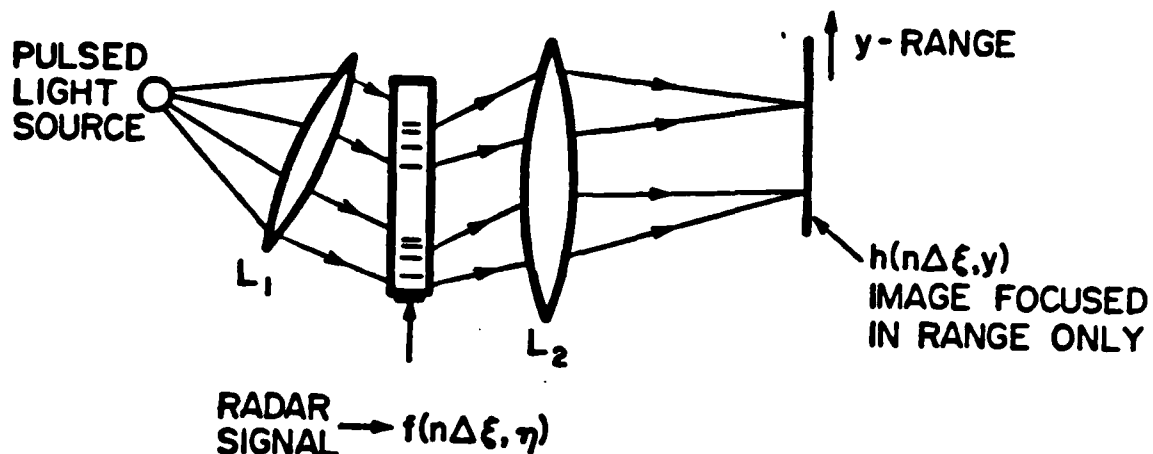


Figure 3. Range Processor

corresponds to the reflected signal for each radar pulse that is transmitted. This acoustic signal in the AOD consists of a multitude of spatially misaligned LFM signals. Each LFM causes a portion of the incident light beam to be diffracted into a diverging spherical wave that is focused by lens  $L_2$  in Figure 3. The position in the  $y$ -dimension at which the light from each LFM is focused at the output plane, is proportional to the position of the LFM in the AOD at the instant the light source is pulsed. This position is in turn proportional to the range of each target on the ground; reflection from targets relatively close to the radar are received earlier and propagate relatively farther in the AOD at the instant the light source is pulsed. The focusing action of the lens is described mathematically by the integral over  $\eta$  in Eq. (6) and the output of the processor in Figure 3 is the SAR image focused in range only.

The range processor described above has been assembled and tested. The experimental set-up is shown in Figure 4a. A pulsed laser diode, operating at 830 nm wavelength, .5 watts peak power and pulse width 50 nsec was the light source in this experiment. A spherical lens was used to collimate the light from the laser diode. The AOD shown in Figure 4a has 40 MHz bandwidth and 10  $\mu$ sec aperture. Cylindrical optics were used to match the shape of the light beam to the aperture of the AOD. The signal applied to the AOD is shown in Figure (4b). The consecutive LFM signals were generated by a Surface-Acoustic wave device at a 10 KHz PRF. The duration of each LFM was 6  $\mu$ sec and the bandwidth 20 MHz for display purposes. The laser diode was pulsed at the same PRF, delayed by approximately 15  $\mu$ sec, to allow the signal to propagate through the SAW and the AOD. The light diffracted by the AOD was brought into focus with a 381 mm focal length spherical lens. The diffracted beams were converging in this experiment and the focal plane was found approximately 360 mm after the spherical lens. The collimated undiffracted light was spatially separated from the signal beam at this point and the signal was detected by a linear detection array. Thirty light pulses were integrated on the array before it was read-out. The signal from the detector is displayed in Figure 4c and it shows the two LFM signals compressed and therefore the SAR image brought into a sharp focus in range.

# V. AZIMUTH PROCESSOR

The range focused image must be processed in the  $\xi$  dimension (over many radar pulses) to produce an image focused in both dimensions. An electro-optic processor (8,9) that utilizes a 2-D CCD detector is used for this purpose. A schematic diagram of the azimuth processor is shown in Figure 5. The light distribution at the input plane  $P_1$  is the same light that appears at the output of the range processor of Figure 3.

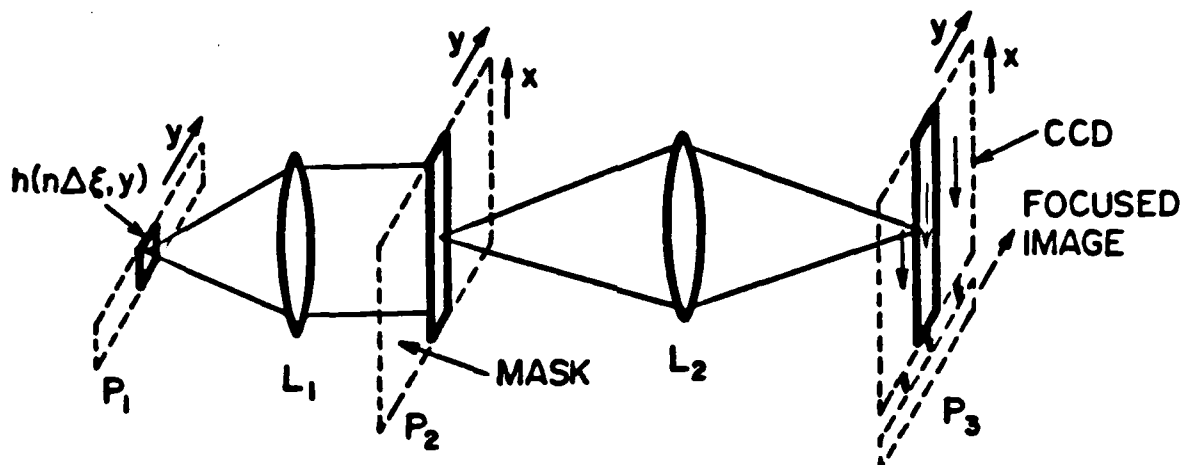


Figure 5. Azimuth Processor

Let  $h(n\Delta\xi, y)$  denote the light amplitude at  $P_1$  at the range position  $y$  during the  $n$ th radar pulse. The light from  $P_1$  is collimated in the vertical ( $x$ ) direction and imaged in  $y$  onto plane  $P_2$ . A mask is placed at plane  $P_2$  with amplitude transmittance

$$t_M(x, y) = e^{-jk_1 x^2 / y} \quad (7)$$

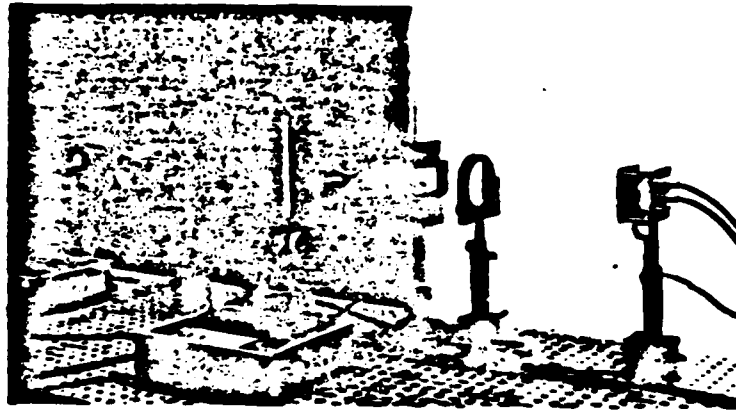
This is the kernel function in the azimuth ( $\xi$ ) direction from Eq. (6). The complex transmittance function is implemented by writing the data on a spatial carrier. The light immediately after the mask is modulated by the product  $h(n\Delta\xi, y) t_M(x, y)$ . Plane  $P_2$  is imaged in both dimensions onto plane  $P_3$ , where the 2-D CCD array is placed. The light incident on the CCD is interferometrically detected. The entire charge pattern stored on the array is shifted by one pixel in the  $x$ -direction after each light pulse. In other words, the CCD vertical transfer rate is also equal to the radar PRF. The photogenerated charge due to consecutive light pulses continues to accumulate on the travelling charge-pattern in the CCD. The relative motion between the charge on the CCD and the fixed mask provides the mechanism by which the correlation between the input  $h(n\Delta\xi, y)$  and  $e^{-jk_2 x^2 / y}$  (the transmittance of the mask) is computed at each range position  $y$ . The charge accumulated on the CCD after  $N$  radar (and light) pulses is given by (4)

$$\sum_{n=1}^N h(n\Delta\xi, y) e^{-jk_2 (x+n\Delta\xi-N\Delta\xi)^2 / y} = g(x-N\Delta\xi, y). \quad (8)$$

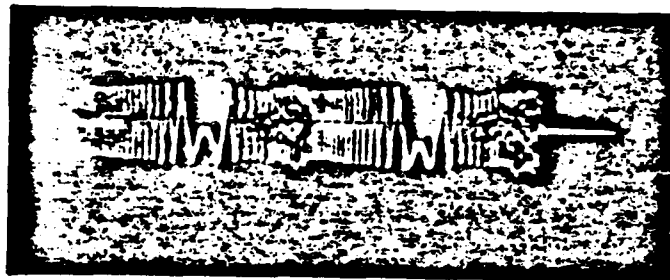
We recognize by inspection of Eq. (6), that Eq. (8) is the focused SAR image shifted in the  $x$  direction by  $N\Delta\xi$ . The number,  $N$ , of pulses that are integrated to form the SAR image is equal to the number of pixels of the CCD in the  $x$  direction. Therefore, the shift in  $x$  by  $N$  pixels reveals the fact that the lines of the focused SAR image form sequentially at the bottom row of the array, where they are transferred to the output shift-register and read-out. The lines of the image (slices along the range dimension) are continuously produced at a rate equal to the PRF of the radar.

A photograph of the experimental azimuth processor is shown in Figure 6. A light emitting diode (LED) was used as the source in this experiment. The LED was temporally modulated with a slow varying LFM

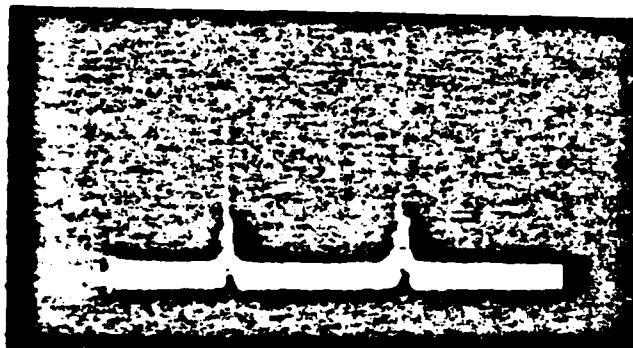
352-16



(a)



(b)



(c)

Figure 4. a) Experimental Range Processor b) Input LFM Signals  
c) Focused LFM Signals.

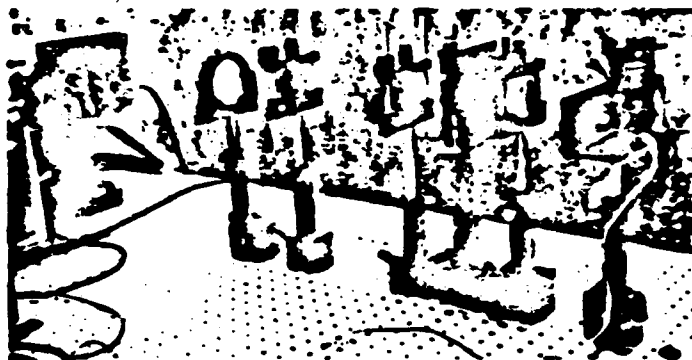


Figure 6. Experimental Azimuth Processor

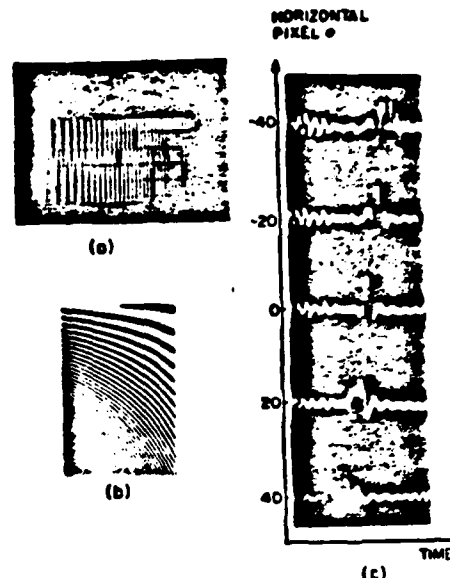


Figure 7. a) Input LFM Waveform b) Mask c) Ambiguity Function

signal to stimulate the variation of  $f(\xi, \eta)$  in  $\xi$  (see Eq. (4)). The bandwidth of this signal (corresponding to the Doppler bandwidth) was 30 Hz and its duration 1 second. This waveform is shown in Figure 7a. The light from the LED was collimated by lens  $L_1$  in Figure 6 and it illuminated the mask shown in Figure 7b and marked M in Figure 6. The mask was imaged by lens  $L_2$  onto the CCD. The CCD is a buried channel device with 512 pixels in the vertical (shifting) direction and 320 in the horizontal. The CCD was clocked horizontally at .5KHz. Therefore each charge packet that reached the output stage at the bottom of the device had accumulated charge for  $(512) \times 2 \text{ msec} = 1.024$  seconds, which was approximately equal to the duration of the input LFM signal. The transmittance of the mask in Figure 7b is a LFM signal in the vertical direction and the FM rate varies along the y direction. The signal clocked out from each column of the CCD in the correlation of the temporal signal that modulates the LED and the transmittance of the mask in the vertical direction. The output of the CCD at selected horizontal pixel locations is shown in Figure 7c. A match between the input waveform and the transmittance of the mask was obtained at the middle of the array (pixel #0) where we obtain the autocorrelation of the LFM. The signals at other locations are the cross-correlation of the LFM with scaled versions of itself. The entire 2-D waveform is known as the ambiguity surface (10) and the familiar tilted ridge structure of the ambiguity function of the LFM is evident in Figure 7c.

## VI. INTERFEROMETRIC DETECTION

The overall SAR processor is synthesized by interfacing the range and azimuth processors. This interface however must be coherent because the information needed to focus the SAR image in azimuth, is encoded in the phase of the range compressed signals (the Doppler frequency shift). Therefore the phase of the light must be recorded on the CCD as well as the amplitude. This can only be accomplished by introducing a reference beam so that the phase can be recorded on the interference pattern. Interferometric detection will in general decrease the dynamic range and the available space-bandwidth product and it imposes stricter requirements for mechanical stability and coherence of the source. In this section we describe the interferometric detection scheme we use in the SAR processor that minimizes most of these problems and we report experimental results of interferometric detection with pulsed laser diodes.

352-16

The interferometric system is shown in Figure 8. It is similar to the range processor shown in Figure 5. In this case however, the radar signal after it is mixed to the center frequency  $\omega_1$  of the AOD it is added to a reference sinusoid at a frequency  $\omega_2$ . The

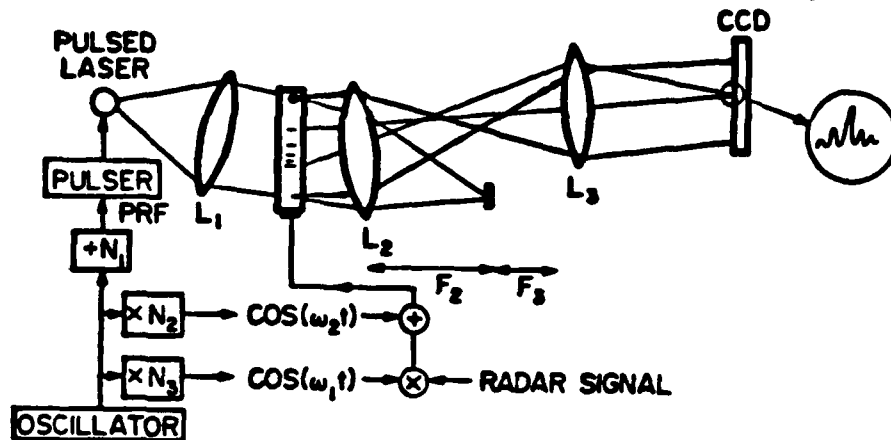


Figure 8. Range Processor including interferometric detection.

difference frequency  $(\omega_2 - \omega_1)/2\pi$  is chosen to be equal to the bandwidth of the radar waveform. The combined waveform is applied to the AOD and a pulsed light source is used as before. The light diffracted by the AOD consists of two separate waves: a converging wave due to the LFM radar signal and a collimated beam due to the reference signal at  $\omega_2$ . Lenses  $L_2$  and  $L_3$  are separated by the sum of their focal lengths. This arrangement collimates the plane wave reference after  $L_3$  and it images the focal plane of the LFM signal onto the CCD. The temporal frequency offset between the signal and the reference results in an angular offset between the focusing signal and the collimated reference that are co-incident on the CCD. The interference pattern is recorded on a spatial carrier and it can be separated from the bias terms by filtering. This frequency offset however, also introduces different Doppler frequency shifts on the two diffracted beams, which can wash out the fringes when many pulses are integrated on the detector (4). This is avoided by locking the difference frequency  $|\omega_1 - \omega_2|/2\pi$  to the PRF of the laser diode. We show some of the interferometrically detected signals using this method, in Figure 9. The optical system shown in Figure 8 was assembled and a LFM test signal with 20 MHz bandwidth was applied as the

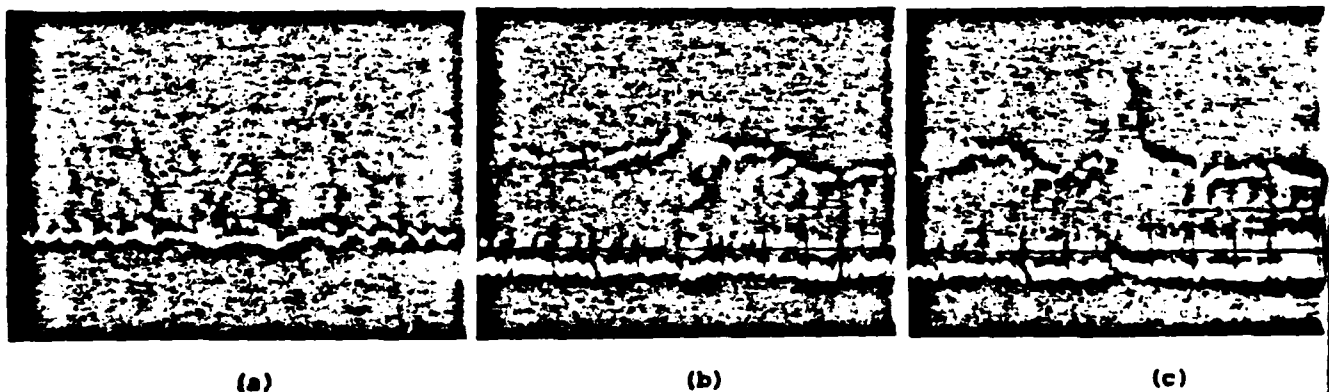


Figure 9. Interferometrically detected waveforms using a pulsed laser diode source.

radar signal. The reference signal was equal to the center frequency of the LFM when the photographs shown in Fig. 9 were taken. Figure 9a shows the interference pattern at the image plane of the AOD where the diffracted LFM wave (a purely phase modulated optical beam) is interfered with the reference beam. The LFM is reconstructed at baseband. Figure 9b shows the interference of the focused LFM and the reference beam. In this instance, destructive interference is observed. When a phase delay  $180^\circ$  is introduced electronically in the reference beam, the interference becomes constructive. (Fig. 9c).

These results are very encouraging since the pulsed laser diode used in this experiment (pulse width = 50 nsec, PRF = 10 KHz) is designed for a high peak power (1.5 watts) and consecutively it has a very short coherence length. Our ability to obtain strong interference away from the image plane, demonstrates that the introduction of the reference beam through the same Bragg cell as the signal beam, minimizes the coherence requirements because the optical paths of the two beams are equalized very effectively.

#### ACKNOWLEDGEMENTS

We thank Mr. Tom Bicknell for his support and assistance. The research reported in this paper is funded by NASA and the Air Force Office of Scientific Research.

#### REFERENCES

- 1) E. Leith, Proc. IEEE, Vol. 59, p. 1305, Sep. 1971.
- 2) I. Cindrich, et. al., Proceeding of SPIE, Vol. 128, p. 128, Sep. 1977.
- 3) D. Psaltis and K. Wagner, Proc. SPIE, Vol. 271, Feb. 1981.
- 4) D. Psaltis and K. Wagner, Optical Engineering, Sep. 1982.
- 5) D. Psaltis, JOSA, Vol. 71, p. 198, Feb. 1981.
- 6) D. Psaltis, Appl. Optics, Vol. 21, p. 491, Feb. 1982.
- 7) D. Psaltis, Proc. EO/SD Conf., Nov. 1981, Anaheim, California.
- 8) K. Bromley, M. M. Monahan, et al, Proc. SPIE, Vol. 118, 1977.
- 9) M. Copeland, et. al, IEEE Trans. Electron Devices, Vol. ED-23, p. 152, Feb. 1976
- 10) A. Rihaczek, "Principles of High Resolution Radar", McGraw Hill, NY 1969.



## Appendix Ve

## IMAGE PROCESSING USING ACOUSTO-OPTICS

by

Demetri Psaltis  
California Institute of Technology  
Pasadena, California 91125

ABSTRACT

An optical processing technique is presented that allows the processing of images using an acousto-optic device as the input light modulator.

I. INTRODUCTION

Image Processing is one of the most promising applications for optical computers because the multidimensional processing space and the parallelism of the optical system can be very effectively utilized to represent and perform computations on images. The practical realization of optical image processing systems however, has been impeded by the slow development of real-time 2-D spatial light modulators (SLM). Such devices are used in a conventional optical image processor, to create at high speed a transparency corresponding to an input image. In a coherent optical computer good optical quality of the SLM is essential as well as speed and resolution. A number of 2-D SLM's have been under development for several years [1], but none of these devices have yet reached a mature state of development that would allow its routine use in image processing systems. In this paper we consider the implementation of optical image processors using an Acousto-Optic Device (AOD) as the input SLM. AOD's are excellent light modulators and are commonly used to optically process 1-D signals [2]. The relative disadvantage of AOD's is that they can only produce light modulation along one spatial dimension. Thus, if an AOD is to be used as the input transducer to an image processing system, we must find ways to represent 2-D functions through a 1-D device and design optical processor architectures that can process the images as they are represented by the AOD.

In Section II, we discuss the general concepts relating to the representation and processing of images using AOD's. In Section III, we describe the implementation of 2-D linear, shift invariant operations and in Section IV, we discuss the implementation of 2-D linear operations with separable kernels.

II. GENERAL CONCEPTS

Optical image processing systems typically perform linear operations on the input image  $f(\alpha, \beta)$  which can be described by a superposition integral:

$$g(\xi, \eta) = \iint f(\alpha, \beta) h(\alpha, \beta, \xi, \eta) d\alpha d\beta, \quad (1)$$

where  $h$  is the impulse response of the linear operation and  $g(\xi, \eta)$  is the processed image. We will address two related issues: a) how will the function  $f(\alpha, \beta)$  be entered in the optical system through the AOD, and b) what is the optical system architecture that can implement Equation (1).

A schematic diagram of an AOD is shown in Figure 1. The device consists of a piezoelectric transducer bonded onto the acousto-optic crystal. An electronic signal applied to the piezoelectric transducer induces an acoustic wave which propagates along the x-direction in the crystal with acoustic velocity  $v$ . When the device is illuminated with a collimated light beam, a portion of the incident light is diffracted due to the acousto-optic interaction. The amplitude of the light diffracted in the first order is modulated by  $\text{rect}(\frac{x}{A}) s(t + \frac{x}{v})$ , where  $s(t)$  is the electronic signal applied to the device and  $A$  is the aperture of the device. In other words, at any instant in time  $t$ , the amplitude of the diffracted light is spatially modulated by the signal  $s(t)$  for  $t < t + \frac{A}{v}$ . The space-bandwidth product of the device is  $N = \frac{A}{\lambda} B$  where  $B$  is the temporal bandwidth. For a typical AOD,  $N$  is  $10^3 - 10^4$ . For the majority of image processing applications, the input image has a space-bandwidth product of  $(500)^2$  or more. Thus, an AOD can only represent approximately one line

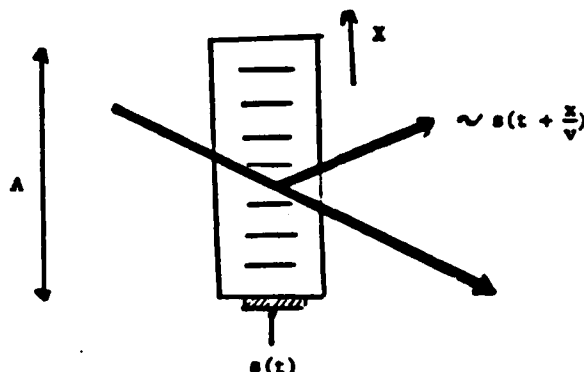


Figure 1. Acousto-optic Spatial Light Modulator

of an input image  $f(\alpha, \beta)$  at one time. Since the AOD must be addressed electronically, the image  $f(\alpha, \beta)$  is converted to an electronic signal by a scanning sensor, such as a TV camera. The raster scanned signal  $s(t)$ , is related to  $f(\alpha, \beta)$  by the following relation:

$$s(t) = \sum_{n=1}^N f[v_s(t-nT), n\Delta y] \quad (2)$$

where  $v_s$  is the scanning velocity of the TV camera in the  $\alpha$  direction,  $\Delta y$  is the resolution of  $f(\alpha, \beta)$  in the  $\beta$  direction,  $T$  is the duration of each raster line ( $Tv_s$  is the size of the image in the  $\alpha$  direction),  $n$  is an integer and  $N$  is the total number of raster lines in the  $\beta$  direction ( $N\Delta y$  is the size of  $f(\alpha, \beta)$  in the  $\beta$  direction).

If an AOD is driven by the signal in Equation (2) the diffracted light is modulated proportionally to

$$s(t + \frac{x}{v}) = \sum_{n=1}^N f[v_s(t + \frac{x}{v} - nT), n\Delta y] \text{rect}(\frac{x}{A}). \quad (3)$$

The light source illuminating the AOD is pulsed at time instances  $t-nT$ . If the light pulse is made shorter than the inverse of the bandwidth of  $s(t)$ , at time  $t-nT$  the diffracted light is modulated by

$$s(nT + \frac{x}{v}) = f(x, n\Delta y) \quad (4)$$

In Equation (4) we assume  $v_s = v$  for simplicity and  $Tv_s = A$ . From Equation (4) we conclude that at each instant  $t-nT$  the AOD spatially modulates the light with the  $n$ th raster line of  $f(\alpha, \beta)$  and the different lines are entered consecutively in time. For a fixed position  $x=x_0$  in Equation (4), the light is temporally modulated by the function  $f(x_0, \beta)$ , sampled in  $\beta$ . In essence, one of the dimensions of  $f(\alpha, \beta)$  is represented in one spatial coordinate of the optical system and the second in time. The representation of  $f(\alpha, \beta)$  by the AOD, suggests that a combination of spatial and temporal integration must be used in any optical processor that would process an image represented in this manner [3].

If the sampling in the  $\beta$  direction is done at the Nyquist rate, we can rewrite the expression of a general 2-D linear operation (Equation (1)) in terms of the signal in Equation (4).

$$g(\xi, \eta) = \sum_{n=1}^N \int f(x, n\Delta y) h(x, n\Delta y, \xi, \eta) dx \quad (5)$$

Since the index  $n$  in Equation (4) represents different instances in time, the summation over  $n$  in Equation (5) can be implemented in an optical processor by time integration on a detector. Therefore, we turn our attention to the optical implementation of the integral in  $x$  in Equation (5).

For each value of  $n$ , this integral represents a linear system, with a one-dimensional input function and a three-dimensional impulse response. The optical implementation of such a system is in general difficult, because three independent dimensions are required and we only have two spatial dimensions to work with. However, the implementation is possible for several forms of the function  $h(\alpha, \beta, \xi, \eta)$ . Specifically if  $h$  is shift invariant (i.e.,  $h(\alpha, \beta, \xi, \eta) = h(\xi - \alpha, \eta - \beta)$ ) or separable in  $\alpha$  and  $\beta$ , (i.e.,  $h(\alpha, \beta, \xi, \eta) = h_1(\alpha, \xi) \cdot h_2(\beta, \eta)$ ) it is possible to configure optical processor architectures that can implement Equation (5). These two cases are very significant because in practice the majority of the linear operations that are commonly performed on imagery, are indeed shift invariant or separable. In the following sections we describe the implementation of acousto-optic systems that perform image correlation and Fourier transformations.

### III. SHIFT INVARIANT OPERATIONS

For a shift invariant system, Equation (5) can be rewritten as follows.

$$g(\xi, n) = \sum_{n=1}^N \int f(x, n\Delta y) h(\xi - x, \eta - n\Delta y) dx$$

$$= \sum_{n=1}^N \int [f(x, n\Delta y) h(\xi - x, \eta)] \delta(\eta - \eta + n\Delta y) d\eta, \quad (6)$$

where  $\delta(\ )$  is the impulse function.

For each value of the integer  $n$ , the term in the brackets in Equation (6) is the 1-D convolution of  $f(x, n\Delta y)$  with  $h(x, \eta)$  for all values of the independent variable  $\eta$ .

An optical implementation of such a multichannel 1-D convolver is shown in Figure 2. The light in plane  $P_1$  is modulated by an AOD along the  $x$ -direction by  $f(x, n\Delta y)$ . The light is collimated in the direction orthogonal to  $x$  by lens  $L_1$  and Fourier transformed by  $L_2$  along the  $x$ -direction. The amplitude of the light illuminating plane  $P_2$  is uniform in the  $\eta$  direction and is modulated by the Fourier transform of  $f(x, n\Delta y)$  in the horizontal direction. The filter function  $h(x, \eta)$  is Fourier transformed along  $x$  only and a hologram of this transform is formed. The hologram is placed in  $P_1$ . The light at each position  $\eta = \eta_0$  immediately following the hologram is modulated by the product of the transforms of  $h(x, \eta_0)$  and  $f(x, n\Delta y)$ . The cylindrical lens  $L_4$  retransforms this product in the  $x$ -direction and lens  $L_3$  images plane  $P_2$  onto plane  $P_3$  in the  $\eta$  direction. The light is detected interferometrically by a 2-D detector at the output plane  $P_3$ . At each location  $\eta_0$  in  $P_3$  the detected signal is modulated in the  $x$ -direction by the convolution of the function  $f(x, n\Delta y)$  and  $h(x, \eta_0)$ . In other words, the light distribution at the output plane  $P_2$  is the term in the brackets in Equation (6). According to Equation (6) this function must be shifted in the  $\eta$  direction by  $n\Delta y$  and the summation over  $n$  performed to obtain the output  $g(\xi, n)$ . The vertical coordinate on the detector is denoted by  $\eta$  to distinguish it from the coordinate in the same plane associated with the optical system. If  $\eta = \eta - n\Delta y$  then the detected signal when written in detector coordinates is in the desired form and the summation over  $n$  can be simply accomplished by letting the signals for different  $n$  accumulate on the time integrating detector. We therefore focus on the interpretation of the condition  $\eta = \eta - n\Delta y$ . For  $n=0$  no data has entered the system yet and  $\eta = \eta$ , i.e., the coordinate of the optical system and the detector coordinates coincide. For  $n=1$ ,  $\eta = \eta - \Delta y$  which means that after the first line of data,  $f(x, \Delta y)$  has entered the system and the output is detected, the detector must be shifted in the  $\eta$  direction by one pixel. In general, after each line enters the system and is processed, the detector is moved relative to the optical system by one pixel. In practice, this relative motion can be achieved by mechanically moving either the hologram or the detector relative to each other or by using an optical scanner at some point between the hologram and detector planes. Most conveniently however, a CCD camera can be used as the detector. In a CCD the photogenerated charge that is stored in each pixel can be shifted to an adjacent pixel by applying an electrical waveform to the device [4]. This mechanism is normally used in a CCD camera to read-out the detected image as a video signal. In our system, the charge transfer mechanism of the device can be utilized to implement the shifting of the detector

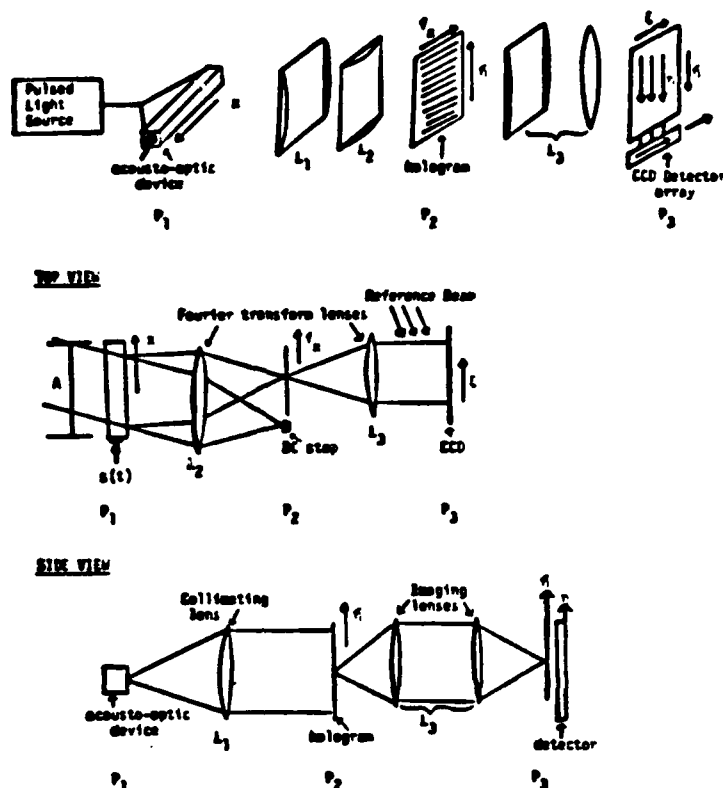


Figure 2. Acousto-optic Image Correlator

coordinates relative to the rest of the system in a very convenient and efficient manner.

#### IV. SEPARABLE KERNEL OPERATIONS

If the function  $h$  is of the form  $h(\alpha, \beta, \xi, \eta) = h_1(\alpha, \xi) h_2(\beta, \eta)$  then Equation (5) can be written as follows:

$$g(\xi, \eta) = \sum_{n=1}^N [f(x, n\Delta y) h_1(x, \xi) dx] h_2(n\Delta y, \eta) \quad (7)$$

In this case, the 2-D processing operation reduces to a cascade of two 1-D operations, one along each dimension of the input image. The optical architecture that implements Equation (7) is a 1-D space-integrating processor operating on the light which the AOD spatially modulates by the  $n$ th line of  $f(\alpha, \beta)$ , followed by a time integrating processor, which operates in the orthogonal dimension. This can be accomplished for arbitrary functions  $h_1$  and  $h_2$ . In other words, 2-D space variant operations can be implemented with this technique if the kernel is separable. For instance, a 2-D Mellin transform which is useful for scale invariant image recognition, can be calculated in real time. There is a variety of optical architectures with which Equation (7) can be implemented [5]. We will present the specific example of a particular implementation of the 2-D Fourier transform in order to exemplify the signal processing method. The 2-D Fourier transform of  $f(\alpha, \beta)$  is given by

$$g(\xi, \eta) = \iint f(\alpha, \beta) e^{-j2\pi\alpha\xi} e^{-j2\pi\beta\eta} d\alpha d\beta, \quad (8)$$

and in the sampled form of Equation (7),

$$g(\xi, \eta) = \sum_{n=-N}^N [f(x, n\Delta y) e^{-j2\pi x\xi} e^{-j2\pi n\Delta y\eta}] \quad (9)$$

The optical architecture that can implement Equation (9) is shown in Figure 3. The raster

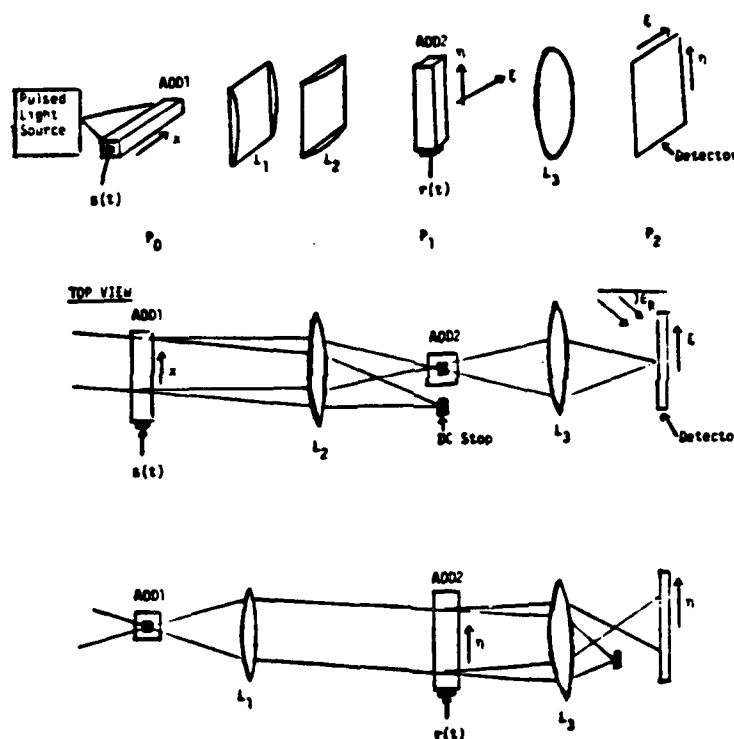


Figure 3. Acousto-optic Image Fourier Transforming System

scanned signal corresponding to the input image is applied to AOD1. The system is illuminated with a pulsed light source as we described in the previous section. During the  $n$ th light pulse, the light diffracted by AOD1 is  $f(x, n\Delta y)$ . The cylindrical lens  $L_1$  collimates the light in the direction orthogonal to  $x$  and  $L_2$  forms the Fourier transform of  $f(x, n\Delta y)$  in the  $x$ -direction and displays it at plane  $P_1$ . A second AOD is placed at  $P_1$ . The acoustic wave propagates in the direction orthogonal to  $x$ , denoted by  $\eta$  in Figure 3. The signal  $r(t)$  is applied to AOD2, where

$$r(t) = \sum_{n=-N}^N \cos[(\omega_0 + n\Delta\omega)t] \text{rect}\left(\frac{t-nT}{T}\right) \quad (10)$$

Where  $\omega_0$  is the center frequency of AOD2 and  $\Delta\omega$  is a fixed frequency increment. The amplitude

of the light diffracted by AOD2 is modulated by

$$\sum_{n=1}^N \text{rect}\left(\frac{t+\eta/v-nT}{T}\right) e^{j(\omega_0+n\Delta\omega)(t+\eta/v)} \quad (11)$$

At times  $t=nT$  and assuming the aperture of AOD2 is equal to  $A=vT$  the modulation is

$$\text{rect}\left(\frac{t-nT}{T}\right) e^{jn\Delta\omega t} e^{\frac{jn\Delta\omega\eta}{v}} e^{j\omega_0 t} \quad (12)$$

where  $T$  is the width of the light pulse and we assume  $T \ll \frac{2\pi}{\Delta\omega}$ . We also set  $T = \frac{2\pi}{\Delta\omega}$ . The light after AOD2 is modulated by the product of the Fourier transform of  $f(x, n\Delta y)$  and Equation (12):

$$\text{rect}\left(\frac{t-nT}{T}\right) e^{j\frac{2\pi n\eta}{A}} F_x(\xi, n) e^{j\omega_0 t} \quad (13)$$

where  $F_x(\xi, n) = \int f(x, n\Delta y) e^{-j2\pi\xi x} dx$ .

Plane  $P_1$  is imaged onto the output plane  $P_2$  by the spherical lens  $L_3$ . A reference plane wave is also made incident on plane  $P_2$ . The amplitude of the reference beam is modulated by

$$R(\xi, t) = e^{j\frac{2\pi\sin\theta_R \xi}{\lambda}} e^{j\omega_0 t} \quad (14)$$

where  $\theta_R$  is the angle of the reference beam. A 2-D time integrating detector is placed at  $P_2$ . The signal,  $D(\xi, \eta, n)$ , detected during each light pulse is the time integrated intensity of the total light amplitude (the sum of Equations (13) and (14)).

$$\begin{aligned} D(\xi, \eta, n) &= \int_T |F_x(\xi, n) e^{j\frac{2\pi n\eta}{A}} + e^{j\frac{2\pi\sin\theta_R \xi}{\lambda}}|^2 dt \\ &= 2T |F_x(\xi, n)| \cos\left[\frac{2\pi\sin\theta_R \xi}{\lambda} - \frac{2\pi n\eta}{A} + \phi(\xi, n)\right] \\ &\quad + \text{Bias terms.} \end{aligned} \quad (15)$$

The signal accumulated on the detector after  $N$  pulses is given by:

$$\begin{aligned} \sum_{n=1}^N D(\xi, \eta, n) &= 2 \sum_{n=1}^N |F_x(\xi, n)| \cos\left[\frac{2\pi\sin\theta_R \xi}{\lambda} - \frac{2\pi n\eta}{A} + \phi(\xi, n)\right] \\ &\quad + \text{Bias terms} \\ &= 2T |g(\xi, \eta)| \cos\left[\frac{2\pi\sin\theta_R \xi}{\lambda} + \phi_g(\xi, \eta)\right] + \text{Bias terms} \end{aligned} \quad (16)$$

where  $g(\xi, \eta) = |g(\xi, \eta)| e^{j\phi_g(\xi, \eta)}$  is the 2-D Fourier transform of  $f(\alpha, \beta)$  as defined in Equation (9). Thus the 2-D transform forms on the detector on a spatial carrier of frequency  $\frac{\sin\theta_R}{\lambda}$  and it can be obtained by quadrature demodulation of the video signal when the detector is read-out.

## V. CONCLUDING REMARKS

We have demonstrated that AOD's which are 1-D spatial light modulators can be used to represent 2-D images in an optical processor by raster scanning the images and applying the video signal to the AOD. The use of a pulsed light source in the system isolates each raster line from the rest. A

## Appendix Vf

## Real Time Computation of Moments with Acousto-optics

Kelvin Wagner and Demetri Psaltis

Department of Electrical Engineering  
California Institute of Technology  
Pasadena, CA 91125Abstract

The separable nature of the geometric moment generating functions and the serial raster encoding of the image permits the 2-dimensional moment integral equation to be computed with a cascaded system of 1-dimensional integrations. In this paper new optical processing architectures are presented that use acousto-optic devices illuminated by pulsed sources to enter the data into the optical system. The advanced state of the art of the components used and the flexibility of these architectures can lead to the implementation of practical optical processing system for computing the moments of a real time high resolution image.

Introduction

Given a finite image intensity distribution  $f(x,y)$  over an aperture  $\Lambda$ , the  $p,q$ th geometric moment  $m_{pq}$  of order  $p+q$  is given by the moment integral equation

$$m_{pq} = \iint_{\Lambda} x^p y^q f(x,y) dx dy. \quad (1)$$

The value of these geometric moments are sensitive to the position, scale, rotation and contrast of the image. Appropriate nonlinear combinations of moments can be made invariant to all of these intraclass variations.<sup>1,2,3,5,6,8</sup> These moment invariants may have applications in pattern recognition as a low dimensionality feature space for image classification<sup>4</sup> and in coding the essential features of an image<sup>5</sup>. Alternatively the moments can be used to normalize an image<sup>7</sup> so that intraclass variations are minimized, so that standard pattern recognition techniques such as template matching can be applied successfully. The zeroth order moment gives the average of  $f(x,y)$ . The first order moments locate the image centroid  $\bar{x} = m_{10}/m_{00}$ ,  $\bar{y} = m_{01}/m_{00}$ . The central moments  $\mu_{pq}$  are defined with the centroid as the origin and are invariant to translations of the image

$$\begin{aligned} \mu_{pq} &= \iint_{\Lambda} (x-\bar{x})^p (y-\bar{y})^q f(x,y) dx dy \\ &= \sum_{r=0}^p \sum_{s=0}^q \binom{p}{r} \binom{q}{s} (-\bar{x})^{p-r} (-\bar{y})^{q-s} m_{rs}. \end{aligned} \quad (2)$$

Rotation and scale invariant moments of order  $(p,q)$  can be defined in terms of the ordinary moments  $m_{rs}$ .

Coherent optical processors have been proposed to compute the moments<sup>9-12</sup>, using 2-dimensional spatial light modulators (SLM) for real time operation. The separable nature of the geometric moment generating functions and serial raster encoding of the image allows the decomposition of the moment integral into cascaded 1-dimensional integrations. New architectures are presented that use 1-dimensional acousto-optic (AOD) spatial light modulators to enter the data into the optical system. In the first architecture the separable moment generating functions are entered through the AOD's, which allows flexibility in the choice of generating functions, and accuracy of their representation. Alternatively the moment generating functions can be written on film or used to modulate the optical source and the raster recorded image is entered into the optical system through the AOD. The large dynamic range and rapid programmability of acousto-optic devices can allow the implementation of practical real time optical computers for the generation of the geometric moments of an image.

Space Integrating Processor

Film based coherent optical processors have been proposed<sup>9-12</sup> for computing the geometric moments of an image using the 2-D spatial integration performed by a spherical Fourier transform (FT) lens. Teague's<sup>9</sup> method requires multiple differentiation of the FT of the image. The other methods<sup>10,12</sup> involve the spatial integration of the product of the

image  $f(x,y)$  and the moment generating function  $g_{pq}(x,y) = x^p y^q$ . Spatial frequency multiplexing of the generating functions in a computer generated hologram can be used to compute all the desired moments in parallel at separate locations in the frequency plane.

Since the geometric moment generating function  $x^p y^q$  is separable in cartesian coordinates, we can replace the moment mask of Ref. 10,11 with a pair of crossed acousto-optic deflectors (AOD) schlieren imaged onto the image film as shown in Fig. 1. This is similar to a triple product processor architecture<sup>17</sup>, except that the continuously modulated source is now pulsed. If the pulse width is less than the inverse bandwidth of the signals in the AODs, then it will act as a delta function in time and freeze the image of the moment generating function when it illuminates the input image. The functions  $t^p$  and  $t^q$  are synchronously applied to the AODs as amplitude modulations to an RF carrier at the center frequency of the AOD

$$\begin{aligned} S_{1p}(t) &= t^p e^{j^2 \pi f_0 t} \\ S_{2q}(t) &= t^q e^{j^2 \pi f_0 t} \end{aligned} \quad (3)$$

For odd powers there is a change of sign at  $t=0$  that is represented with a  $180^\circ$  phase change. This will lead to destructive interference at the integrated output which can be interferometrically detected. When these signals simultaneously slide to the centers of the AODs the laser diode (LD) is pulsed, collimated, and focused into a horizontal strip that enters AOD1 at the Bragg angle. The diffracted light is collimated in  $y$  and Fourier transformed in  $x$  to produce a vertical strip that illuminates AOD2 at its Bragg angle. Both undiffracted components are filtered, and the doubly diffracted light is expanded in  $x$  to a square so that AOD1 is imaged onto  $f(x,y)$  in the  $-x$  direction and AOD2 is imaged onto  $f(x,y)$  in the  $-y$  direction. The light amplitude incident on the image is similar to an outer product and is modulated by

$$\begin{aligned} E_1(x,y,t) &= \delta(t) S_{1p}(x+vt) S_{2q}(y+vt) \\ &= \delta(t) S_{1p}(x) S_{2q}(y). \end{aligned} \quad (4)$$

This is multiplied by the image transmittivity,  $f(x,y)$ , and the product is Fourier transformed by the integrating lens. This transform can be sampled at its center or integrated over its whole extent to yield an interferometrically detected signal proportional to the desired moment.

$$m_{pq} = \iint_A S_{1p}(x) S_{2q}(y) f(x,y) dx dy = \iint_A x^p y^q f(x,y) dx dy. \quad (5)$$

All the desired moments could be computed successively with high accuracy and dynamic range on a single detector pair very rapidly. For an AOD with a  $10 \mu\text{sec}$  aperture time moments through the tenth order could be computed in  $.5 \text{ msec}$ . This would allow many differently windowed sets of moments to be computed during each frame time of available 2-D spatial light modulators. Alternatively the moments could be computed simultaneously with lower dynamic range in a few microseconds by using temporal frequency multiplexing of the moment generating functions. This is shown in Figure 2. In this case the following signals are applied to the two AOD's of the system.

$$\begin{aligned} S_1(t) &= \sum_{p=0}^P t^p e^{j2\pi(f_0 + p\Delta f)t} \\ S_2(t) &= \sum_{q=0}^Q t^q e^{j2\pi(f_0 + q\Delta f)t} \end{aligned} \quad (6)$$

where  $\Delta f$  is the frequency separation of the frequency multiplexed moment generating functions. For an image bandwidth  $B$  [cy/mm] and acoustic velocity  $v$ , the different moments would be spatially separated in the output plane if  $\Delta f/v > B$ , and therefore could be sampled by an appropriately arranged array of detectors.

The versatility of this system allows the direct optical computation of the central moments  $\mu_{pq}$  instead of the geometric moments  $m_{pq}$ . First the centroid is located in each dimension separately by finding the 0th and 1st order moments and using  $\bar{x} = m_{10}/m_{00}$ ,



$\bar{y} = m_{01}/m_{00}$ , or by operating the source CW, and locating the zero crossing of the detector's temporal output as the generating functions for  $m_{10}$  or  $m_{01}$  slide through the Bragg cells.

To compute the central moments directly the moment generating functions are input to AOD1 and AOD2 with a relative delay  $\tau_d = \tau_1 - \tau_2 = x/v - y/v$  and the LD is pulsed at  $t = \tau_1$ . This aligns the origin of the moment generating functions with the image centroid, and the spatially integrated outputs compute the central moments  $\mu_{pq}$ . This architecture also allows the windowing of the region for which the moments are being computed by simply windowing the electronic signals  $S_1(t)$  and  $S_2(t)$ , this would allow a rapid search for the appropriate window within  $f(x,y)$  to be made under computer control.

### Space and Time Integrating Architecture

The performance of the space integrating moment processor could be limited by the 2-D spatial light modulator (SLM) required for real time operation. In many applications the image is available to the optical processor in the form of a serial raster signal. In this case, the 2-D image  $f(x,y)$  can be entered into the optical processor one line at a time through a 1-D SLM such as an acousto-optic device (AOD) <sup>13,14</sup>. The raster scanned representation of a continuous image  $f(x,y)$  is denoted by  $f(x,n\Delta y)$  where  $n$  is an integer and  $\Delta y$  is the separation between the raster lines. The moments can be calculated from the sampled image by replacing the integration over  $y$  in Eq. (1) with a summation over  $n$

$$\mu_{pq} = \sum_{n=1}^N (n\Delta y)^q \int x^p f(x, n\Delta y) dx. \quad (7)$$

This formation suggest a hybrid space and time integrating system <sup>16,15,13</sup> as shown in Fig. 3. The video raster lines are sequentially applied to an AOD operated in the intensity modulation regime and oriented in the  $x$  direction, as an amplitude modulation of an RF carrier at the center frequency of the piezoelectric transducer. The AOD is illuminated by the collimated light emitted from a closely spaced array of  $Q+1$  pulsed modulated laser diodes (LD). If all the LD's emit light at the same wavelength then the spatial frequency multiplexed light incident on the AOD must be within its Bragg angular aperture. Alternatively, the momentum mismatch can be compensated by varying the wavelength in the LD array, so that the light from each LD is incident on the AOD at the Bragg angle for that wavelength. When the  $n$ th video raster line completely fills the AOD aperture, the entire LD array is synchronously pulsed with a pulse width short enough to freeze the image of the raster line within the AOD. The intensity modulation of the  $q$ th LD is given by

$$I_q(t) = \sum_{n=1}^N (n^q + \text{bias}) \delta(t - nT), \quad (8)$$

where  $T$  is the video line time and the bias may be needed to represent the bipolar odd moment generating functions. The bias is not necessary for the even moments and spatial multiplexing can be used rather than bias to represent the bipolar odd moments. The light diffracted by the AOD is expanded and collimated in  $y$  and schlieren imaged in  $x$ , so the intensity incident on  $P_3$  from the  $q$ th LD during the  $n$ th raster line is

$$O_3(x,t) = I_q(t) f(t - \frac{x}{v}, n\Delta y) = n^q \delta(t - nT) f(\frac{x}{v}, n\Delta y). \quad (9)$$

At plane  $P_3$  a mask is placed containing the intensity transmittance variations  $x^P$  at different  $y$  coordinates:

$$t(x,y) = \sum_{p=0}^P x^p \text{rect} \left[ \frac{y - y_0}{y_0} \right]. \quad (10)$$

The light leaving  $P_3$  (modulated by the product of the incident intensity and the mask transmittance), is then imaged in the  $y$  dimension and integrated in the  $x$  direction onto the plane  $P_4$ . At the output plane there are  $(Q+1)$  columns of  $(P+1)$  detectors each. Each LD, is imaged onto a separate column and to avoid crosstalk the columns must be separated by  $\Delta > \lambda Fv/B$ , where  $F$  is the focal length of the integrating lens,  $v$  is the acoustic velocity and  $B$  is the video bandwidth. If the detector is wide enough to collect all the light from its associated laser diode then the detected signal on the  $p,q$ th detector during the  $n$ th pulse will be proportional to

$$s_{pq}(n) = \int_{(n-\frac{1}{2})T}^{(n+\frac{1}{2})T} I_q(t) \int O_3(x,t) x^p dx dt = n^q \int f(\frac{x}{V}, n\Delta y) x^p dx. \quad (11)$$

If the detector is time integrated for a full video frame the output of the p,qth detector becomes

$$\begin{aligned} s_{pq} &= \int_0^{NT} I_q(t) \int O_3(x,t) x^p dx dt \\ &= \sum_{n=0}^N n^q \int f(\frac{x}{V}, n\Delta y) x^p dx \\ &= \sum_{n=0}^N \int n^q x^p f(\frac{x}{V}, n\Delta y) dx, \end{aligned} \quad (12)$$

which is proportional to the desired moment calculation. All  $(P+1) \times (Q+1)$  moments are computed in parallel on a 2-dimensional array of detectors.

An alternative topology of the optical processor is obtained by spatially multiplexing the LDs in the y direction as shown in Fig. 4. This eliminates the problem of Bragg angle mismatch previously encountered, and allows all the moments to be detected on a single linear detector array, without crosstalk. The mask must be repeated once for each laser diode for this architecture and its intensity transmittance is given by

$$t(x,y) = \sum_{q=0}^Q \sum_{p=0}^P x^p \text{rect} \left[ \frac{y - q(p+1)y_0 - py_0}{y_0} \right] \quad (13)$$

Another useful feature of this architecture is its extension to bipolar processing as shown in Fig. 5. For odd q two laser diodes can be spatially multiplexed in the x direction, one represents the positive and the other the negative portions of the moment generating function. Similarly for odd p two rows of the mask are used to represent the positive and negative portions of this half of the moment generating function. Two linear time integrating detector arrays are used to detect the four cross products. The outputs are electronically added and subtracted to yield the calculated bipolar moment.

### Discussion

In optical analog computers of this type errors and noise can enter into the calculation for many reasons. These include noise in the modulated laser diode sources, nonlinearities in the acousto-optic Bragg cell, quantization errors and film nonlinearities of the computer generated masks, optical aberrations, coherent noise and detector noise. Careful optical and electronic design can minimize most of these effects, and in practice the output detector array is a major factor that limits the accuracy of an optical computer. Typical charge coupled device (CCD) detector arrays have an output SNR of 1000:1, which allows a digitization of the optically computed geometric moments to a resolution of 10 bits. A digital post processor can then combine the geometrical moments to produce the invariants and perform a pattern classification based on the invariant feature space. The geometrical moment optical preprocessor takes the bulk of the computational load away from the digital computer, however some accuracy is sacrificed.

The separable moment generating function  $x^p$  is positive definite for even powers p, and an incoherent unipolar intensity representation can be used. For odd powers p, the moment generating functions become bipolar. Therefore the capability to represent bipolar quantities must be incorporated in the optical processor. If coherent light is used the cancellation needed for odd moment powers can be performed in the space integrating processors by destructive interference and interferometric detection. However in the time integrating architectures the processing is performed by integrating photogenerated charge on the detector, which is proportional to the number of incident photons or the intensity and therefore strictly positive. Bipolar operations can be performed by placing the odd moment generating functions on a bias. This in turn places a bias on the detector thereby decreasing the available dynamic range of the computed moments. Alternatively the positive

and negative halves of the separable odd moment generating functions can be represented in separate channels of the processor. The crossproduct terms must be electronically combined with the appropriate sign when the detector is read out in order to produce an estimate of the bipolar moment. The achievable accuracy and dynamic range of this bipolar estimate will be limited by the requirement that none of the detectors saturate, and that the variances of the noise will add. The possibility of a special purpose directly coupled detector structures to perform the continuous subtraction needed for incoherent bipolar optical processing merits further research.

### Conclusions

In conclusion we have proposed several optical computing architectures for calculating the geometrical moments of images in real time. The space integrating processor requires a 2-D SLM to represent the image, but has the flexibility of electronic control of the separable moment generating function. With this processor the moments can be calculated sequentially at a rapid rate with high accuracy. The time and space integrating architectures are not as flexible since the moment generating functions are fixed by the computer generated masks. However since acousto-optic devices are used to enter the raster video data into the optical processing system, the need for a real time 2-D SLM is avoided.

### Acknowledgments

We would like to thank Dr. Yaser Abu-Mostafa for many illumination discussions on moment invariants.

The research reported in this paper is supported by the Air Force Office of Scientific Research and the Army Research Office.

### References

1. M. K. Hu, IRE Trans. Inf. Th. IT-8, 179 (1962).
2. S. Maitra, Proc IEEE 67, 697 (1979).
3. S. S. Reddi, IEEE Trans. Pattern Anal. Machine Intell. PAMI-3, 240 (1981).
4. S. Dudani et.al., IEEE Trans. Computers C-26, 39 (1977).
5. R. C. Gonzales and P. Wintz, Digital Image Processing, Addison-Wesley, Reading, Mass., (1977).
6. Y. Abu-Mostafa and D. Psaltis, IEEE Trans. on PAMI, to be published.
7. Y. Abu-Mostafa and D. Psaltis, IEEE Trans. on PAMI, to be published.
8. M. R. Teague, JOSA 70, 920 (1980).
9. M. R. Teague, Applied Optics 19, 1353 (1980).
10. J. A. Blodgett et.al., Optics Letters 7, 7 (1982).
11. D. Casasent and D. Psaltis, SPIE 201, 107 (1978).
12. D. Casasent and D. Psaltis, Optics Letters, 5, 395 (1980).
13. D. Psaltis, JOSA, 71, 198 (1981).
14. D. Psaltis, Applied Optics, 21, 491 (1982).
15. D. Psaltis and D. Casasent, Applied Optics, 18, 3203 (1979).
16. T. R. Bader, Applied Optics, 18, 1668 (1979).
17. P. Kellman, Ph.D. thesis, Stanford U. Press, Stanford, California (1979).

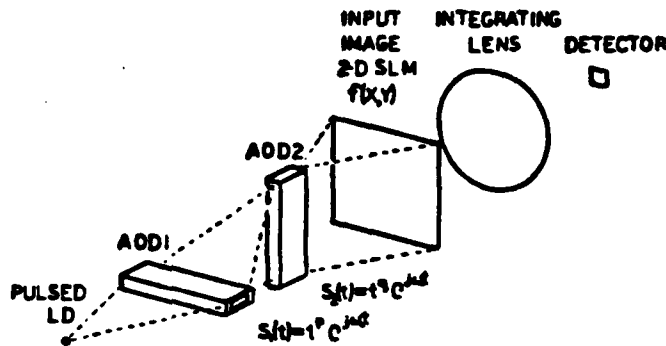


Figure 1. Space integrating geometric moment processor with crossed Bragg cells to enter the separable moment generating function.

Space Integrating Moments Architecture with Crossed Bragg Cells

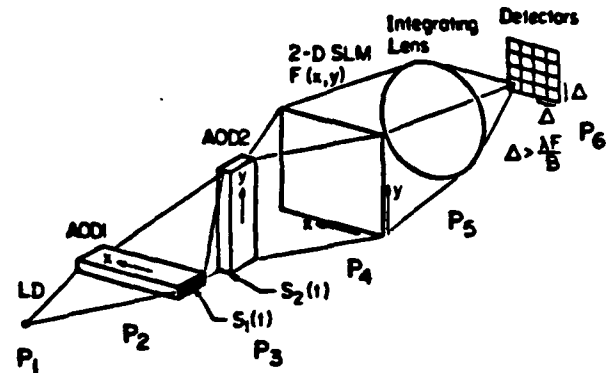


Figure 2. Frequency multiplexed space integrating architecture.

Space and Time Integrating Moments Architecture

Multichannel Space Integrating Processor for each Pulse

$$C_{ij}(n\Delta t) = n! \int F(x,n) x^i dx$$

Time Integrating Detector Sums for N Pulses

$$M_{ij} = \sum_n n! \int F(x,n) x^i dx$$

$$= \sum_n \int F(x,n) x^i n! dx$$

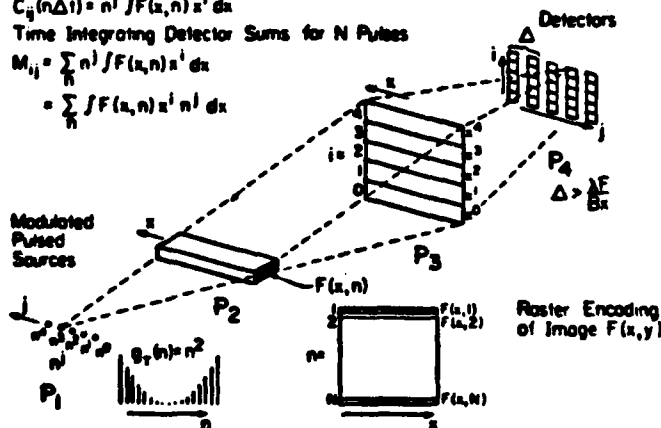
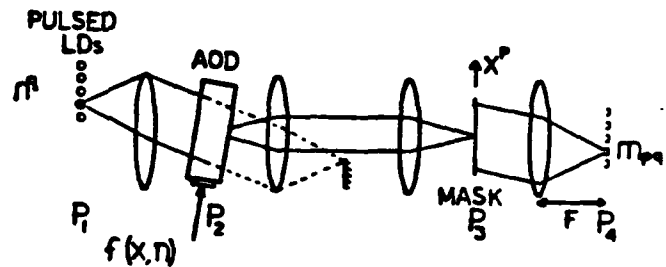


Figure 3a. Time and space integrating moment processor with horizontal spatial multiplexing of modulated pulsed laser diodes and acousto-optic entry of video raster data.



$$P_2 \quad n^p f(x,n)$$

$$P_3 \quad f(x,n) x^p n^q$$

$$P_4 \quad \int f(x,n) x^p n^q dx$$

$$\sum_{n=1}^N \int f(x,n) x^p n^q dx$$

Figure 3b. Top view and operation of the processor.

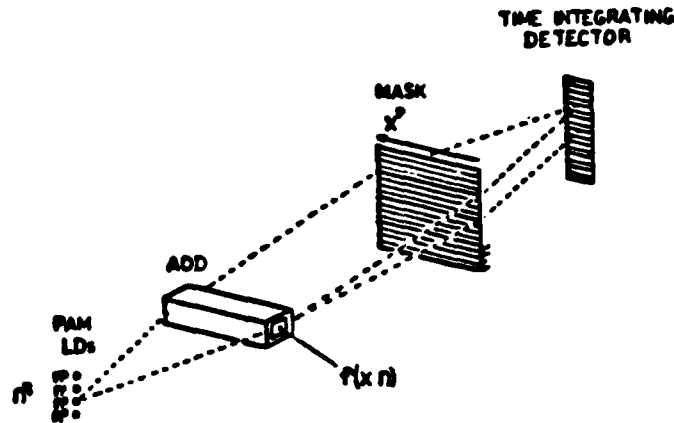


Figure 4. Time and space integrating moment processor with vertical spatial multiplexing of the laser diode array.

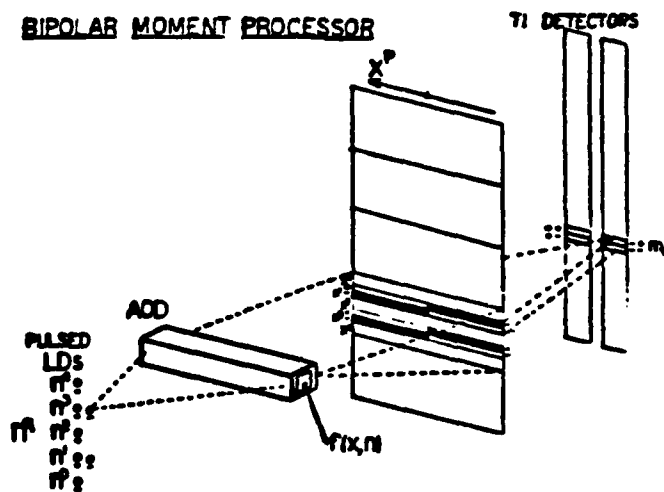


Figure 5. Bipolar representation of the odd moment generating function in the processor of Figure 4, by horizontal multiplexing of the sources and vertical multiplexing in the mask.

## VI. REFERENCES

- [1] A. Vander Lugt, IEEE Trans. Info. Theo., IT-10:2, 1964
- [2] D. Casasent, Proc. IEEE, Vol. 65, #1, Jan 1977.
- [3] A Tanguay, Jr., "Spatial Light Modulators for Real Time Optical Processing", in Proceedings of the workshop on Future Directions for Optical Information Processing, Lubbock, Texas.
- [4] Special Issue on Acousto-optic Signal Processing, Proc. IEEE,
- [5] T. Bader, Applied Optics, Vol. 18, 1979, p. 1668.
- [6] D. Psaltis and D. Casasent, Applied Optics, Vol. 18, 1979, p. 3203.
- [7] D. Psaltis, J. Opt. Soc. Am., Vol. 71, Feb. 1981, p.198.
- [8] D. Psaltis, Applied Optics, Vol. 21, Feb. 1982, p. 491.
- [9] D. Psaltis, E. Paek and S. Venkatesh, Proc. of Int. Opt. Comp. Conf., Cambridge, MA, 1983.
- [10] K. Wagner and D. Psaltis, Proc. SPIE, Vol. 352-19, San Diego, 1982.
- [11] D. Psaltis and K. Wagner, Opt. Engineering, Sept/Oct 1982, Vol. 21, p. 822.
- [12] D. Psaltis, K. Wagner and M. Haney, Proc. SPIE, Vol. 352-16, San Diego, 1982.
- [13] D. Psaltis, Proc. Elect.-Opt. Sys. Des. Conf., Anaheim, 1981.
- [14]
- [15] M. Monahan et. al., Digest of International Optical Computing Conference, Washington, DC, 1975.
- [16] P. Kellman, private communication.
- [17] D. F. Barbe, Proc. IEEE, Vol. 63, #1, 1975, p. 38.
- [18] J.A. Hall, "Arrays and Charge Coupled Devices", Chapter 8, in "Applied Optics and Optical Engineering", Vol. VIII, R. R. Shannon and J. C. Wyant Eds., Academic Press, New York, 1980.

**END**

**FILMED**

**1-84**

**DTIC**